Directing the Mineralization of Inorganic Nanomaterials using Programmable Macromolecular Building Blocks

by

Nada Youssef Mahmoud Naser

A dissertation
Submitted in partial fulfillment of the
Requirements for the degree of

Doctor of Philosophy

University of Washington
2024

Reading Committee:
François Baneyx, Chair
Lilo Pozzo
Elizabeth Nance

Program Authorized to Offer Degree:
Department of Chemical Engineering

University of Washington

Abstract

Directing the Mineralization of Inorganic Nanomaterials using
Programmable Macromolecular Building Blocks

Nada Youssef Mahmoud Naser

Chair of the Supervisory Committee:
François Baneyx
Department of Chemical Engineering

Sequence-defined building blocks such as peptides, proteins, and peptoids offer a path toward the construction of precision materials by enabling the organization, mineralization and dynamic reconfiguration of organic and inorganic components through engineered functions. With thermoresponsive elastin-like polypeptides (ELPs) fused to solid-binding peptides, we demonstrate the biomimetic mineralization of highly uniform and positively charged silica nanoparticles that support the one-step assembly of mono- and bi-material superstructures with highly integrated components. Using gold-binding ELPs, we synthesize gold nanoparticles that can be reversibly assembled into clusters with distinct plasmonic signatures in response to temperature change. For both systems, we study how protein sequence and concentration, solution conditions, and temperature affect mineralization outcomes and plasmonic responses. In collaborative work, we transfer learnings from solid-binding peptides to peptoids by designing a polymeric analog of the

R5 silicifying peptide. The biomimetic approaches to the synthesis of size- and composition-controlled nanomaterials described herein are simple and environmentally friendly, and the extracted design rules should prove useful for the biological fabrication of a broad range of hierarchical systems with applications in biomedicine and energy-related fields.

In loving memory

of

my father

Table of Contents

ABSTRACT ..... **I**

ACKNOWLEDGMENTS ..... **X**

CHAPTER 1 INTRODUCTION **1**

1.1 BIOMIMETIC MINERALIZATION OF INORGANIC MATERIALS 2
1.1.1 Solid binding peptides and proteins *3*
1.1.2 Biomimetic silica mineralization *4*
1.1.3 Biomimetic titania mineralization *5*
1.1.4 Biomimetic gold mineralization *6*
1.2 STIMULI RESPONSIVE AND FUNCTIONAL NANOMATERIALS 7
1.3 FIGURES 9

CHAPTER 2 BIOMIMETIC MINERALIZATION OF POSITIVELY CHARGED SILICA NANOPARTICLES TEMPLATED BY SOLID-BINDING ELASTIN-LIKE POLYPEPTIDES **11**

2.1 INTRODUCTION 11
2.2 MATERIALS AND METHODS 12
2.2.1 DNA manipulations and protein purification *12*
2.2.2 Characterization and quantification of solid-binding ELP constructs *14*
2.2.3 Silica mineralization *15*
2.2.4 Analytical techniques *15*
2.3 RESULTS 17
2.3.1 V54-Car9 forms micelles above its transition temperature *17*
2.3.2 Silica mineralization templated by V54-Car9 micelles and the influence of biological buffer on silicification products *18*
2.3.3 Studying reaction kinetics and surface charge *21*
2.3.4 Applications to electrostatic assembly of hierarchical and composite superstructures *23*
2.4 DISCUSSION 25
2.5 CONCLUSIONS 29
2.6 FIGURES 31

CHAPTER 3 GENETIC ENGINEERING OF SILICA-BINDING ELPS TO STUDY TEMPERATURE-INDUCED MICELLIZATION AND MINERALIZATION KINETICS **45**

3.1 INTRODUCTION 45
3.2 MATERIALS AND METHODS 46
3.3 RESULTS AND DISCUSSION 47
3.3.1 Influence of mutations on protein assembly *47*
3.3.2 Arginine-4 is critical for V54-Car9 micelle formation *47*
3.3.3 Silicification captures subtle details of the protein templates *49*
3.4 CONCLUSION 52
3.5 FIGURES 54

CHAPTER 4 TEMPLATED MINERALIZATION AND ACTUATION OF GOLD NANOPARTICLES USING SOLID-BINDING ELASTIN-LIKE POLYPEPTIDES **59**

4.1 INTRODUCTION 59

4.2 Materials and Methods 59
4.2.1 Au mineralization 60
4.2.2 AuNP characterization and actuation 60
4.3 Results and Discussion 60
4.3.1 Characterization of solid-binding ELP constructs 60
4.3.2 Gold mineralization and temperature-triggered actuation using V54-A3 61
4.3.3 Modular design of Au-binding ELPs and high throughput AuNP synthesis 62
4.3.4 Next steps 63
4.4 Conclusions 64
4.5 Figures 65

CHAPTER 5 BIO-INSPIRED SILICA MINERALIZATION USING R5 PEPTOIDS 74

5.1 Introduction 74
5.2 Materials and Methods 75
5.2.1 Synthesis of R5 peptide and peptoid analogs 75
5.2.2 Silica mineralization templated by R5 peptides and peptoid analogs 76
5.2.3 Surface Plasmon Resonance (SPR) 77
5.3 Results and Discussion 77
5.4 Conclusion 79
5.5 Figures 80

CHAPTER 6 CONCLUSIONS 84

APPENDIX A INORGANIC MINERALIZATION TEMPLATED BY SELF-ASSEMBLING *DE NOVO* DESIGNED PROTEIN FIBERS 87

A.1 Introduction 87
A.2 Materials and Methods 88
A.3 Results and Discussion 89
A.3.1 Self-assembly newly constructed Car9-tagged DHF monomers 89
A.3.2 Titania mineralization on de novo self-assembling fibers 89
A.4 Conclusion 90
A.5 Figures 92

FUNDING INFORMATION 99

REFERENCES 100

List of Figures

Figure 1.1 Micrographs of diatom silica nanostructures. Scale bars are 1 μm (a and k), 5 μm (b), 10 μm (c, f, and l), 500 nm (d), 2 μm (e, g, h, and j), and 50 μm (i). Adapted from Ref [45] 9

Figure 1.2 Micrographs of silicas particles mineralized in solutions of R5 peptide variants shown. Scale bar is 1 μm. Adapted from Ref [21] 10

Figure 2.1 (A) Amino acid sequences of the V54 control protein and V54-Car9 silica-binding ELP. Positively and negatively charged residues are colored in blue and red, respectively . (B) Coomassie Blue-stained SDS-PAGE used to analyze V54-Car9 (lane 2) and V54 (lane 3) after two cycles of ITC purification. Proteins were diluted to 100 μM and boiled in SDS before loading. The staining of V54 by Coomassie Blue is inefficient due to the lack of charged residues. 31

Figure 2.2 Temperature-dependent evolution of the turbidity (A) and D_h (B) of a 75 μM solution of V54 (black) or V54-Car9 (orange). Numbers in panel B correspond to the D_h of the different species. 32

Figure 2.3 Kinetics of V54-Car9 micellization. (**A**) A 50 μM solution of V54-Car9 initially at room temperature was transferred to 65°C. DLS intensity profiles collected at the indicated time points show the transition of unimers to intermediate aggregates that progressively collapse into micelles. (**B**) Quantification of the evolution of intermediate aggregates (300 nm peak) and micelles (30 nm peak) over time. 33

Figure 2.4 SEM images of silica particles mineralized in solutions of V54-Car9 (A) or V54 (B) in 20 mM Tris-HCl, pH 7.5 at 45°C. 34

Figure 2.5 (A) Field of view and (B) magnified SEM images of mineralization products obtained at 45°C in DI water (*hot synthesis*), representative TEM image (C), and the corresponding particle size distribution (D). 35

Figure 2.6 (A) Field of view SEM image of mineralization products obtained at 22°C in DI water (*cold synthesis*) and the corresponding particle size distribution (B). 36

Figure 2.7 Kinetics of silica particle growth in the absence of Tris buffer at 22°C (blue triangles) and 45°C (red circles). Bars correspond to the full width at half maximum (FWHM) of the intensity size distributions measured by DLS. Experiments were conducted with 75 μM of V54-Car9 and 100 mM of silicic acid. 37

Figure 2.8 Mineralization controls lack size and morphology control. Representative field of view SEM image of silica mineralized in a solution of 75 μM V54 in DI water held at 45°C (A). SEM images of precipitation products obtained by incubating 100 mM of silicic acid at 45°C for 8h in 20 mM Tris-HCl, pH 7.5 (B) or DI water (C). 38

Figure 2.9 SAXS, AFM, and HRTEM characterization of silicification products. (A) SAXS profiles of silicification products obtained at 22°C (blue) or 45°C (red) fit to a raspberry sphere model (solid lines), (B) Distribution of core particle diameter from SAXS fit. (C) Schematic representation of the raspberry structure used for fitting of SAXS profiles. The core particles with radius R_c are decorated with embedded spheres of radius R_p, each with a projecting hemisphere. Tapping-mode AFM topography images (D, G), phase images (E, H), and HRTEM images (F, I) of NPs mineralized at 45 or 22°C, respectively. 39

Figure 2.10 (A) TGA thermograms of *hot* (red) and *cold* (blue) *synthesis* products compared to commercial silica before (black) and after (orange) decoration with a molar excess of V54-Car9. All TGA samples were extensively dialyzed to remove loosely bound or unreacted ligands. (B) DLS intensity profiles of silicification products at 22°C (solid lines) or 45°C (dashed lines) after incubation at the indicated temperatures for 10 min each. SEM images of mineralized nanoparticles at 45°C (C) or 22°C (D) after the addition of 75 μM V54-Car9 and incubation for 10 min. 40

Figure 2.11 XPS analysis of mineralization products obtained by incubating 75 μM of V54-Car9 with 100 mM of silicic acid in water at 45°C for 8h. Two different spots were sampled to yield a mean elemental composition of 41.3% oxygen, 15.6% silicon, 38.2% carbon, and 5.1% nitrogen. 41

Figure 2.12 (A) Schematic of the electrostatically driven co-assembly of positively charged mineralized silica NPs (blue) with an excess of 10-nm negatively charged silica NPs (gray). (B) Products of assembly step (***1***). (C) Products of assembly step (***2***). 42

Figure 2.13 (A) Schematic of electrostatically driven co-assembly of positively charged mineralized silica NPs (blue) and 20-nm negatively charged NPs (gray). SEM images and magnified insets of the co-assembly of mineralized NPs with 20-nm silica NP (B) or 20-nm AuNPs (C). (D) HRTEM of the silica-Au interface with field of view inset. 43

Figure 2.14 SEM images of mineralized silica/Au co-assemblies after 6 months of storage. Scale bars are 200 nm. 44

Figure 3.1 Low energy structure of Car9 in solution (A) and at the silica interface (B). The solution structure was proposed by Rosetta. (B) Superimposition of the structure proposed by Rosetta (green) and MD simulations (pink). Adapted from Ref. [31] 54

Figure 3.2 (A) Amino acid sequences of the Car9 variants. Positively and negatively charged residues are colored in solid blue and red, respectively. Substitutions are highlighted with red circles. Temperature-dependent evolution of the D_h (left axis, black traces) and turbidity (right axis, purple traces) of 75 μM solutions of V54-Car9 (B), V54-P9AG10A (C), V54-K8AK11A (D), V54-R4QR12Q (E), V54-Q4 (F), and V54 (G). 55

Figure 3.3 Representative SEM micrographs of mineralization products obtained with 75 μM solutions of V54-Car9 (A and D), V54-P9AG10A (B and E), or V54-K8AK11A (C and F). Reactions were conducted at 50°C (A-C) or 65°C (D-F) for two hours. Scale bars are 200 nm. (G) Mean diameters and standard deviations of silica nanoparticles mineralized at the indicated temperatures (N = 100). 56

Figure 3.4 SEM micrographs of the mineralization products with 75 μM solutions of V54-R4QR12Q (A and C) or V54-Q4 (B and D) at 50°C (A and B) and 65°C (C and D). Scale bars are 500 nm. 57

Figure 3.5 Temperature-dependent evolution of the D_h (left axis, black traces) and turbidity (right axis, purple traces) of 75 μM protein solutions of V54-R4Q (A) and V54-R12Q (D). SEM micrographs of silica mineralization products at 50°C (B, E) or 65°C (C, F) of V54-R4Q and V54-R12Q, respectively. 58

Figure 4.1 (A) Amino acid sequences of the V54 control ELP and Au-binding ELPs: V54-AuBP1, V54-AuBP2, and V54-A3. Positively and negatively charged residues are colored in blue and red, respectively. Temperature-dependent evolution of the turbidity (A) and D_h (B) of 75 μM solutions of proteins. 65

Figure 4.2 SEM (A, B) and TEM (C) images, corresponding particle size distribution (D), and DLS intensity profile (E) of AuNPs mineralized with 100 μM of V54-A3 at 25°C. ... 66

Figure 4.3 Field of view (A) and magnified (B-D) SEM images of AuNP clusters formed after incubation at 45°C for 5 min and the corresponding cluster size distribution (E). . 67

Figure 4.4 UV-Visible spectra (A), observed turbidity (B), and LSPR shift (C) associated with repeated cycles of heating AuNPs to 45°C and cooling to 25°C with 10 minutes equilibration steps at each temperature. 68

Figure 4.5 Field of view (A-B) and magnified (C-D) TEM images of AuNPs synthesized in solutions of V54-AuBP1 (A and C) or V54-AuBP2 (B and D). 69

Figure 4.6 LSPR peaks of AuNPs synthesized in solutions of V54-AuBP1 (A), V54-AuBP2 (B), or V54-A3 (C) at varying concentrations as indicated. 70

Figure 4.7 UV-visible spectra of the AuNPs synthesized in 6.25 (A), 12.5 (B), 25 (C), 50 (D), 75 (E), or 100 μM (F) solutions of V54-AuBP1 in HEPES buffer supplemented with $HAuCl_4$. Samples were thermocycled by incubating the 96-well plate at 45°C (hot) or 25°C (cold) for 10 min. 71

Figure 4.8 UV-visible spectra of the AuNPs synthesized in 6.25 (A), 12.5 (B), 25 (C), 50 (D), 75 (E), or 100 μM (F) V54-AuBP2 solutions of in HEPES buffer supplemented with $HAuCl_4$. Samples were thermocycled by incubating the 96-well plate at 45°C (hot) or 25°C (cold) for 10 min. 72

Figure 4.9 UV-visible spectra of the AuNPs synthesized in 6.25 (A), 12.5 (B), 25 (C), 50 (D), 75 (E), or 100 μM (F) solutions of V54-A3 in HEPES buffer supplemented with $HAuCl_4$. Samples were thermocycled by incubating the 96-well plate at 45°C (hot) or 25°C (cold) for 10 min. 73

List of Tables

Table 2.1 summarizing the silicification reaction conditions and characterization of mineralized silica NPs in DI water. ……..22

Table 3.1 summarizing T_t, zeta potential, and micellization behavior of solutions of ELP-Car9 mutants ……..….48

Table 3.2 summarizing the size distribution of silica nanoparticles mineralized in solutions of V54-Car9 variants at the indicated temperatures (*N* = *100*). ……....50

Acknowledgments

I would like to express my sincere gratitude to my Ph.D. advisor, François Baneyx, for his guidance, mentorship, and continuing support to pursue exciting opportunities and collaborations throughout my graduate school. I am grateful to my committee members: Lilo Pozzo, Elizabeth Nance, and Brandi Cossairt for their insightful discussions and suggestions.

I would like to thank my collaborators at the Center for the Science of Synthesis Across Scales (CSSAS): Huat Thart Chiang, Kacper Lachowski, Helen Larson, Hao Shen, Biao Jin, Shuai Zhang, Kaylyn Torkelson, and my lab mates: Jinrong Ma, Yifeng Cai, Zhixing Lin, Will Wixson, Karthik Pushpavanam, and Mason Nelson.

Finally, I would like to thank my partner, Will, and my friends, Amira, Ty, Jacob, Nisarg, Yasmeena, and Aliyah, for their love and community, for grounding me, and for supporting me through my graduate school journey over the past five years.

Chapter 1 Introduction

In natural biomineralization systems, living organisms produce sophisticated hierarchical organic-inorganic hybrid materials including bones, teeth, shells, sponges, and others that combine various building blocks in a controlled and well-ordered manner. Using high information content macromolecular building blocks, such as nucleic acids, peptides, and proteins, they achieve fascinating degrees of complexity from nanoscale patterning to macroscale optical and mechanical properties that aid in their various functionalities. We seek to design and study biomimetic mineralization mediated by biological building blocks to gain control over the range of compositions, morphologies, and crystallographies similar to those observed in natural biomineralization while retaining the ability to mineralize inorganic materials under mild aqueous conditions. We study how solution conditions, sequence modifications, and molecular reconfiguration influence mineralization outcomes.

This dissertation focuses on the synthesis and organization of inorganic nanomaterials mediated by various classes of high information content biomolecules. First, we design a silica-binding intrinsically disordered, thermoresponsive **polypeptide** to promote silica nanoparticle synthesis and access a large range of mineralization outcomes based on reaction temperature, presence of biological buffer, and the silica-binding peptide sequence (Chapters 2 and 3). In a similar design, we use gold-binding thermoresponsive **polypeptides** to template gold nanoparticle (AuNP) synthesis and mediate their reversible actuation in response to temperature stimuli (Chapter 4). In Chapter 5, we propose a **peptoid** as an alternative sequence-defined synthetic polymer that mimics bio-inspired **silicifying peptides** and can offer significant increases in the molecular design

space. This study is assisted by molecular dynamics (MD) predictions to gain predictive insights on their structural differences and their biomimetic silica mineralization outcomes.

1.1 Biomimetic mineralization of inorganic materials

For decades, scientists have been inspired by nature's ability to create hierarchical materials with multi-scale order, sophisticated morphologies, unique physical properties, and various functionalities under mild aqueous conditions.[1,2] Those natural hierarchical systems rely on high information content macromolecules such as nucleic acids, foldamers, peptides, proteins, and so on to establish precise order and self-assembly across scales, template the bottom-up synthesis of controlled hybrid nanostructures, and the fabricate hybrid systems that integrate biological components with silicon-based electronic devices. Studies were inspired by the natural self-assembly process to create complex and diverse hierarchical structures using just one or a combination of simple building blocks such as RNA,[3,4] DNA,[5–7] and short peptide sequences. [8–10] Others were inspired by the self-assembly of larger, more structurally complex building blocks, such as the S-layers enclosing archaea and bacteria, to design protein-based structures with sophisticated functionalities.[11–13] Many studies focused on biological systems and their ability to read environmental stimuli and send precise signals and their inter- and intra-cellular communication networks facilitated by membrane proteins, which enabled the integration of biological components into electronic devices and gave rise to the field of bionanoelectronics.[14–17] Studies conducted by Kröger and others drew inspiration from the nanostructured silica in the cell walls of the diatom *Cylindrotheca fusiformis* to examine the mechanism behind biosilicification and isolate a group of cationic peptides responsible for biosilicification, called silaffins for silica-affinity, that were extensively

studied to drive the biomimetic silicification reaction at ambient temperature, pressure, pH conditions.[18–21] The monodispersity and programmability of high information content macromolecules have proven valuable to expanding the range of compositions, morphologies, and crystal structures observed in natural biomineralization processes while retaining the ability to mineralize inorganic materials under mild aqueous conditions.

1.1.1 Solid binding peptides and proteins

Solid binding peptides (SBPs) are short amino acid motifs isolated for their binding affinity to specific inorganic materials through noncovalent interactions. SBPs are typically selected from combinatorial phage or cell surface display libraries where a large number of candidates are contacted with the target inorganic surface and repeatedly washed until the strongest binders are identified and sequenced.[22,23] Their adhesive properties have been widely exploited, individually or fused to larger protein scaffolds, for binding, decorating, organizing, assembling a variety of materials to create complex hierarchical systems.[24–27] The Baneyx Lab originally identified the Car9 dodecapeptide (DSARGFKKPGKR) for its binding affinity to carbon substrates[26] and later discovered its selective binding to silica surfaces.[28,29] It was then developed as a cleavable modular affinity tag used for protein purification on silica gel columns. Beyond its commercial advantages as a purification tag, Car9 has been used as a fusion to superfolder green fluorescent protein (sfGFP) to study the adhesion regimes[30,31] and create ordered intricate hierarchical systems integrating polymer, protein, and inorganic building blocks.[32,33] In addition to their adhesive properties, SBPs have demonstrated an ability to promote inorganic precipitation and gain morphogenetic control. [34–37]

1.1.2 Biomimetic silica mineralization

Silicon dioxide (SiO_2, commonly referred to as silica) is one of the most ubiquitous compounds in nature, making up more than a quarter of Earth's crust by weight. Many forms of silica are fairly common in our daily lives especially quartz, a form of crystalline silica, which happens to be the second most common mineral found on earth.[38,39] Silica biomineralization, the natural process of precipitating silica, has been observed in simple organisms capable of producing silica from abundant silicon and oxygen in their environment. This process expands across length scales starting with single-cell diatoms producing nanopatterned silica shells for protection, to supporting the skeletal structure of sponges in the deep sea.[20,40,41]

Silica-based nanomaterials have been used for decades in applications ranging from catalysis to controlled drug release, and from antimicrobial coatings to enhanced oil recovery. This broad range of uses has been driven by the low cost of silica, its thermal stability and biocompatibility, and by the fact that the material's size, morphology, and surface chemistry are all tunable.[42,43] While colloidal silica is typically synthesized at scale by liquid- (e.g. Stöber) or gas-phase methods,[43] more complex architectures, such as zeolites, can be accessed by macromolecular templating.[44] However, no synthetic process approaches the sophistication of diatoms which build intricately structured siliceous cell walls with extraordinary optical and physical properties by controlling silica deposition with proteins and other biomacromolecules.[45,46] In seminal work on biomimetic silica, Kröger *et al.* isolated a set of cationic peptides from the cell wall of *Cylindrotheca fusiformis* and demonstrated their role in mediating silicification under ambient conditions.[18] The so-called silaffins (for silica affinity), and notably a constituent 19-mer

peptide called R5, were capable of mineralizing silica nanospheres from silicic acid in mild conditions.[18] Their early work suggested that post-translational modifications (PTMs) found in silaffins significantly improved their silicification activity, which was further confirmed by experimental and simulation studies.[47–49] They have also been extensively studied to uncover the roles of sequence, side-chain chemistry, oligomerization, and solution conditions on silica polycondensation.[19–21,39,50–53]

Other biomolecules have proven useful to manipulate the precipitation and organization of silica. For instance, poly(lysine), poly(arginine),[54] and long-chain polyamines[50,51] induce silica precipitation with high activity, while short peptides can template more sophisticated silica structures.[19,21,55,56] Solid-binding proteins, which combine the adhesive or morphogenetic activities of guest SBPs with the structural or functional properties of a host protein framework, are a valuable addition to this arsenal.[23,57] For example, Car9, a silica-binding peptide,[28,29] was genetically fused to superfolder green fluorescent protein (sfGFP) to study silica adhesion regimes,[30,31] print protein patterns on microscope slides,[58] and create multi-material hierarchical architectures.[27,33,59,60]

1.1.3 Biomimetic titania mineralization

Titania-based nanomaterials are highly desirable for their enhanced optical and electrochemical properties that can be exploited for catalysis, sensing, protective coatings, solar energy conversation and storage, and pigments.[61–63] Early studies demonstrated that silaffin-derived peptides and proteins exhibit an affinity to SiO_2- and TiO_2- based nanomaterials. This led to the exploration of silaffin-derived biomacromolecules as TiO_2 mineralization templates under ambient conditions. [63–65] This

inspired recent TiO_2 mineralization work using Car9, which has been well characterized for its binding affinity to SiO_2, to control size, particle distribution, and crystalline phase of mineralized TiO_2 inclusions. [36,59] Importantly, Puddu *et al* demonstrated the first biomimetic TiO_2 synthesis approach using TiO_2-binding peptides Ti-1 (QPYLFATDSLIK) and Ti-2 (GHTHYHAVRTQT) which exhibited TiO_2 mineralization activity and produced stable 10-nm sols.[35]

1.1.4 Biomimetic gold mineralization

Plasmonic nanoparticles, commonly Au, Ag and Cu, exhibit unique optical properties that have been exploited in art works and architectures dating back to the Roman Empire, centuries before the evolution of modern nanotechnology. Their optical properties arise from a phenomenon known as localized surface plasmon resonance (LSPR) that is highly dependent on the nanoparticles' size, morphology, polydispersity, and spatial arrangement. Thus, it is desirable to gain precise control over their synthesis.[66]

The A3 peptide (AYSSGAPPMPPF) was originally selected, along with two other dodecapeptides, from a combinatorial phage display library for its binding affinity to silver particles.[67] A later study by Slocik *et al* found that A3 binds to both gold and silver surfaces possibly via hydrophobic interactions and hydrogen bonding between the peptide side chains and the metallic surfaces. They also demonstrated that A3 is capable of synthesizing and stabilizing AuNPs from a solution of $HAuCl_4$ precursor in reducing conditions.[68] The synthesized AuNPs were successfully functionalized with different chemistries to enable hierarchical material assembly and use in biosensing and imaging.[69] These findings inspired many more studies that focused on fine tuning Au mineralization mediated by A3 peptide and achieving sophisticated architectures and

functionalities.[59,70–72] For example, Chen *et al* incorporated A3 into an amphiphile peptide that can self-assemble into highly ordered double helices displaying the Au-mineralizing A3 moieties which mediated the precipitation of discrete spherical AuNPs.[73] Au-based nanomaterials have been developed for a large variety of applications including drug delivery, diagnostics, cancer treatments, chemical and biological sensing, catalysis, and others.[74–77]

1.2 Stimuli responsive and functional nanomaterials

The interest in stimuli-responsive nanomaterials has significantly grown in the fields of electronics,[14,15,78] catalysis,[79–82] novel materials,[83,84] and medicine[85,86] owing to their unique mechanical and optical properties, programmability, and specificity. These materials can respond to a wide range of environmental triggers such as pH, temperature, irradiation, the presence of ions, and electrical or magnetic fields by undergoing compositional, structural, or morphological changes, assembly/disassembly, actuation, motion, etc. [87,88] While a wide range of stimuli-responsive nanomaterials have been developed, the synthetic thermoresponsive polymer, poly(N-isopropylacrylamide) or PNIPAM, has been extensively used for the production of temperature-responsive materials.[89,90] PNIPAM hydrogels exhibit lower critical solution temperature (LCST) behavior, transitioning from a swollen, extended state to shrunken phase-separated hydrophobic coacervates when the solution temperature is increased above the cloud point (about 32°C in water at moderate polymer concentrations).[91] Numerous studies have demonstrated that PNIPAM can be used independently or within more complex structures to capture and release drugs and other molecules.[92–95] However, they have uncovered the fact that PNIPAM coacervates have a limited loading capacity and a

relatively slow response to temperature. In addition, PNIPAM has been used to decorate plasmonic nanoparticles to endow them with temperature-triggered actuation at psychologically relevant temperatures that resulted in a reversible LSPR shift. This dynamic process can be used for applications like spectroscopy and biosensing.[82,96,97]

Elastin-like polypeptides (ELPs) are a class of stimuli-responsive disordered proteins derived from the elastin protein found in the extracellular matrix of connective tissues in humans. They contain long repeats of the sequence VPGXG (where X is a guest residue that can be any amino acid except for proline) and exhibit LCST behavior that can be tuned by changing the guest residue identity, chain length, and solution conditions (pH, salt concentration, co-solvents).[98–102] Because of their monodispersity, tunable LCST properties, and enhanced stability, ELPs have been explored as alternatives to PNIPAM as early as the 1990s.[103,104] ELP-based materials have been developed for various applications including drug delivery,[105–108] tissue engineering,[109] imaging,[110] hierarchical self-assembly,[111–113] and mineralization of inorganic nanoparticles.[114,115]

1.3 Figures

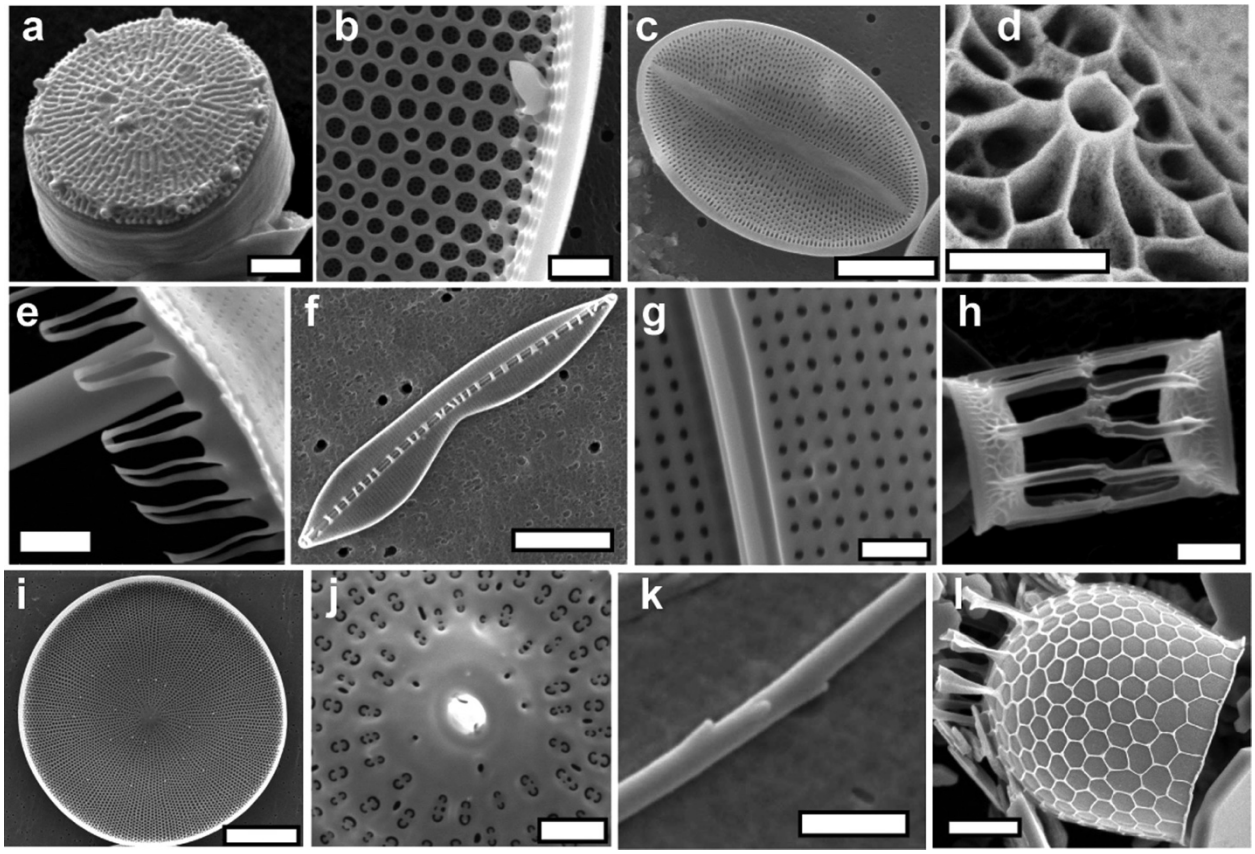

Figure 1.1 Micrographs of diatom silica nanostructures. Scale bars are 1 μm (a and k), 5 μm (b), 10 μm (c, f, and l), 500 nm (d), 2 μm (e, g, h, and j), and 50 μm (i). Adapted from Ref [45]

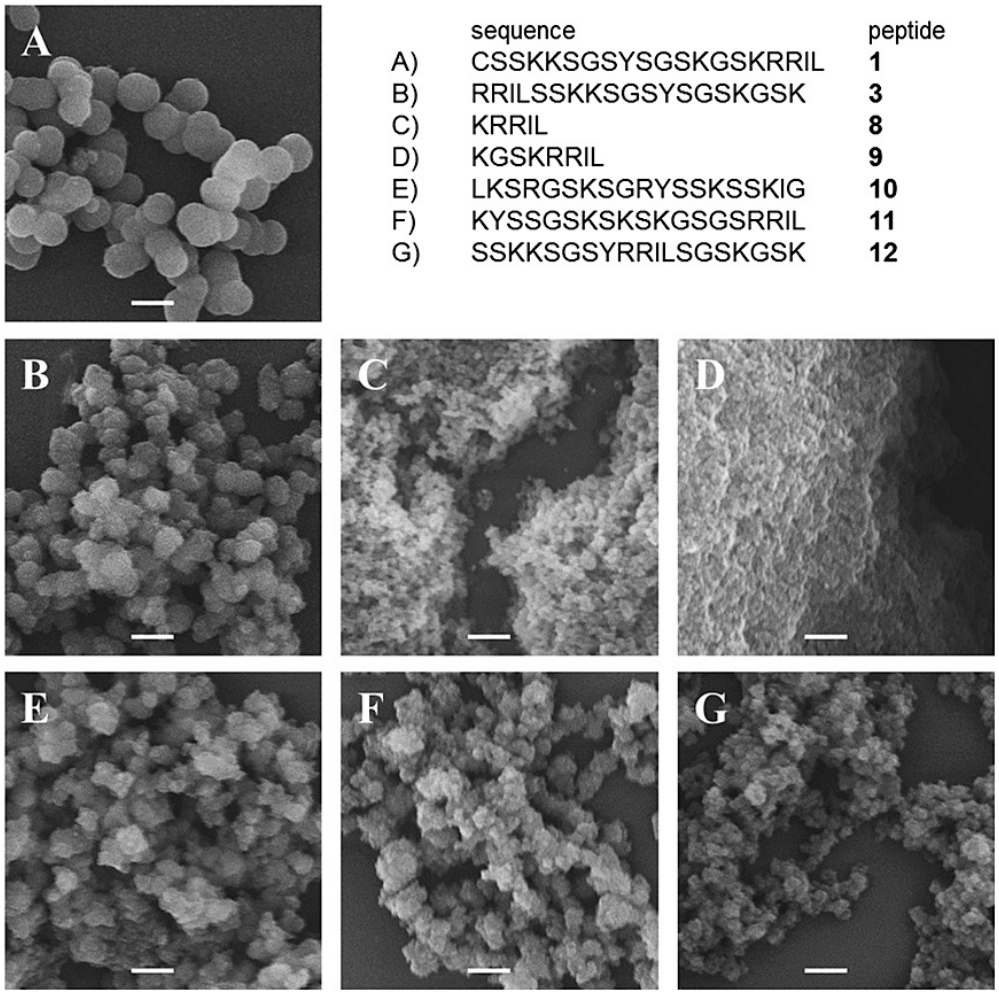

Figure 1.2 Micrographs of silicas particles mineralized in solutions of R5 peptide variants shown. Scale bar is 1 μm. Adapted from Ref [21]

Chapter 2 Biomimetic mineralization of positively charged silica nanoparticles templated by solid-binding elastin-like polypeptides

2.1 Introduction

Silica-based nanomaterials have been advantageous for a variety of industrial and biomedical applications which include catalysis, energy conversion, controlled drug release, sensing, anticorrosion, antimicrobial coatings, and enhanced oil recovery.[116–119] Although silica nanoparticles can be synthesized at scale by simple liquid- or gas-phase methods,[43] no synthetic process approaches the sophistication of natural systems (e.g. diatoms and sponges) that employ biomacromolecules to mediate, template, or control the precipitation of silica with intricate nanostructures and complex hierarchy. Many biomimetic approaches towards tailored nanoscale silica synthesis have exploited both bio-inspired and rationally designed biomacromolecules to template silica mineralization and organization under neutral pH and low temperature conditions. As such, it has been established that silica-binding peptides can induce the condensation of silicic acid in mild aqueous conditions and modify the reaction kinetics and morphology of the precipitated silica.[55,120] However, little attention has been paid to fusing these peptides to stimuli-responsive proteins to bias the outcomes of silicification. Elastin-like polypeptides (ELPs), a class of thermoresponsive intrinsically disordered proteins derived from the human tropoelastin protein, are particularly attractive for this purpose. These low-complexity proteins consist of long repeats of the VPGXG pentamer, where the guest residue X can be any amino acid except for P. They exhibit LCST behavior and form phase-separated droplets, or coacervates, above a characteristic transition temperature (T_t)[103,121] that can be tuned by changing the identity of the guest residue, the overall chain length, and the

solution conditions (e.g., pH, salt concentration, and the presence of co-solvents).[98–102] ELPs have found many uses in biomedical applications,[122–124] hierarchical self-assembly,[106,111–113] and inorganic nanoparticle mineralization.[114,115]

In this chapter, we use the silica-binding ELP V54-Car9, a fusion protein between a 54-repeat of the VPGVG sequence and the Car9 silica-binding peptide, to conduct a detailed study of how temperature driven self-assembly influences silicification. We show that increasing the temperature by 5°C above the T_t of the ELP block leads to a transition from extended, disordered ELP unimers to 30-nm self-assembled micelles. We demonstrate that whereas both species support self-limiting silica precipitation in the absence of biological buffer, micelles template the mineralization of highly monodisperse 62 nm NPs while V54-Car9 unimers produce polydisperse NPs with a mean diameter of 133 nm. NPs mineralized at both temperatures exhibit a net positive charge that we attribute to the surface exposure of cationic sidechains that are not involved in the polycondensation process. We take advantage of the monodispersity, stability, and the positive charge of the silica NPs produced at high temperature for the solution-based, electrostatically driven assembly of a range of hierarchical architectures using unmodified silica and gold NPs as assembly partners.

2.2 Materials and Methods

2.2.1 DNA manipulations and protein purification

An ELP gene encoding 96 repeats of the VPGVG sequence[125] was amplified using Addgene plasmid pET25b(+)-V96 (number 68392) as a template. Primer pair 5'-ATTCGAGCTCCGTCGACAGGCTTG-3' and 5'-TCGGATCCTGAAGATCATTATCAAAGCTTACCTACACCC-3' introduced a unique

HindIII site at the 3' end of the gene to enable modular insertion of solid-binding peptides at the C terminus of the gene product. Non-specific priming to repeated oligonucleotides regions in the V96 template resulted in amplification products of variable lengths. A product encoding 54 repeats of VPGVG followed by a KLGGGS flexible linker specifying a HindIII restriction site was recircularized yielding pET25b(+)-V54. To create gold- and silica-binding derivatives, the *V54* gene was excised by NdeI-HindIII digestion of pET25b(+)-V54 and ligated into the same sites of pET24a(+)-sfGFP(G51C)-A3 or pET24a(+)-sfGFP(G51C)-Car9, generating pET24a(+)-V54-A3 and pET24a(+)-V54-Car9, respectively.[59] An isogenic plasmid encoding the V54-KLGGGS control polypeptide, pET24a(+)-V54, was constructed by digesting pET24a(+)-V54-Car9 with HindIII and XhoI and ligating the backbone with a DNA cassette obtained by hybridizing the 5'-AGCTTGGCGGCGGCTCTTAATAAC-3' and 5'-TCGAGTTATTAAGAGCCGCCGCCA-3' oligonucleotides. Plasmids were transformed into *E. coli* Top10 and verified by Sanger sequencing. Verified plasmids were introduced into BL21(DE3) cells. For protein expression, overnight cultures of BL21(DE3) cells harboring pET24a(+)-V54, pET24a(+)-V54-A3, or pET24a(+)-V54-Car9 were grown at 37°C in 5 mL of LB medium supplemented with 50 µg/mL kanamycin and used to inoculate 250 mL of Terrific Broth (TB) supplemented with the same antibiotic. Cells were grown at 37°C without induction for 24 hours before cell paste was harvested by centrifugation at 4,000*g* for 20 min, resuspended in 25 mL of 20 mM Tris-HCl, pH 7.5, and disrupted by two cycles of sonication for 9 min each (10s on, 20s off) at 30% amplification (Fisherbrand Sonic Dismembrator). Cell lysates were supplemented with 1 mL of 10% polyethylenimine (PEI), incubated on ice for 10 min, and centrifuged at

10,000*g* for 20 min at 4°C to remove insoluble materials and precipitated nucleic acids. ELPs were purified by inverse transition cycling (ITC)[103]. Each cycle started with ELP precipitation by adding 3 M of crystalline NaCl to the supernatant. After vigorous shaking, the mixture was rotated at 40 RPM for 30 min at room temperature and centrifuged at 4,000*g* for 20 min at 40°C. Soluble impurities were removed with the supernatant and the ELP-containing pellet was resuspended in 20 mL of pre-chilled DI water and rotated as above at 4°C. Finally, the solution was centrifuged at 10,000*g* for 20 min at 4°C and the supernatant was subjected to an additional cycle of ITC. The purity of the final products was verified by Coomassie Blue-staining of SDS-PAGE minigels as shown in **Fig 2.1B**. Concentrations were determined by measuring the absorbance at 205 nm and using calculated extinction coefficients[126] of 764500, 814370, and 809160 $M^{-1}cm^{-1}$ for V54, V54-A3, and V54-Car9, respectively. Samples were stored at 4°C until further use.

2.2.2 Characterization and quantification of solid-binding ELP constructs

Phase transitions of the protein solutions were monitored by UV-visible spectroscopy and dynamic light scattering (DLS). For UV-visible spectroscopy, A_{350} was measured as a function of temperature on a Cary 3500 spectrophotometer equipped with a Peltier temperature controller (Agilent Technologies) using a ramp rate of 1°C per min. Protein solutions (700 µL at a concentration of 75 µM) were blanked against the appropriate reference (DI water, 20 mM Tris-HCl at pH 7.5, or 100 mM HEPES at pH 7.3) in semi-micro quartz cuvettes. The lower critical solution transition temperature of each protein (T_t) was determined based on inflection point analysis of the A_{350} turbidity profiles. A Zetasizer Nano ZS (Malvern) was used to measure D_h as a function of temperature.

Triplicate samples (1 mL) were incubated at each temperature for 5 min before DLS measurements were acquired.

2.2.3 Silica mineralization

Silica mineralization reactions were conducted as described by Kröger *et al.*[18] Stock solutions of 1 M silicic acid were freshly prepared by mixing 150 µL of tetramethyl orthosilicate (TMOS, 98%, Sigma) with 850 µL of 1 mM HCl, vortexing the solution for 5 min, and rotating it for 10 min at room temperature. Aliquots (100 µL) were added to 900 µL of V54-Car9 or V54 to reach final concentrations of 100 mM silicic acid and 75 µM proteins. Solutions were immediately mixed by inverting 5 times and the reaction was allowed to progress for 8 h in water. For mineralization reactions above T_t, protein solutions were pre-incubated for 10 min in a water bath held at 45°C prior to addition of silicic acid and the reaction was allowed to proceed for 8 h at the same temperature. Silicification products were characterized as described below. When indicated, aliquots (500 µL) were transferred to 50 kDa cutoff, 10 nm pore size, Float-A-Lyzer devices (Repligen, Waltham, MA) and were dialyzed twice against 300 mL of DI water (with stirring) for 2 h at room temperature, and a final round of dialysis was conducted overnight.

2.2.4 Analytical techniques

Small angle x-ray scattering (SAXS) data were collected by Will Wixson on a Xeuss 3.0 (Xenocs) using Cu K_α radiation and processed with the XSACT software (Xenocs).

For scanning electron microscopy (SEM), samples were diluted 100-fold in deionized (DI) water, and aliquots (5 µL) were deposited on silicon wafers that were allowed to air

dry overnight. For mineralization reactions above T_t, samples were diluted 100-fold in DI water pre-heated to 45°C, deposited on pre-heated silicon wafers, and allowed to air dry overnight in an incubator held at the same temperature. Images were acquired on an Apreo-S SEM (Thermo Scientific) operated at 2 kV and 13 pA.

For transmission electron microscopy (TEM), samples were diluted 10-fold in DI water. Aliquots (10 µL) were deposited on carbon-coated copper grids (Electron Microscopy Sciences and Ted Pella) and allowed to sit for 5 min before excess solution was wicked out with a laboratory tissue. Images were acquired on a Tecnai F20 SuperTwin TEM (FEI) at an acceleration voltage of 200 kV and analyzed using ImageJ (NIH).

For atomic force microscopy (AFM), aliquots (10 µL) of samples were deposited onto freshly cleaved mica substrates (Ted Pella). After 5 minutes, excess water was wicked out with laboratory tissue and samples were further dried by evaporation. AFM images were captured in the dry state using the tapping mode on an ICON AFM (Bruker) and Multi75Al-G probes. Offline AFM data processing was performed using Gwyddion software.[127]

Thermogravimetric analysis (TGA) was conducted on lyophilized mineralization products that had been extensively dialyzed to remove free and loosely bound proteins. Experiments were performed in a Q50 TGA instrument (TA Instruments). Lyophilized powder was loaded into an alumina crucible on platinum tray and heated to 800°C at a ramp rate of 20°C per min in air (100 mL/min).

2.3 Results

2.3.1 V54-Car9 forms micelles above its transition temperature

To combine the mineralization properties of a solid-binding peptide with the thermoresponsive phase segregation behavior of ELP, the sequence encoding the Car9 dodecapeptide (DSARGFKKPGKR) was fused to the C-terminus of a 54-repeat of the VPGVG sequence via a flexible KLGGGS linker (**Fig. 2.1**). A control protein lacking the Car9 dodecapeptide (denoted V54) exhibited characteristic LCST behavior[103,121] with a sharp increase in both the absorbance at 350 nm (A_{350}) and the hydrodynamic diameter (D_h) as the temperature exceeded a T_t of 40°C (**Fig. 2.2**, black traces). In contrast, V54-Car9 only experienced a transient peak in turbidity between 42 and 48°C before reaching a slightly higher value as the temperature increased (**Fig. 2.2**, orange trace). Results were well explained by DLS measurements showing that the D_h of V54-Car9 increased from 8 to 540 nm between 42 and 45°C before declining to about 30 nm over the next 2-3°C. To gain insights on kinetics, we monitored the D_h at 65°C, a temperature that far exceeds its T_t (~45°C). Within two minutes, V54-Car9 molecules transitioned from unimers to intermediate aggregates ranging in size from 200 to 300 nm (**Fig. 2.3**). These species progressively disappeared after 3 minutes to the profit of a peak centered at a D_h of 30 nm.

Similar phase transitions have been reported for amphiphilic block copolymers,[87,128–132] including those consisting of a hydrophobic ELP block (where the guest residue is V) fused to a hydrophilic ELP block (where the guest residue is G, A, or S). For such diblock ELPs, a temperature increase above the T_t of the hydrophobic block leads to the formation of spherical micelles displaying the hydrophilic block on their exterior.[133–139]

This feature was exploited by Lopez and coworkers to display the 19-residue long R5 peptide on the surface of 50 nm micelles by fusing it to a 300-residue long hydrophilic block that was itself fused to a 300-residue long hydrophobic block.[112,114,137]

We used SAXS (conducted by Will Wixson) to determine if V54-Car9 adopted a similar micellar structure above 45°C despite lacking a long hydrophilic ELP block. Expectedly, the SAXS profile of V54-Car9 at 22°C was consistent with that of polymeric random coils and intrinsically disordered proteins.[31,140] Analysis of the profile at $T > T_t$ (45°C) revealed that 140 ± 9 V54-Car9 molecules self-assemble to form a micelle with a 15 ± 0.2 nm core radius that is fully consistent with a D_h of 30 nm as determined by DLS. Consistent with a structure in which a coacervated V54 core is surrounded by cationic Car9 extensions, the ζ potential of the micelles was +19 ± 3 mV (**Table 2.1**). In short, our results show that the short Car9 peptide is sufficient to impart diblock behavior to a 54-repeat hydrophobic ELP and drive the formation of micelles at a T_t that is about 5°C higher than that of the ELP block.

2.3.2 Silica mineralization templated by V54-Car9 micelles and the influence of biological buffer on silicification products

To determine how temperature-induced micellization would influence silica precipitation outcomes, solutions of V54-Car9 in Tris-HCl buffer were heated to 45°C, supplemented with an excess of silicic acid and the silicification reaction was allowed to progress at 45°C (i.e. *hot synthesis*). Within 10 min, a significant increase in turbidity was observed accompanied by the sedimentation of large silica structures. Characterization of the precipitates revealed large, yet monodisperse, spherical silica particles with an

average diameter of 697 ± 49 nm under dry conditions (**Fig 2.4A**, N = 100), a D_h of 905 ± 42 nm, and a zeta (ζ) potential of -22 ± 0.4 mV.

How can 30-nm micelles of V54-Car9 template the formation of SiO_2 particles that are an order of magnitude larger in size? Previous studies with the R5 peptide and silaffins have postulated that the SiO_2 precipitation of these macromolecules is promoted by the interactions between the negatively charged silicic acid precursor molecules and the amine groups of serine and lysine residues.[19,114] It has also been suggested that the presence of cationic ions in the buffer can influences silica polycondensation pathway resulting in different silica structures in terms of size and morphology.[20,48,141] We therefore hypothesized that the formation of ca. 700 nm silica particles was due to accelerated reaction kinetics and fusion of primary silica nanoparticles templated by V54-Car9 micelles, mediated by the amine group of Tris. Further, solutions of the control protein (V54) held at 45°C produced larger particles with an average diameter of 1176 ± 458 nm under dry conditions (**Fig 2.4B**, N = 100) that exhibited a higher degree of polydispersity, which were likely templated by the large coacervates above T_t. These findings support a dominant role of Tris ions in catalyzing silica polycondensation and supporting further growth of large particles regardless of the biomolecular template size or the reaction temperature.

To test this hypothesis, *hot synthesis* was conducted in DI water**. Unlike what was seen in the presence of Tris, there was no obvious precipitation after 10 min of reaction at 45°C**. The reaction was allowed to progress at the same temperature for 8 h and D_h was measured at intermediate times to monitor particle growth. An increase in turbidity correlating with an increase in D_h (62 nm) was observed within 30 min, with no

further evolution over time **(Fig. 2.7**, red trace). SEM (**Fig. 2.5A-B**) and TEM (**Fig. 2.5C**) revealed the production of monodisperse NPs with an average diameter of 56 ± 4 nm (*N* = 100) under dry conditions.

Conducting the silicification experiment at 22°C (i.e. *cold synthesis*), where 8-nm V54-Car9 unimers dominate rather than 30-nm micelles, led to the formation of slightly larger particles (D = 96 ± 16 nm, *N* = 100) that exhibited a higher degree of polydispersity and to the production of occasional aggregates (**Fig. 2.6**). A DLS time course study (**Fig. 2.7**, blue trace) showed that little growth occurred after two hours of *cold synthesis* in the absence of Tris-HCl. Consistent with imaging results, polydispersity index (PDI) values from DLS measurements were 0.03 and 0.12 for the products of *hot* and *cold synthesis*, respectively, in absence of Tris.

Control experiments showed that the V54, which lacks the Car9 extension, mineralizes polydisperse ~1 μm spherical particles in the presence of Tris-HCl, but that silica precipitation lacks morphological control in DI water (**Fig. 2.8A-B**) Further, minimal silica precipitation was observed when silicic acid was added to DI water in the absence of protein over a period of days (**Fig. 2.8C**).

We conclude that by virtue of exposing Car9 extensions on their corona, V54-Car9 micelles provide multiple cationic sites that trigger instant nucleation of silica. In water, the reaction is self-limiting and polycondensation stops after a silica shell thickness of about 20 nm has been produced. Nucleation is more random with the V54-Car9 unimer (i.e., below the T_t) resulting more polydisperse particles. In addition, Tris ions are not mere spectators of the reaction as they mediate silica polycondensation and the ultimate production of near micron sized silica.

The SAXS profiles of synthesis products at both temperatures were consistent with spherical particles. They also exhibited a turnover at high *q*-values that is indicative of small surface features (**Fig. 2.9A**). We therefore used a spherical raspberry model[142] instead of a simpler sphere model to fit the scattering data. This analysis confirmed that the *hot synthesis* products are highly monodisperse silica spheres with a mean core diameter of 55 ± 3 nm and a PDI of 0.12 (**Fig. 2.9B**, red). The turnover in scattering was successfully modelled as uniform projecting hemispheres that were 2 ± 0.2 nm in diameter (**Fig. 2.9C**). On the other hand, the scattering profile of the *cold synthesis* products (**Fig. 2.9A**, blue) lacked strong secondary peaks and had a steep negative slope at low q-values, which is indicative of polydispersity. Indeed, the fitting procedure revealed particles with a mean core diameter of 116 nm, a larger PDI of 0.18, and surface features that could be modelled as hemispheres 1.6 ± 0.4 nm in diameter (**Fig 2.9B**, blue). We confirmed that protrusions were present on the surface of both particles using tapping-mode AFM and high-resolution transmission electron microscopy (HRTEM) shown in **Fig. 2.9D-I**. In agreement with the SAXS data, these nodules were more uniform and regularly distributed on the surface of *hot synthesis* products (**Fig. 2.9D-F**). With a diameter of ~3 nm determined from TEM data and ~2 nm from SAXS data fitting, these small particles are likely to correspond to the primary units that make up biomimetic silica structures.[20]

2.3.3 Studying reaction kinetics and surface charge

Several scenarios can account for the formation of silica particles of defined sizes including exhaustion of the silicic acid precursor, termination of growth by capping, and self-limiting growth. With an over 1,300-fold molar excess of silicic acid to proteins, the first possibility appeared unlikely. Indeed, when both *cold* and *hot synthesis* products

were supplemented with additional V54-Car9 at room temperature after the initial mineralization reaction, we observed additional silica precipitation, indicating that free silicic acid remains available in solution despite the observed cessation of nanoparticle growth (**Fig. 2.10C-D**). However, and unlike in the *cold synthesis* case, the products of the reaction were micrometer sized silica islands that grew around the pre-mineralized nanoparticles and likely did not form silane bonds with them (**Fig 2.10C**, yellow arrow). We attribute this result to a slower growth of the silica matrix due to depletion of the precursor in the initial mineralization phase and concomitant diffusion limitations.

Consistent with a unique surface chemistry, our templated NPs exhibited a positive ζ potential of about 40 mV (**Table 2.1**) as well as long-term colloidal stability following extensive dialysis against water and storage at 4°C. X-ray photoelectron spectroscopy (XPS) of the oxygen and nitrogen signals confirmed the presence of organics at, or within the first ~10 nm of the surface (**Fig. 2.11**). This result was quite unexpected, as protein and peptide inducers of silicification typically become fully encased within the growing silica matrix, leading to a negative ζ potential.[19,44,143]

Table 2.1 summarizing the silicification reaction conditions and characterization of mineralized silica NPs in DI water.

[Si(OH)$_4$] (mM)	**Reaction Temp** (°C)	**Reaction Time** (h)	D_h DLS (nm)	D SEM (nm)	R_g SAXS (nm)	D_{sphere}* (nm)	**ζ Potential** (mV)
0	22	N.A.	8 ± 1	N.A.	5	N.A.	8 ± 5
0	45	N.A.	31 ± 8	N.A.	13	34	19 ± 3
100	22	8	133 ± 32	96 ± 16	49	127	38 ± 0.4
100	45	8	62 ± 10	56 ± 4	24	62	39 ± 0.1

* D_{sphere} was calculated based on R_g using the relationship: $D_{sphere} = 2 \times \sqrt{\frac{5}{3}} R_g$ [144]

To rationalize the positive ζ potential displayed by the mineralized silica, we conducted a series of experiments to verify whether V54-Car9 unimers were merely bound to the particles' surface or if they were partially embedded within the silica matrix leaving cationic sidechains emanating from the particles' surface. First, extensively dialyzing the nanoparticle solution against water did not change the ζ potential over the course of seven days, reflecting the strong surface interactions or the integration of the proteins within the particles. Second, and in contrast with our recent results with ELP-decorated AuNPs,[145] neither the *cold* nor the *hot synthesis* products experienced an increase in D_h when the solution temperature was raised to 55°C to induce colloidal aggregation via coacervation of any surface exposed ELPs (**Fig. 2.10B**). This finding strongly suggests that the ELP segments are embedded within the silica matrix rather than being available at the surface of the particles. Finally, TGA of 65-nm commercial silica nanoparticles that had been decorated with V54-Car9 revealed an onset of organic pyrolysis at about 250°C (**Fig. 2.10A**, orange trace). This temperature increased to 290°C for the *hot synthesis* and 300°C for the *cold synthesis* products, reflecting not only a more intimate integration of the proteins within the silica matrix, but also subtle differences in the nature of the interaction between the two types of nanoparticles.

2.3.4 Applications to electrostatic assembly of hierarchical and composite superstructures

We exploited the fact that nanoparticles mineralized under *hot synthesis* conditions are both positively charged and highly uniform in size to create colloidal assemblies through electrostatic interactions with unmodified NPs bearing an intrinsic net negative charge. In a first demonstration, we mixed the mineralized particles with an excess of

commercial, 10-nm silica NPs (**Fig. 2.12A**, *step 1*). This operation led to the decoration of the mineralized particles' surface with the smaller silica nanospheres and neutralized the ζ potential (**Fig. 2.12B**). In the resulting raspberry architecture, the 10-nm nanospheres were rather evenly separated from each other, as would be expected if they were experiencing a balance of attractive electrostatic interactions with discrete, positively charged regions of the mineralized particles, and electrostatic repulsion with each other. When an excess of mineralized nanoparticles was added to the product of the first assembly step (**Fig. 2.12A***, step 2*), SEM imaging revealed quantitative depletion of the 10-nm nanoparticles accompanied by the formation of an open, extended, and fractal-like networks, in which positively charged particles are connected to one another by the smaller silica nanospheres (**Fig. 2.12C**).

To demonstrate that different architectures can be accessed by manipulating the size of the unmodified silica NPs (**Fig. 2.13A**), we mixed the mineralized NPs with 20-nm commercial silica nanospheres. When the 20-nm particles were used at high concentrations (5-10 mg/mL), the mixture was colloidally stable and exhibited an overall negative ζ potential. Reducing the concentration 10-fold (to 0.5 mg/mL or about 75 μM) led to the formation of a white flocculate after overnight incubation at room temperature. SEM imaging revealed that this material consisted of rather tightly packed, multilayer aggregates of the two components (**Fig. 2.13B**) in which mineralized nanoparticles are interconnected by smaller, and oppositely charged silica nanospheres (**Fig. 2.13B** inset, yellow arrows).

We extended the approach to the production of a composite superstructure by mixing unmodified, 20-nm gold nanoparticles (AuNPs) with the mineralized silica. Overnight

incubation at the molar ratio used in the experiment of **Fig. 2.13B** led to the formation of a very similar architecture with bridging AuNPs well dispersed in the material (**Fig. 2.13C** and inset of **Fig. 2.13D**). Finally, and consistent with the lack of an adsorbed protein shell, HRTEM imaging showed an intimate interaction between the amorphous mineralized silica and the crystalline AuNPs (**Fig. 2.13D**).

2.4 Discussion

Micelle Formation by V54-Car9. Amphiphilic diblock copolymers have been extensively studied both theoretically[146–148] and experimentally[149,150] for their ability to self-assemble into a range of micellar structures,[151] with recent work focusing on combining the thermoresponsive properties of ELPs with diblock copolymer behavior to create temperature-responsive micelles.[137] In these applications, a hydrophobic ELP block (i.e., one that contains a hydrophobic guest residue such as V) is connected to a moderately hydrophilic block (e.g., an ELP with charged[136] or neutral[114] guest residues) or to a protein or a polymer[152,153] to create a construct with reversible thermoresponsive micellization behavior. In most cases, the hydrophilic block needs to be at least half as long as the hydrophobic block to form sub-100 nm micelles. Here, we showed that such long hydrophilic blocks are not required for micelle formation since the Car9 dodecapeptide is sufficient to confer diblock behavior to the V54 ELP despite representing less than 5% of the V54-Car9 amino acid sequence. Micellization arises 5˚C above the T_t of the ELP block in a process that involves the formation of intermediate aggregates 200 to 300 nm in size, and their subsequent resolution into highly monodisperse equilibrium structures that are 30 nm in diameter and comprise about 140 ELPs. This configuration provides about 20 nm^2 of surface area for the organization of a Car9 segment on the

micelle's exterior. Since Car9 can adopt a variety of conformations,[31] each core-tethered peptide must optimize the orientation of its sidechains to minimize destabilizing interactions with all its nearest neighbors. Considering that five of the 12 residues that make up Car9 are positively charged, this operation should lead to the presentation of a high density of basic side chains to the solvent, consistent with the appreciable ζ potential of approximately +20 mV. Whether the five basic residues of Car9 are necessary and sufficient to induce the formation of a well-behaved corona around the coacervated ELP core, and their role in this process, is currently being investigated.

Silicification by V54-Car9 micelles and unimers. The ability of V54-Car9 micelles to template the formation of highly monodisperse silica NPs when mixed with a solution of silicic acid in the absence of a buffer was not entirely unexpected. Han *et al.* previously reported that $ELP_{Diblock}$-R5, an amphiphilic ELP consisting of 60 repeats of the hydrophobic (GVGVP) sequence and 30 repeats of the hydrophilic (GAGVPGGGVP) sequence followed by the silaffin-derived R5 peptide (SSKKSGSYSGSKGSKRRIL), formed 50 nm micelles above a T_t of 33°C. When supplemented with silicic acid, these micelles templated the formation of silica NPs at 37°C.[114] However, there are two important differences between the results of this study and ours. First, the particles synthesized by Han and coworkers exhibited a negative ζ potential (-27 mV), indicating that the positively charged micelles were fully encapsulated in a mineral terminated by negatively charged silanol groups. Second, no silica precipitation was observed when silicic acid was added to dispersed $ELP_{Diblock}$-R5 unimers at 25°C.

Like $ELP_{Diblock}$-R5 micelles, V54-Car9 micelles are likely to serve as nucleation and growth centers for silica polycondensation by displaying a high density of positively

charged amino acids on their coronae. By analogy with a mechanism suggested for polyamine-mediated silicification,[154] we propose that the adsorption of silica monomers (or small oligomers) onto the amino groups of vicinal cationic side chains of Car9 promotes condensation reactions by bringing the inorganic species in proximity. This process leads to the formation of larger oligomers that grow into 1-3 nm particles.[20,155] These primary particles, which eventually come into contact and become linked by siloxane bonds, may be responsible for the surface features modelled by SAXS fitting and the granularity visualized in the TEM and AFM experiments in **Fig. 2.9**.

If similar silicification mechanisms are at play, why do $ELP_{Diblock}$-R5 micelles produce negatively charged silica particles while V54-Car9 micelles yield positively charged ones? A major difference between the two systems is that a 300-residue long hydrophilic block is present between the hydrophobic ELP block and the silica-binding peptide in $ELP_{Diblock}$-R5, relative to a six amino acids long linker in V54-Car9. Thus, R5 should experience considerably more degrees of freedom than Car9, which would facilitate interactions between primary particles and promote the encapsulation of the entire micelle. We propose that the lower mobility of coronal Car9 peptides and a stronger structural correlation with their neighbors introduces inwards directionality in the silica growth process that precludes complete encapsulation of the peptide. Using molecular dynamics (MD) simulations, we previously reported that three of Car9's basic residues (R4, K7, and K8, starting the numbering with the first residue) spend significant more time on silica surfaces relative to K11 and R12.[31] If a longer residence time on silica is indicative of a more active participation in the silicification process, the positive charge of mineralized

V54-Car9 micelles could be due to the side chains of K11 and/or R12 emanating from the surface of the mineralized silica.

Why do $ELP_{Diblock}$-R5 unimers *not* induce nanoparticle formation below T_t[114] while V54-Car9 unimers are effective at this task is well explained by the fact that Car9 is a better catalyst of silicification in water and phosphate-free buffers. Extensive literature indicates that the formation of R5 oligomers through the bridging action of phosphate ions[19,156] (or the post-translational phosphorylation of the peptide's serine residues)[48] significantly improves its silica precipitation ability. Additionally, a direct comparison of the ability of genetic fusions between green fluorescent protein (GFP) and the R5 or Car9 sequences revealed that whereas GFP-Car9 readily precipitated titania from the alkoxide-like precursor TiBALDH in mildly acidified citrate buffer, GFP-R5 was unable to do so.[36] A more interesting question is why do the NPs formed by V54-Car9 unimers under *cold synthesis* conditions also exhibit a positive ζ potential. We believe that this result is explained, at least in part, by the ability of Car9 to form oligomers when its R4, K7, and K8 anchor residues are engaged with silica.[31] While less efficient at templating the mineralization of uniform particles than V54-Car9 micelles, these small oligomers could still impart directionality to the silicification reaction, precluding encapsulation within the silica matrix and leading to the production of spherical particles that project cationic sidechains.

Electrostatic assembly of hierarchical architectures. Silica nanostructures exhibiting a positive surface charge have proven valuable for catalysis[157,158] and biomedical applications,[159–161] including controlled encapsulation and release of anionic drugs, surface decoration with DNA, efficient penetration of cell membranes, and

electrostatically-driven binding to negatively-charged cancer cells.[118] Reversal of the silica particles' native negative charge is usually achieved by adsorption of positively charged species or by chemical modification of the surface silanol groups (Si-OH) with cationic ligands. Unfortunately, these strategies often result in high polydispersity, poor colloidal stability, and/or silica dissolution.[118,162] Here, we described a simple approach to produce highly uniform positively charged silica nanospheres that exhibit exceptional colloidal stability and can be fabricated biomimetically under mild conditions without a need for multiple precursors, or post-synthesis surface modifications.[118,159]

These ready-to-use NPs were exploited to create 2- and 3-dimensional superstructures via electrostatically driven co-assembly with negatively charged NPs. From raspberry and fractal structures to more tightly packed composites, we achieved a broad range of architectures by changing the diameter, concentration, and composition of the anionic components. Although these proof-of-concept superstructures were obtained with little optimization and without annealing, we observed not only a rather uniform distribution of the two types of NPs in the final assemblies, but also the formation of intimate contacts between gold and silica components. This feature may be particularly valuable for the design of efficient catalytic and photoelectronic structures that exhibit high sensitivity to interfacial separation.[59,158,163,164]

2.5 Conclusions

We have shown that while a control ELP lacking a silica-binding extension undergoes hydrophobic collapse into micron-size coacervates above its T_t, the V54-Car9 silica-binding ELP self-assembles into 30-nm micelles displaying Car9 on their exterior, establishing that a short cationic peptide can impart diblock behavior to a large

hydrophobic ELP. We exploited these micelles to template the mineralization of highly uniform, positively charged silica NPs under mild conditions. Multimodal characterization of micellization kinetics and mineralization products provided insights into the self-limiting reaction and revealed nanoscale surface texture. Finally, we exploited the positive charge and monodispersity of NPs silicified at high temperature for the electrostatically driven, one-step assembly of hierarchical architectures, accessing a range of superstructures by modifying the size and composition of the negatively charged co-assembly partner. We anticipate that it will be possible to mineralize particles of different sizes, morphologies, and compositions by changing the sequence and length of the solid-binding segment and ELP block. This simple biomimetic approach to the synthesis of positively charged silica NPs and hierarchical and composite superstructures should prove useful for a broad range of biomedical applications and heterogeneous catalysis applications.

2.6 Figures

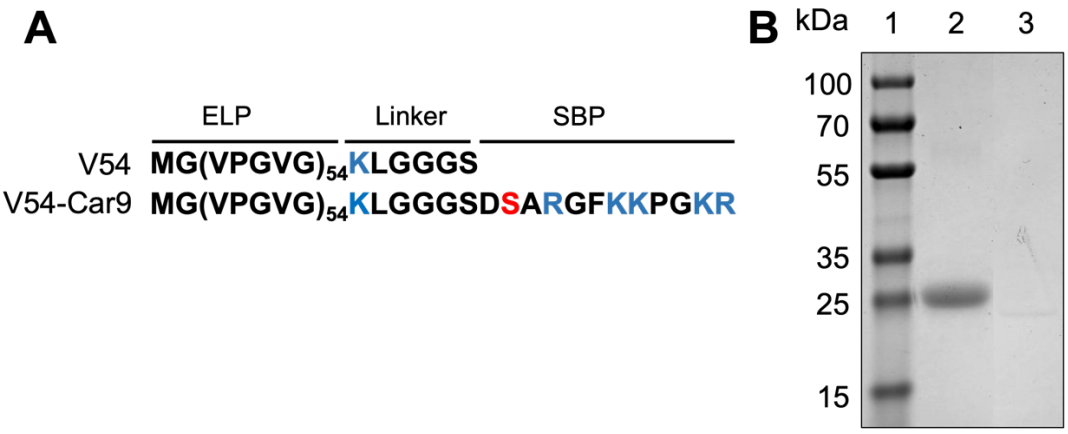

Figure 2.1 (A) Amino acid sequences of the V54 control protein and V54-Car9 silica-binding ELP. Positively and negatively charged residues are colored in blue and red, respectively . (B) Coomassie Blue-stained SDS-PAGE used to analyze V54-Car9 (lane 2) and V54 (lane 3) after two cycles of ITC purification. Proteins were diluted to 100 μM and boiled in SDS before loading. The staining of V54 by Coomassie Blue is inefficient due to the lack of charged residues.

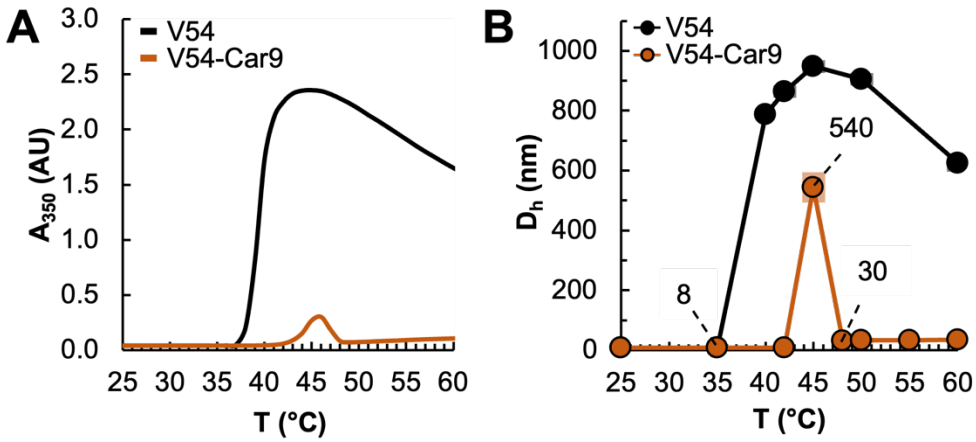

Figure 2.2 Temperature-dependent evolution of the turbidity (A) and D_h (B) of a 75 µM solution of V54 (black) or V54-Car9 (orange). Numbers in panel B correspond to the D_h of the different species.

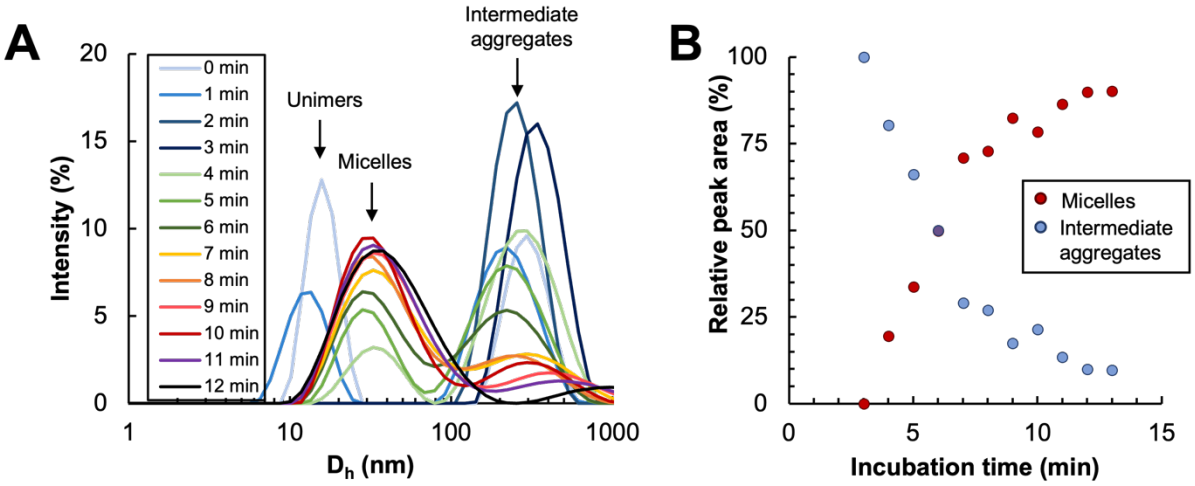

Figure 2.3 Kinetics of V54-Car9 micellization. (**A**) A 50 µM solution of V54-Car9 initially at room temperature was transferred to 65°C. DLS intensity profiles collected at the indicated time points show the transition of unimers to intermediate aggregates that progressively collapse into micelles. (**B**) Quantification of the evolution of intermediate aggregates (300 nm peak) and micelles (30 nm peak) over time.

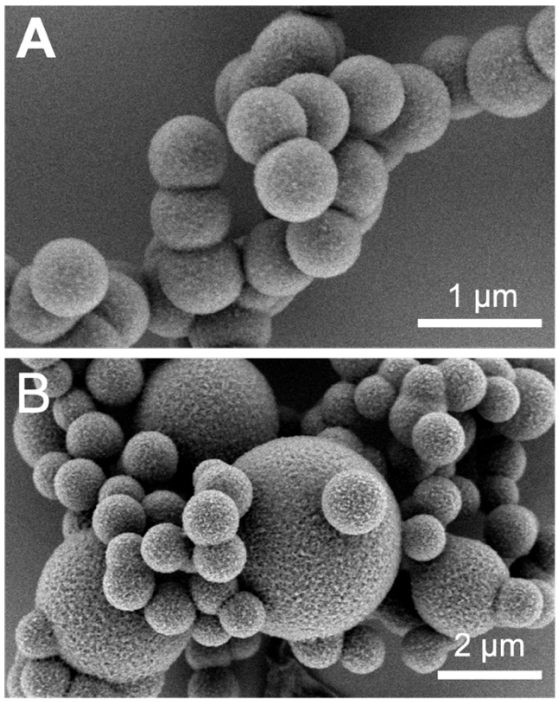

Figure 2.4 SEM images of silica particles mineralized in solutions of V54-Car9 (A) or V54 (B) in 20 mM Tris-HCl, pH 7.5 at 45°C.

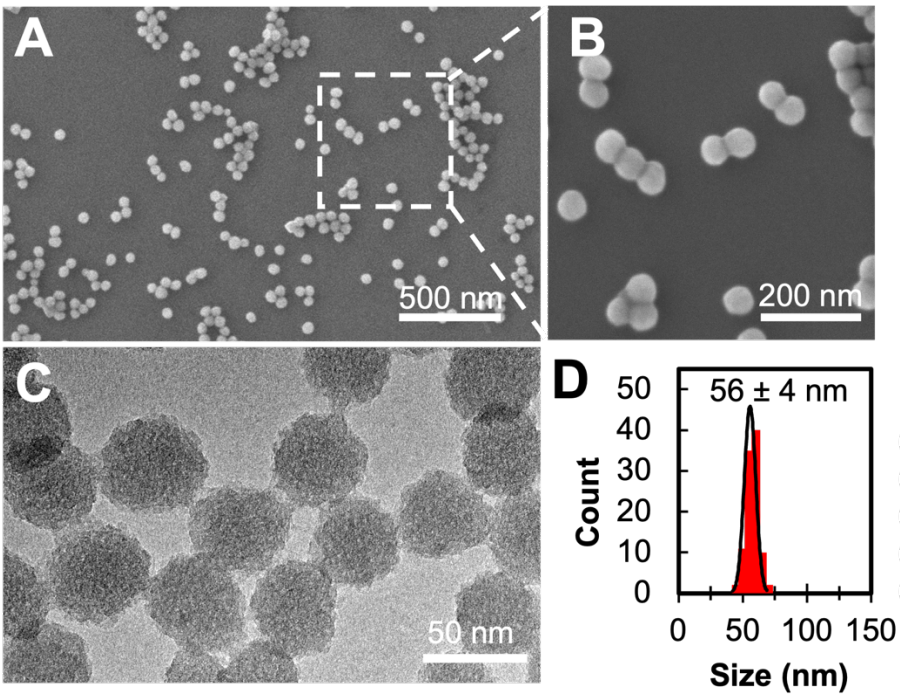

Figure 2.5 (A) Field of view and (B) magnified SEM images of mineralization products obtained at 45°C in DI water (*hot synthesis*), representative TEM image (C), and the corresponding particle size distribution (D).

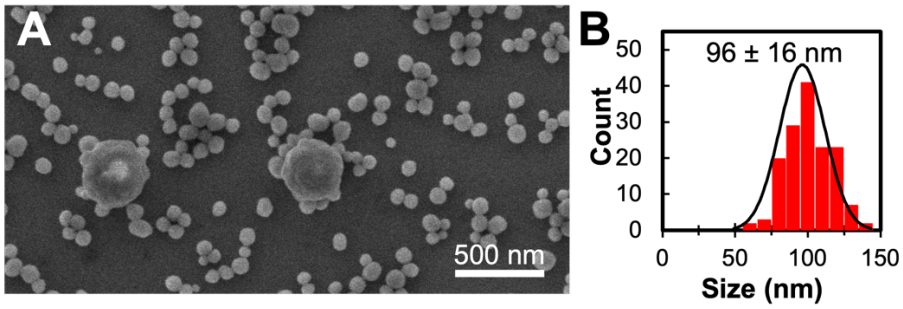

Figure 2.6 (A) Field of view SEM image of mineralization products obtained at 22°C in DI water (*cold synthesis*) and the corresponding particle size distribution (B).

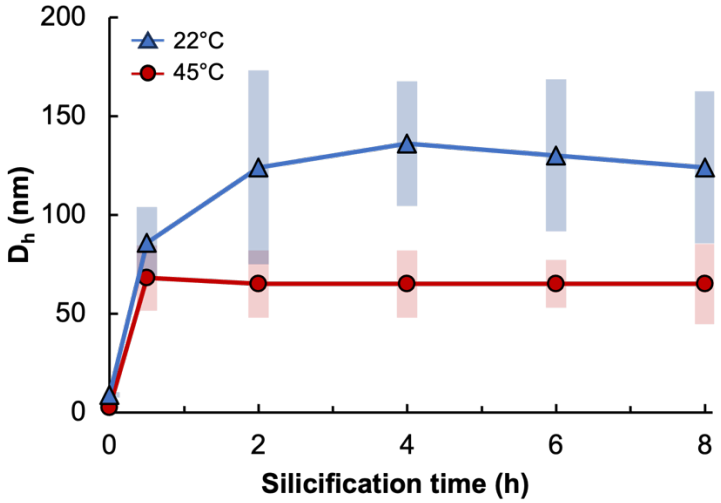

Figure 2.7 Kinetics of silica particle growth in the absence of Tris buffer at 22°C (blue triangles) and 45°C (red circles). Bars correspond to the full width at half maximum (FWHM) of the intensity size distributions measured by DLS. Experiments were conducted with 75 μM of V54-Car9 and 100 mM of silicic acid.

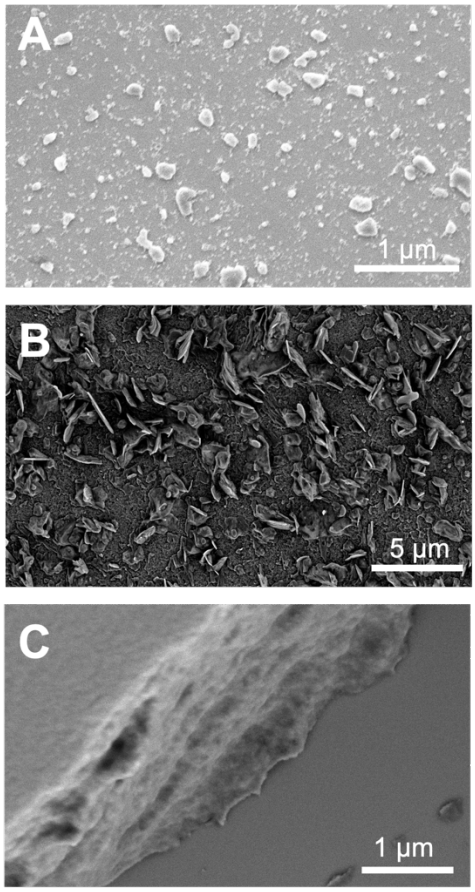

Figure 2.8 Mineralization controls lack size and morphology control. Representative field of view SEM image of silica mineralized in a solution of 75 µM V54 in DI water held at 45°C (A). SEM images of precipitation products obtained by incubating 100 mM of silicic acid at 45°C for 8h in 20 mM Tris-HCl, pH 7.5 (B) or DI water (C).

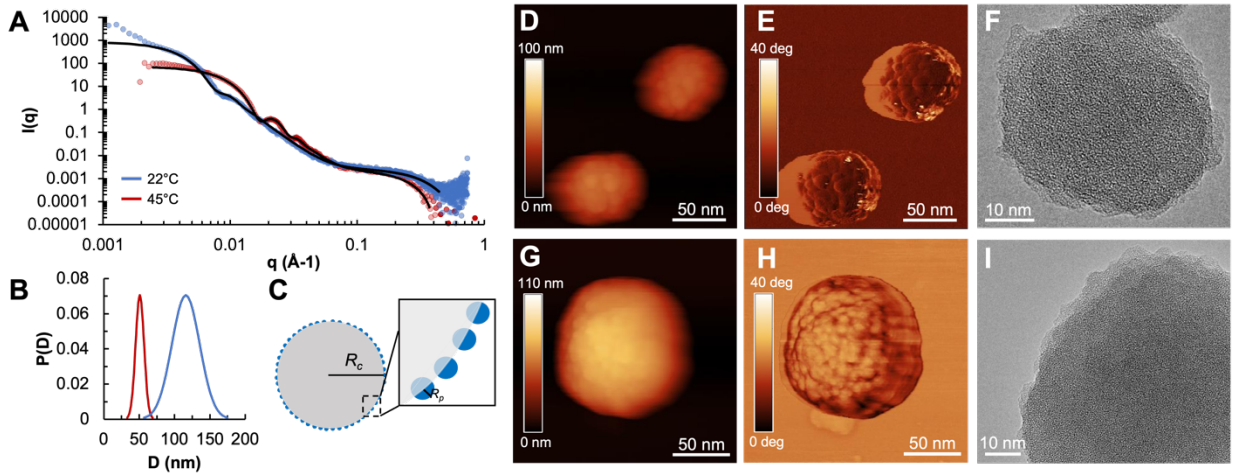

Figure 2.9 SAXS, AFM, and HRTEM characterization of silicification products. (A) SAXS profiles of silicification products obtained at 22°C (blue) or 45°C (red) fit to a raspberry sphere model (solid lines), (B) Distribution of core particle diameter from SAXS fit. (C) Schematic representation of the raspberry structure used for fitting of SAXS profiles. The core particles with radius R_c are decorated with embedded spheres of radius R_p, each with a projecting hemisphere. Tapping-mode AFM topography images (D, G), phase images (E, H), and HRTEM images (F, I) of NPs mineralized at 45 or 22°C, respectively.

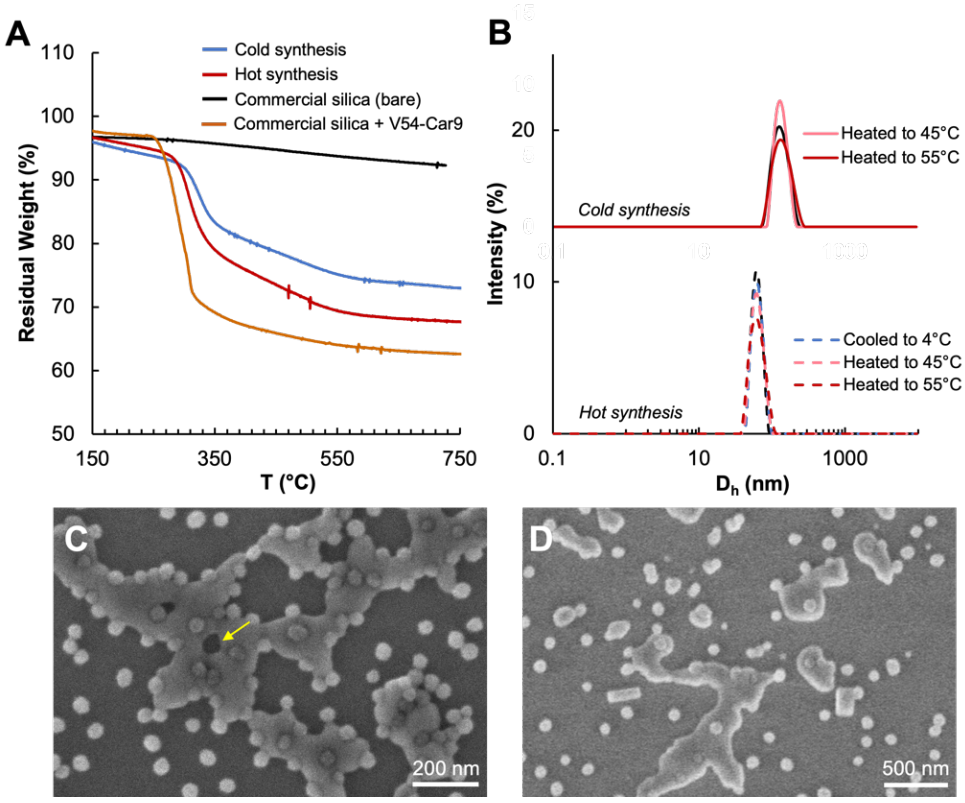

Figure 2.10 (A) TGA thermograms of *hot* (red) and *cold* (blue) *synthesis* products compared to commercial silica before (black) and after (orange) decoration with a molar excess of V54-Car9. All TGA samples were extensively dialyzed to remove loosely bound or unreacted ligands. (B) DLS intensity profiles of silicification products at 22°C (solid lines) or 45°C (dashed lines) after incubation at the indicated temperatures for 10 min each. SEM images of mineralized nanoparticles at 45°C (C) or 22°C (D) after the addition of 75 μM V54-Car9 and incubation for 10 min.

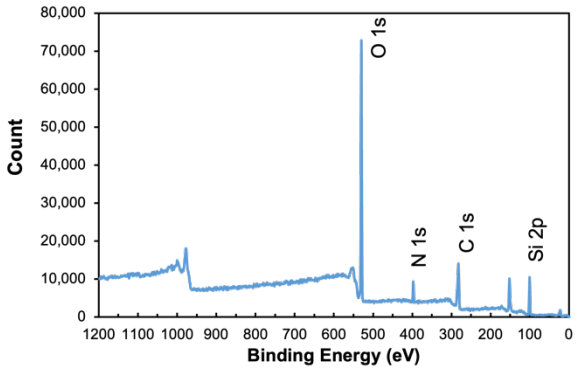

Peak ID	B.E. (eV)	Atomic %
O 1s	530	42.6
C 1s	282	37.0
Si 2p	101	15.3
N 1s	398	5.2

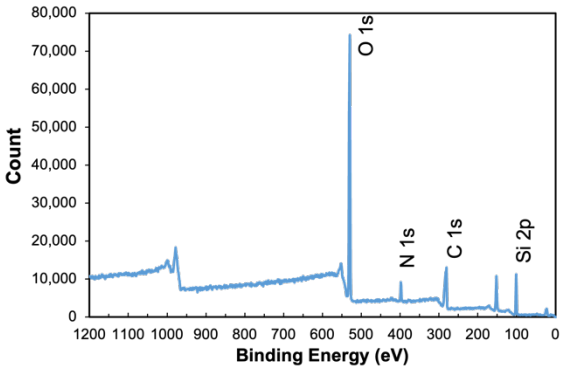

Peak ID	B.E. (eV)	Atomic %
O 1s	530	39.9
C 1s	281	39.4
Si 2p	101	15.9
N 1s	398	4.9

Figure 2.11 XPS analysis of mineralization products obtained by incubating 75 μM of V54-Car9 with 100 mM of silicic acid in water at 45°C for 8h. Two different spots were sampled to yield a mean elemental composition of 41.3% oxygen, 15.6% silicon, 38.2% carbon, and 5.1% nitrogen.

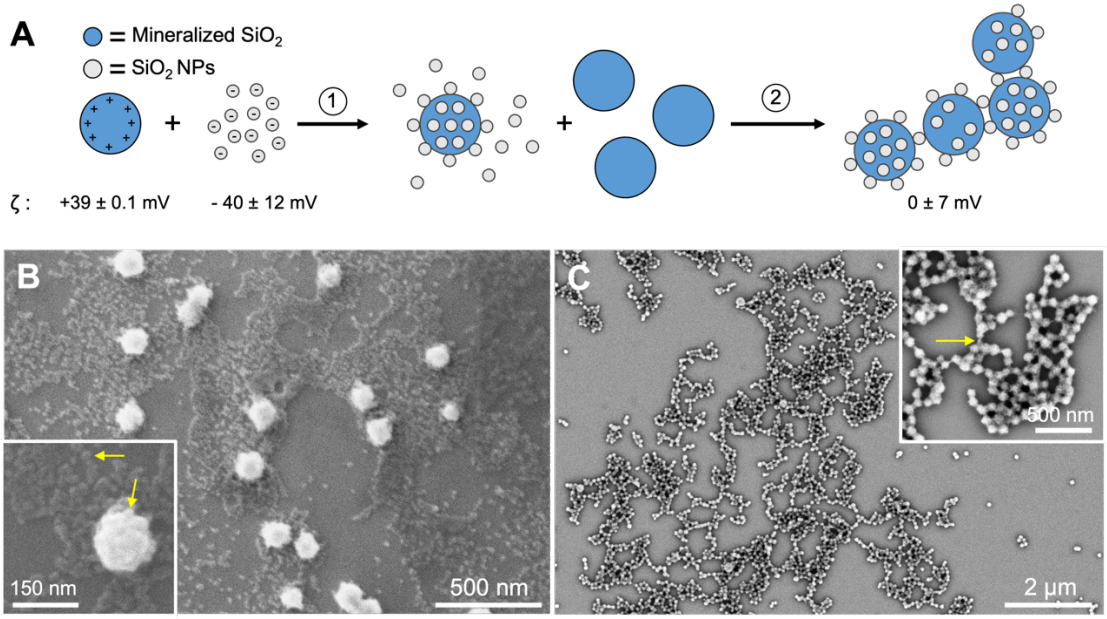

Figure 2.12 (A) Schematic of the electrostatically driven co-assembly of positively charged mineralized silica NPs (blue) with an excess of 10-nm negatively charged silica NPs (gray). (B) Products of assembly step (***1***). (C) Products of assembly step (***2***).

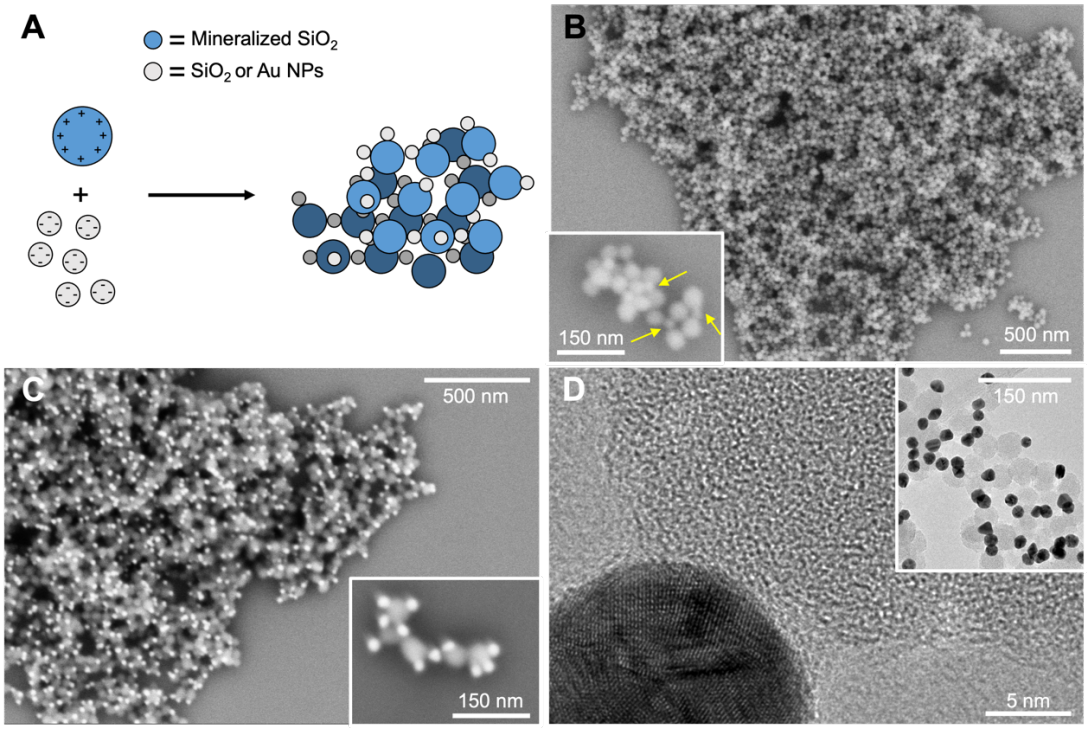

Figure 2.13 (A) Schematic of electrostatically driven co-assembly of positively charged mineralized silica NPs (blue) and 20-nm negatively charged NPs (gray). SEM images and magnified insets of the co-assembly of mineralized NPs with 20-nm silica NP (B) or 20-nm AuNPs (C). (D) HRTEM of the silica-Au interface with field of view inset.

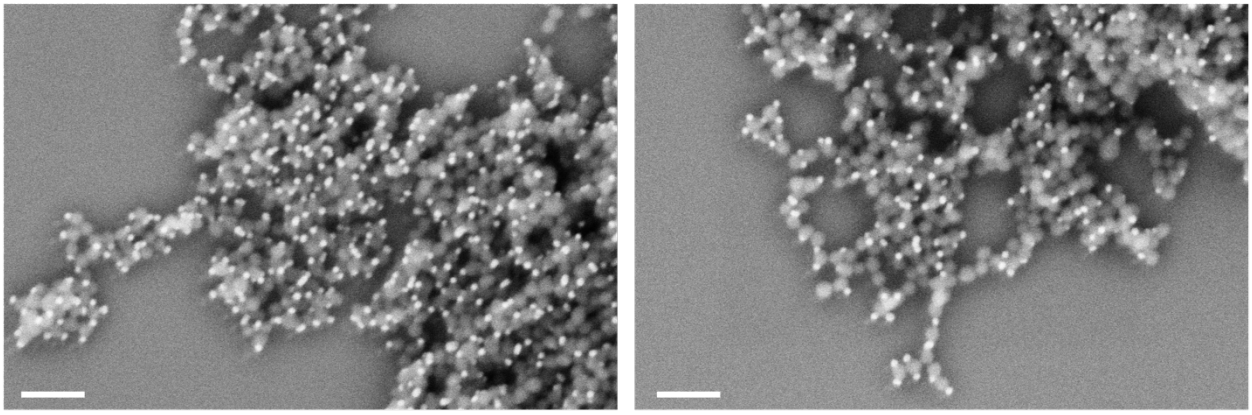

Figure 2.14 SEM images of mineralized silica/Au co-assemblies after 6 months of storage. Scale bars are 200 nm.

Chapter 3 Genetic engineering of silica-binding ELPs to study temperature-induced micellization and mineralization kinetics

3.1 Introduction

In this chapter, we seek to understand how the Car9 extension promotes temperature-triggered micelle formation and mediates the mineralization of uniform and positively charged silica NPs when fused to the C-terminus of the V54 ELP. This study, which was conducted in collaboration with Will Wixson, uses a panel of mutants whose interactions with silica surfaces was extensively characterized through molecular dynamics (MD) simulations and experimental techniques (surface plasmon resonance and atomic force microscopy).[31] Additional mutants were constructed to probe the roles of R4 and R12 on micelle formation and their stability at higher temperatures. Overall, V54-Car9 variants revealed important design rules for temperature-induced micellization, namely Arginine-4, which plays a critical role in micelle formation. We explore the interplay between electrostatic repulsion of protein micelles and the silicification reaction kinetics at elevated temperatures that alter the silica mineralization outcomes. We gain fine control over the size of nanoparticles in the 30 to 60 nm range by changing the assembly temperature and the Car9 sequence.

Previously, we used Rosetta calculations to identify a consensus low energy conformation of the Car9 dodecapeptide in solution (**Fig. 3.1A**) and used this configuration to initiate all-atom MD simulations at the silica interface.[31] In the Rosetta energy-minimized structure, P9 and G10 form a hairpin that buries the hydrophobic F6 residue and positions the cationic side chains (R4 and R12) in a way that presents a rather uniform positive charge on the peptide's molecular surface (**Fig. 3.1**). This structure

is however highly dynamic at the silica interface where a spectrum of interactions between basic sidechains and the silanol-terminated surface mediate binding. Analysis of simulation trajectories to determine the residence time (τ) of basic side chains on the silica surface revealed that three residues (R4, K7, and K8) are in contact with silica > 98% of the time, and that the sidechains of K11 and R12 play a secondary role in binding (75% < τ < 98%). Additionally, modeling the binding kinetics of various Car9 fusion proteins (sfGFP, mCherry and glucose hexokinase) to silica revealed a cooperative adsorption mechanism that could be converted to Langmuir adsorption when basic residues were mutated to uncharged ones.[30] This behavior was later rationalized by the ability of wild type Car9 to undergo rearrangements that lead to peptide self-association at the silica interface when the protein coverage is high.[31]

Here, we use this knowledge of silica-binding behavior to develop a better understanding of how the amino acid sequence of Car9 influences temperature-induced micellization and silica mineralization when fused to the V54 ELP.

3.2 Materials and Methods

Variants of V54-Car9 were constructed by Will Wixson using site-directed mutagenesis. ITC purification and protein characterization by DLS and UV-visible spectroscopy were described in **Chapter 2**. Mineralization products were diluted 100-fold in DI water and deposited on silicon substrates before imaging on Apreo-S or Apreo-2S SEMs.

3.3 Results and Discussion

3.3.1 Influence of mutations on protein assembly

Three double mutants of the V54-Car9 fusion protein – P9AG10A, K8AK11A and R4QR12Q – were constructed and purified with the expectation that insights from previous studies could be extrapolated to understand the micellization and mineralization behaviors of silica-binding ELPs (**Fig. 3.2A**). First, based on MD simulations showing that the P9AG10A substitution in the Car9 segment promotes a mix of folded conformations,[31] we anticipated a more compact packing of C-terminal extensions in the corona of V54-P9AG10A micelles. Second, we expected drastic effects of the K8AK11A and R4QR12Q mutations on micelle formation and silica mineralization since K8AK11A has a stabilizing influence on the structure of Car9 while R4QR12Q has a destabilizing one.[31] In addition, lysines and arginines have both been shown to be critical contributors to silica nucleation activity and biomimetic mineralization outcomes.[53,54,165,166] Finally, we constructed a V54 derivative of the Q4 variant, which converts four of Car9's five basic residues to glutamines (K7QK8QK11QR12Q). This quadruple mutant, which has very low affinity for silica,[30] was not expected to form micelles at high temperatures due to the drastic reduction in the number of positively charged residues that have been shown to play an important role in the formation of stable micelles.[167]

3.3.2 Arginine-4 is critical for V54-Car9 micelle formation

Both V54-P9AG10A and V54-K8AK11A mutants remained capable of forming micelles at temperatures above their T_t, as evidenced by the transient increase in D_h and turbidity of the protein solutions, which plateaued as the temperature continued to rise (**Fig. 3.2C** and **D**). We have previously shown that this transient regime is associated with

the formation of kinetically unstable intermediate aggregates that collapse into micelles as incubation time or temperature increases.[167] However, there were notable differences between wild type Car9 (**Fig. 3.2A**) and the mutants, including a higher T_t, a broader temperature window over which intermediate aggregates are present, and a twofold decrease in the zeta potential exhibited by the V54-K8AK11A micelles, as would be expected when two basic residues are eliminated (**Table 3.1**).

In contrast, neither V54-R4QR12Q nor V54-Q4 proteins were able to form micelles (**Fig. 3.2E** and **F**) as indicated by the temperature-dependent trends in D_h and turbidity. While V54-Q4 exhibited a rapid increase in turbidity, similar to that of the control V54 ELP (**Fig. 3.2G**), V54-R4QR12Q displayed a slower transition and reached lower turbidity values at higher temperatures (**Fig. 3.2E**). The DLS measurements of assembled structures of both proteins indicated transition into much larger coacervates at temperatures above their T_t. Additionally, the ζ potential values of the mutants are summarized in **Table 3.1**.

Table 3.1 summarizing T_t, ζ potential, and micellization of V54-Car9 mutants.

Variant	T_t (°C)	ζ Potential (mV)	Micellization?
V54-Car9	45	24 ± 3	Y
V54-P9AG10A	47	27 ± 4	Y
V54-K8AK11A	45	11 ± 2	Y
V54-R4QR12Q	47	6 ± 1	N
V54-R4Q	44	6 ± 1	N
V54-R12Q	42	9 ± 0.8	Y
V54-Q4	41	N/A	N
V54	40	N/A	N

* ζ potential was measured at 50°C after 10 min of incubation.

To delineate the effect of the two arginines on inhibiting temperature-induced micellization, we introduced single glutamine substitutions at positions 4 and 12 of the Car9 sequence. As shown in **Fig. 3.5A**, the V54-R4Q mutant recapitulated the behavior of V54-Q4 and V54, implicating R4 as a crucial residue in the formation of stable protein micelles. On the other hand, the V54-R12Q mutant behaved similarly to V54-K8AK11A except for a slightly lower T_t and a larger increase in turbidity at high temperatures (compare **Fig. 3.5D** and **Fig. 3.2D**). This likely indicates that the R12Q substitution is more destabilizing to micelle formation than the K8AK11A double mutation, especially when high temperatures trigger an increase in molecular mobility. Finally, the ζ potential of micelles formed at 50°C by V54-R12Q was comparable to that of V54-K8AK11A micelles produced under the same conditions (**Table 3.1**), suggesting an important contribution of the R4 sidechain to the positive charge of V54-Car9 micelles.

3.3.3 Silicification captures subtle details of the protein templates

We conducted standard silicification experiments using 75 μM solutions of the V54-Car9 variants listed in **Table 3.1** at both 50 and 65°C. While V54-Car9 micelles exhibited similar D_h values at both temperatures (33 ± 10 and 36 ± 6 nm at 50 and 65°C, respectively), the silica NPs mineralized at 65°C were nearly half the size of those produced at 50°C (**Fig. 3.3A**, **D** and **Table 3.2**). Consistently, V54-P9AG10A exhibited a similar trend: with micelle size at 30 ± 4 and 32 ± 2 nm at 50 and 65°C, respectively, the particles produced at 65°C were approximately 40% smaller than those produced at 50°C (**Fig. 3.3B**, **E** and **Table 3.2**). The consistency in micelle size rules out the possibility that the smaller particles produced at 65°C are simply the result of template shrinkage due to thermally induced compaction of the ELP core through further desolvation. Instead, faster

silicification kinetics and/or subtle changes in the structure of the corona are more likely to account for the mineralization of smaller particles. Of note, V54-P9AG10A micelles yielded particles that were about 18% smaller than those obtained with V54-Car9 at 50°C. Since the difference in size was highly significant (**Fig. 3.3G**), we propose that replacement of the hairpin-forming P9-G10 residues by smaller alanine side chains allows either for more compact packing of the silica-binding segments or to an alternative presentation of surface sidechains to the solution.

Table 3.2 summarizing the size distribution of silica nanoparticles mineralized in solutions of V54-Car9 variants at the indicated temperatures (*N = 100*)

Temp. (°C)	V54-Car9	V54-P9AG10A	V54-K8AK11A
50	57 ± 8 nm	47 ± 4 nm	53 ± 6 nm
65	31 ± 3 nm	29 ± 3 nm	N/A

The V54-K8AK11A mutant exhibited one of the most interesting behaviors. As mentioned above, while the substitution of two basic residues led to a lower zeta potential, it did not interfere with micelle formation at 50°C. These micelles templated the formation of silica nanoparticles that, at 53 nm, were intermediate in size between those produced by the Car9 and P9AG10A variant (**Fig. 3.3 C**). This would suggest that neither K8, nor K11, are crucial for micelle formation or templating silica nucleation. However, and as suggested by the evolution of D_h and turbidity (**Fig. 3.2 D**), incubation at higher temperatures magnified the deleterious impact of the lysine substitutions. No uniform micelles were observed, and the silicification products consisted of interconnected particles approximately 40 nm in diameter that often merged into one another to produce elongated features spanning the characteristic length of multiple particles (**Fig. 3.3 F**).

Such mineralization products are typically observed when monomeric silica-binding peptides, polyamines, or other biomolecules[53,54,166] are used to initiate silica precipitation from silicic acid precursors. This suggests that the formation of monodisperse silica nanoparticles requires an oligomeric or micellar template that carries sufficient positive surface charge to electrostatically prevent the formation of silane interconnects between vicinal particles.

As noted above, introduction of the R4QR12Q substitutions abolished micellization. Unsurprisingly, mineralization products were highly heterogeneous at either temperature (**Fig. 3.4A** and **C**). There were however differences: at 50°C, large particles in the 150-400 nm range coexisted with interconnected small particles (sub-100 nm) that often evolved into tubular features, whereas large (micron-range) and intermediate (200 nm) size particles dominated at 65°C. On the other hand, V54-R12Q produced networks of interconnected particles both temperatures (**Fig 3.5E** and **F**). Primary particles were about 35 nm in diameter and tended to merge into tubular structures at 65°C. These morphologies were very similar to those observed with the destabilized V54-K8AK11A variant at 65°C.

In contrast, addition of the V54-Q4 variant to silicic acid solutions at 50 and 65°C only resulted in uncontrolled silica precipitation (**Fig. 3.4B** and **D**) with products similar to those observed in solutions of the control V54 ELP (**Fig. 2.8A**).

Taken together, our results suggest that, whereas V54-Car9 and V54-P9AG10A readily transition from intermediate aggregates to uniform micelles above their T_t, V54-R4QR12Q remain frustrated and continue to sample a variety of aggregated conformations that range from micelles to coacervates. These heterogeneous protein

structures template the formation of equally heterogeneous silicification products, with a bias towards larger structures as the temperature increases.

3.4 Conclusion

We constructed a panel of V54-Car9 variants to study how sequence, structure, and charge influence temperature-responsive micellization and templated mineralization of silica. We draw inspiration from previous studies to substitute amino acid residues that are proposed to play kay roles in binding to silica surfaces and stabilizing the structure the Car9 peptide. We gain fundamental understanding of the interplay between electrostatic repulsion of protein micelles and the silicification reaction kinetics as a function of sequence and temperature. First, we establish that arginine-4 is a crucial residue in the formation of stable protein micelles that support the production of size-controlled and monodisperse silica. We show that, contrary to expectation, neither lysine residues in the Car9 segment is essential for micelle formation or templating silica NP precipitation. We use silica mineralization to capture intricate and subtle differences in the size of multiple protein templates at different temperatures that were otherwise indistinguishable using DLS and turbidity characterization. Further, we capture the destabilization of micelles, perhaps triggered by increased molecular mobility at higher temperatures or weakened repulsive forces in some variants that eliminated cationic residues. The destabilized templates produced silica networks comprising of interconnected particles that often merged into one another to produce elongated features and heterogenous morphologies.

To summarize, we established that, unlike conventional silica synthesis routes, our biomimetic system exploits assembly temperature, as well as peptide sequence, to gain

precise control over the silica nanoparticle size and monodispersity produced in short reaction times under mild conditions. We anticipate that conducting mineralization reactions at intermediate temperatures using this panel of protein variants could achieve finer control over the NP size and enable precision synthesis of silica nanomaterials. These varying products could be used for a proof-of-concept experiment aimed at the capture and release of molecular cargo mediated by the hydrophobic interactions between ELP chains. This system can also be expanded to mixtures of silica-binding ELPs with untagged ELPs to access composite LCST regimes that could template unique mineralization outcomes.

3.5 Figures

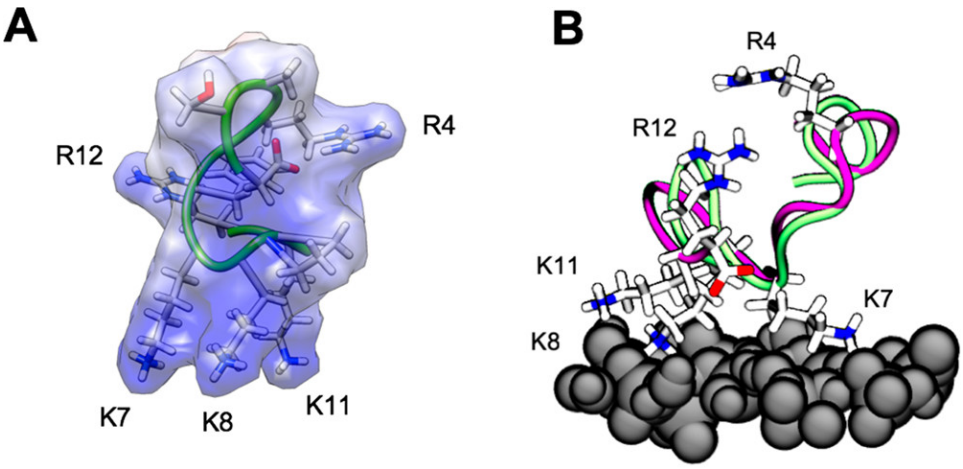

Figure 3.1 Low energy structure of Car9 in solution (A) and at the silica interface (B). The solution structure was proposed by Rosetta. (B) Superimposition of the structure proposed by Rosetta (green) and MD simulations (pink). Adapted from Ref. [31]

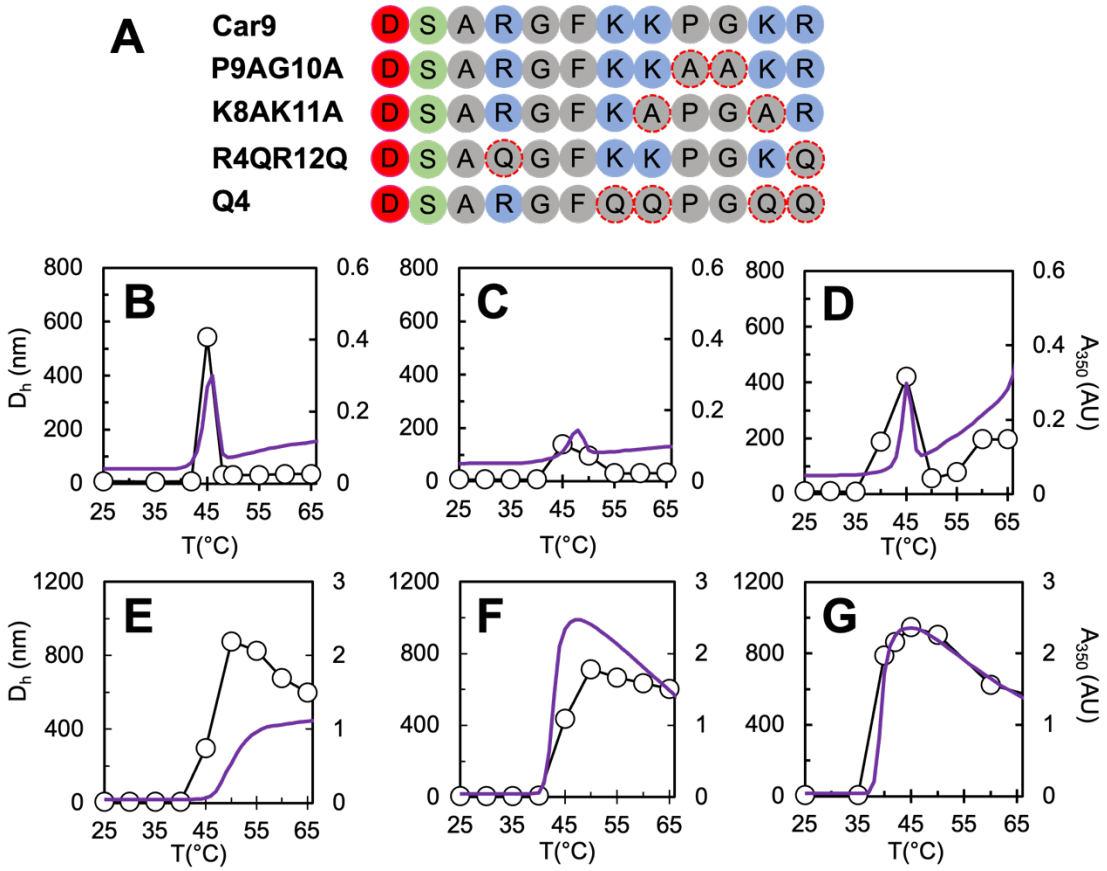

Figure 3.2 (A) Amino acid sequences of the Car9 variants. Positively and negatively charged residues are colored in solid blue and red, respectively. Substitutions are highlighted with red circles. Temperature-dependent evolution of the D_h (left axis, black traces) and turbidity (right axis, purple traces) of 75 μM solutions of V54-Car9 (B), V54-P9AG10A (C), V54-K8AK11A (D), V54-R4QR12Q (E), V54-Q4 (F), and V54 (G).

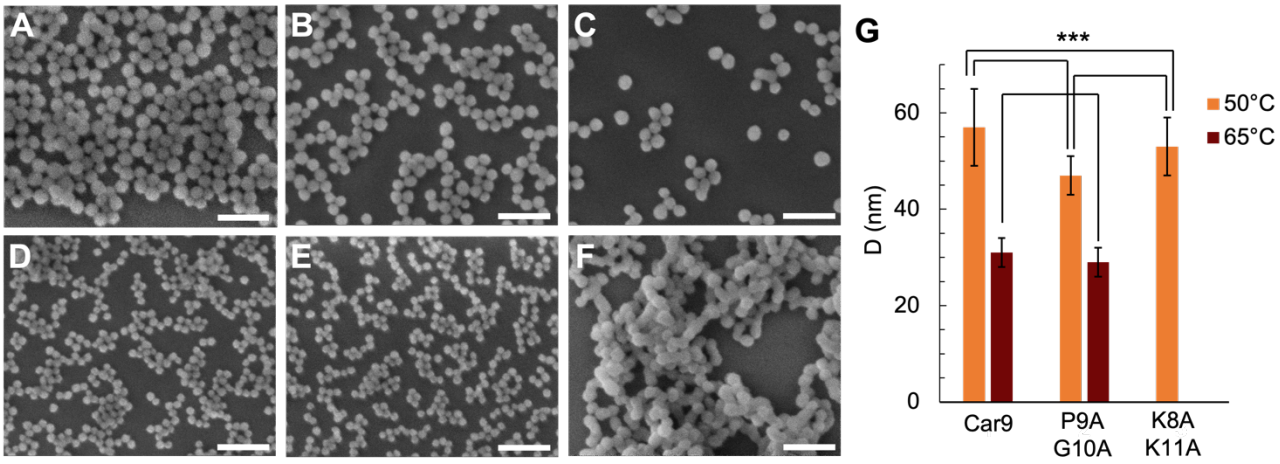

Figure 3.3 Representative SEM micrographs of mineralization products obtained with 75 μM solutions of V54-Car9 (A and D), V54-P9AG10A (B and E), or V54-K8AK11A (C and F). Reactions were conducted at 50°C (A-C) or 65°C (D-F) for two hours. Scale bars are 200 nm. (G) Mean diameters and standard deviations of silica nanoparticles mineralized at the indicated temperatures (N = 100).

*** p values are $< 10^{-6}$.

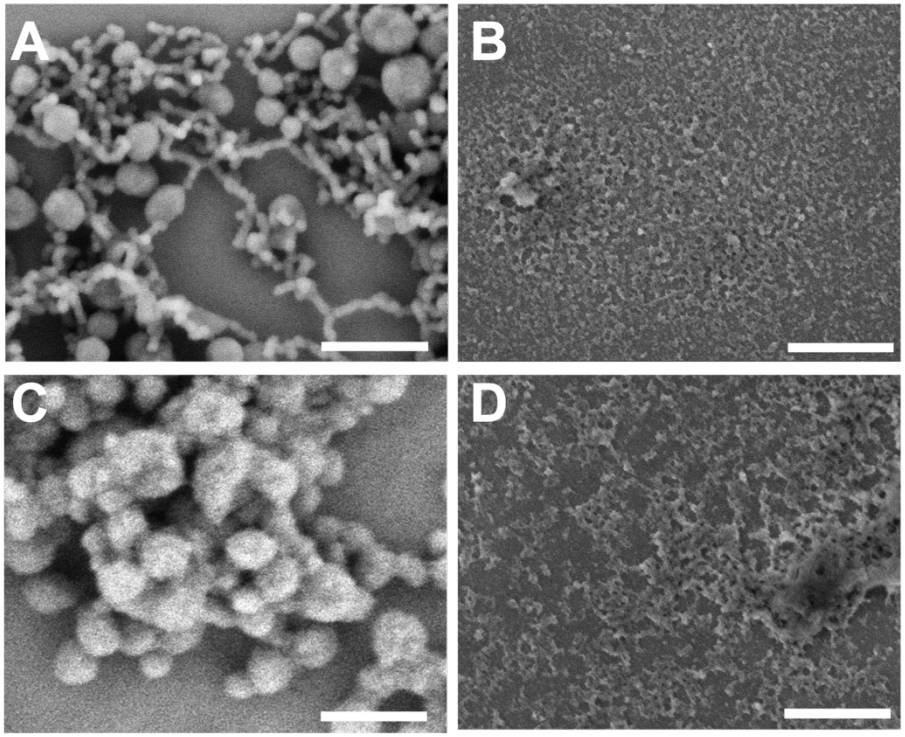

Figure 3.4 SEM micrographs of the mineralization products with 75 μM solutions of V54-R4QR12Q (A and C) or V54-Q4 (B and D) at 50°C (A and B) and 65°C (C and D). Scale bars are 500 nm.

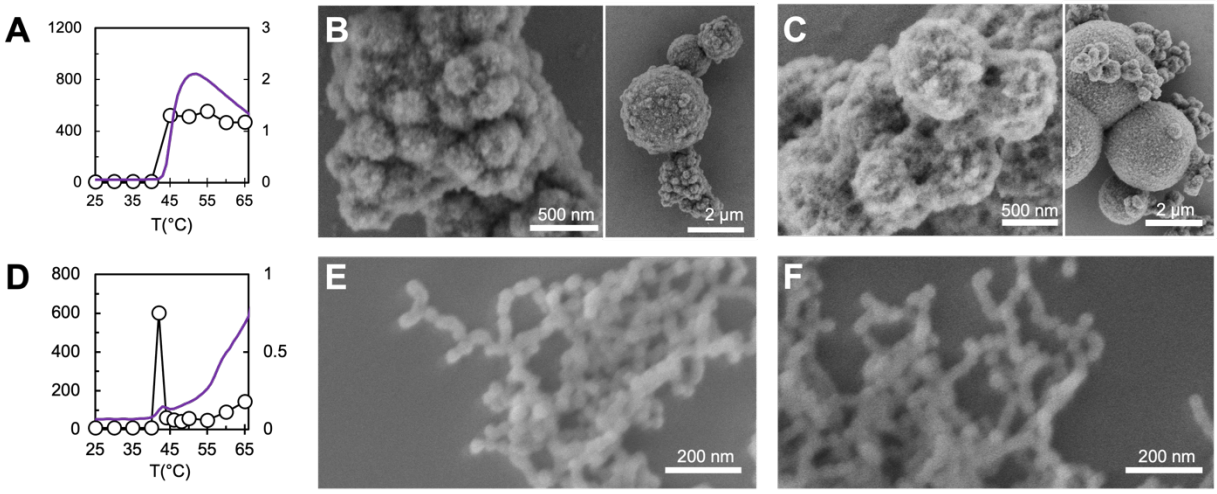

Figure 3.5 Temperature-dependent evolution of the D_h (left axis, black traces) and turbidity (right axis, purple traces) of 75 µM protein solutions of V54-R4Q (A) and V54-R12Q (D). SEM micrographs of silica mineralization products at 50°C (B, E) or 65°C (C, F) of V54-R4Q and V54-R12Q, respectively.

Chapter 4 Templated mineralization and actuation of gold nanoparticles using solid-binding elastin-like polypeptides

4.1 Introduction

As discussed in **Chapter 1**, stimuli-responsive hybrid nanomaterials hold a lot of potential for applications such as biosensing, tissue engineering, and drug delivery. In this chapter, we design a platform for the one-step synthesis and reversible actuation of gold nanoparticles (AuNPs) triggered by temperature change. We construct gold-binding ELPs to combine the mineralization properties of gold-binding peptides[67,68] with the thermoresponsive phase separation behavior of ELPs. These constructs template the synthesis of 10-nm Au nanospheres decorated with ELP brushes that mediate their assembly into 100-nm clusters at high temperatures. The cluster formation is accompanied by a 20-nm redshift in the localized surface plasmon resonance (LSPR) peak due to the plasmonic coupling of AuNPs that become vicinal. We study the influence of Au-binding sequence and solution conditions on the synthesis outcomes and dynamic assembly trends when the temperature is cycled between 25 and 45°C. In addition, we employ high-throughput experimentation capabilities to explore large synthesis spaces and tune the size of AuNPs by controlling the reaction conditions.

4.2 Materials and Methods

DNA manipulations, ITC purification, and protein characterization were described in **Chapter 2**. Construction of the plasmids encoding V54-AuBP1 and V54-AuBP2 and DLS characterization of the purified protein solutions were conducted by Yifeng Cai.

4.2.1 Au mineralization

Gold mineralization experiments were conducted as described by Ma *et al.* [59] Briefly, a precursor solution of gold ions was prepared by adding 100 µL of a freshly prepared 100 mM $HAuCl_4$ trihydrate aqueous stock to 100 µL of 1 M triethylammonium acetate and vortexing the mixture for approximately 1 min until the solution became transparent. Aliquots (8 µL) were added to 1 mL of 100 µM V54-A3 in 100 mM HEPES, pH 7.3 in a glass vial. Upon visual observation of dark objects in solution, the mixture was vortexed for 15 s, placed on a bench, and left undisturbed overnight until further spectroscopic and microscopic characterization.

4.2.2 AuNP characterization and actuation

The UV-Visible spectra of gold nanoparticles at room temperature were acquired on a BioTek Synergy LX Microplate Reader (Agilent Technologies). High throughput synthesis was conducted in collaboration with Huat Thart Chiang (Pozzo Lab) using the OT-2 liquid-handling robot (Opentrons). UV-visible characterization of assembly kinetics was done on a VANTAstar microplate reader (BMG Labtech). For thermocycling experiments, 96-well plates containing synthesis products were incubated at 45°C (hot) or 25°C (cold) for 10 min using a Peltier temperature controller. TEM and SEM characterization was described previously (**Chapter 2**).

4.3 Results and Discussion

4.3.1 Characterization of solid-binding ELP constructs

In a similar design to the ones discussed previously (**Chapters 2** and **3**), we fused the Au-binding sequence A3 (AYSSGAPPMPPF)[67,68] to the C-terminus of V54 via a flexible

linker (KLGGGS). The resulting protein, V54-A3, was purified by ITC and its LCST behavior was characterized by spectroscopy and DLS in comparison to V54, a control protein lacking a solid-binding extension.[103,121]In subsequent work, two additional Au-binding peptides were chosen as cationic candidates for ELP-fusion via the KLGGGS linker to construct V54-AuBP1 and V54-AuBP2[70] (sequences are shown in **Fig. 4.1A**). Protein solutions exhibited a rapid increase in the optical density at 350 nm that correlated with a transition from extended unimers with a mean D_h of 8 nm, to desolvated coacervates approximately 800-1000 nm in size (**Fig. 4.1B** and **C**). The temperatures at which these transitions occurred (T_t) were comparable for all Au-binding ELP constructs with about 2-5°C variation.

4.3.2 Gold mineralization and temperature-triggered actuation using V54-A3

V54-A3 was used to synthesize AuNPs from a $HAuCl_4$ precursor in the presence of TEAA and HEPES as described previously.[59] SEM and TEM imaging of the mineralization products obtained after overnight incubation at room temperature revealed the presence of monodisperse Au nanospheres with an average diameter of 10 ± 2 nm under dry conditions (**Fig. 4.3A-D**), and the expected LSPR maximum at 530 nm.[66] The mean D_h of the particles obtained by DLS was 9 ± 1 nm (**Fig. 4.3E**), suggesting that the protein unimers either become incorporated in the growing Au structures, or that they form capping shells around AuNPs without significantly extending into solution. Two lines of evidence support the second hypothesis. First, the AuNPs produced are monodisperse, suggesting that the A3 segment of the V54-A3 protein efficiently caps their growth. Second, lattice fringes with a *d*-spacing that could be assigned to the (111) facet of Au were visible in HRTEM images (**Fig. 4.3C)**, suggesting that the mineralized particles are

crystalline. To confirm that the ELP segments of the V54-A3 proteins are solvent-accessible and functional, we repeatedly transitioned the mineralized particles between 25°C and 45°C. **Fig. 4.5** shows that heating was accompanied by a 20-nm redshift consistent with the plasmonic coupling of AuNPs that become vicinal due to ELP-driven coacervation. SEM images (**Fig. 4.4**) confirmed the formation of clusters averaging 97 ± 29 nm (n = 40) under dry conditions when the temperature was raised above T_t for ten min. The process was highly reversible as indicated by UV-visible measurements (**Fig. 4.5C**). In short, V54-A3 combines the salient characteristic of its SBP and ELP components by both supporting the mineralization of ~10 nm AuNPs under mild conditions and mediating their reversible thermally driven aggregation into ~100 nm clusters.

4.3.3 Modular design of Au-binding ELPs and high throughput AuNP synthesis

As mentioned above, two additional Au-binding peptide candidates were selected as fusion partners for the ELP to template AuNP synthesis and access different size regimes by varying the peptide sequence and concentration. Although both AuBP1 (WAGAKRLVLRRE) and AuBP2 (WALRRSIRRQSY) possessed a net positive charge comparable to Car9's cationic character, they did not assemble into micelles at temperatures higher than their T_t. Much like the control V54, they form large 800-nm coacervates with high turbidity.

We expanded our knowledge of AuNP synthesis and reversible temperature-triggered actuation of clusters templated by gold-binding ELPs to explore large synthesis spaces using each of the three constructs: V54-AuBP1, V54-AuBP2, and V54-A3. We employed a liquid-handling robot to test out the influence of varying the protein concentration in

identical reducing buffer and gold precursor conditions on the NP synthesis outcomes as characterized by LSPR peak and dynamic assembly/disassembly in response to temperature increase/decrease. **Fig. 4.5** shows representative micrographs of AuNPs mineralization in solutions of V54-AuBP1 and V54-AuBP2 in HEPES buffer.

4.3.4 Next steps

We established a modular ELP-SBP fusion design that enabled the synthesis of AuNPs and their thermal triggered reconfiguration into 100-nm clusters. These clusters exhibited a 20-nm LSPR peak shift corresponding to the plasmonic coupling of AuNPs that became vicinal due to ELP-mediated coacervation at high temperatures. Not only did these clusters resolve into individual particles after incubation at room temperature for 10 min, but also the reversible assembly and disassembly and their associated LSPR signals were retained for multiple cycles of heating and cooling. If the system was illuminated with a 530-nm laser, optical energy deposition could be sufficient to trigger the coacervation of ELPs and clustering of AuNPs eliminating the need for an external thermal stimulus. Many studies revealed that light absorption by AuNPs can lead to a plasmon-assisted increase in their thermal energy[168,169] which can be exploited in our Au-ELP system to create a primitive feedback loop: (1) AuNPs absorb light at 530 nm leading to optical heating; (2) Local increase in thermal energy leads to coacervation of ELPs and formation of AuNP clusters exhibiting a 20-nm LSPR shift due to plasmonic coupling; (3) Clusters will no longer absorb the 530-nm light efficiently leading to decrease in optical heating; (4) Decrease in temperature leads to the cluster disassembly into individual particles exhibiting 530-nm LSPR peak and reverting to the first step.

4.4 Conclusions

This work demonstrates a modular design that combines the biomimetic mineralization properties of SBPs with the thermoresponsive phase separation behavior of ELPs to synthesize thermoresponsive inorganic nanoparticles. We constructed a 54-repeat ELP genetically fused to a gold-binding dodecapeptide to promote the nucleation of AuNPs in a precursor solution of gold chloride and reducing buffer conditions. We demonstrated that the Au-binding segment capped the growth of AuNPs, while the V54 segment remained functional for coacervation. This finding was in agreement with previous reports that Au-binding peptides mediate the nucleation of AuNPs and cap their growth to produce well-defined nanoparticles.[68,70] The resulting AuNPs could be reversibly assembled into 100 nm clusters by temperature upshift and deconstructed into individual particles by cooling. In hybrid systems, it is desirable to gain precise control over the size and shape of inorganic nanoparticles, but also to tune the spatial arrangement and stimuli responsive actuation of such building blocks. Our approach provides a platform to synthesize stimuli responsive functional nanomaterials that possess unique optical and catalytic properties with applications in energy storage and conversion, drug delivery, cancer therapy, and others.

4.5 Figures

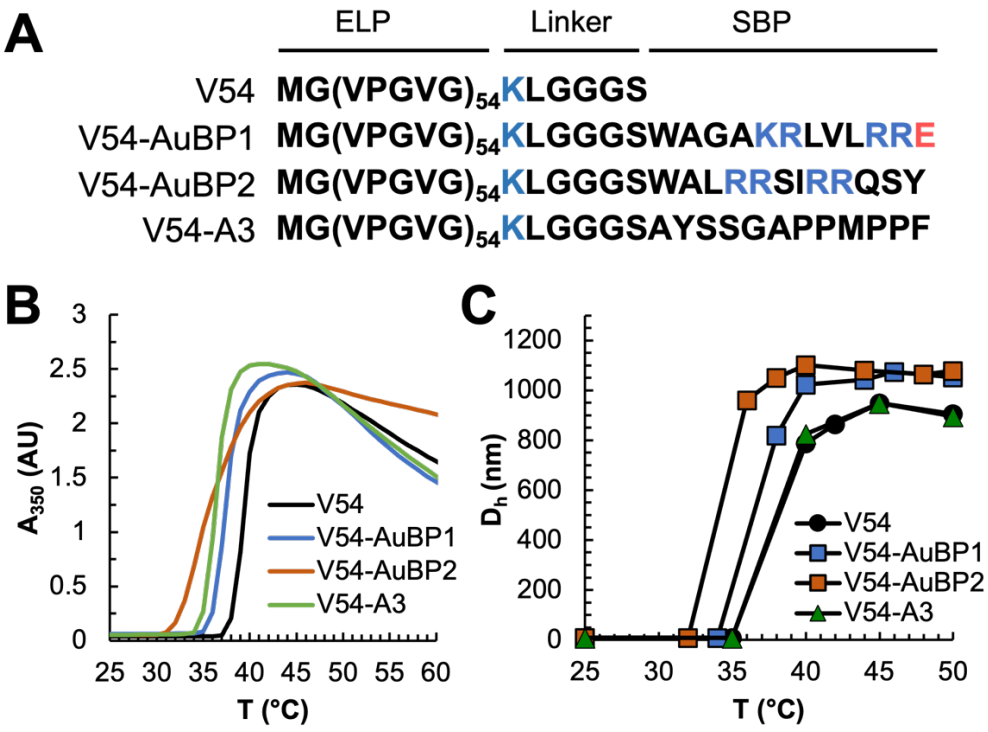

Figure 4.1 (A) Amino acid sequences of the V54 control ELP and Au-binding ELPs: V54-AuBP1, V54-AuBP2, and V54-A3. Positively and negatively charged residues are colored in blue and red, respectively. Temperature-dependent evolution of the turbidity (A) and D_h (B) of 75 µM solutions of proteins.

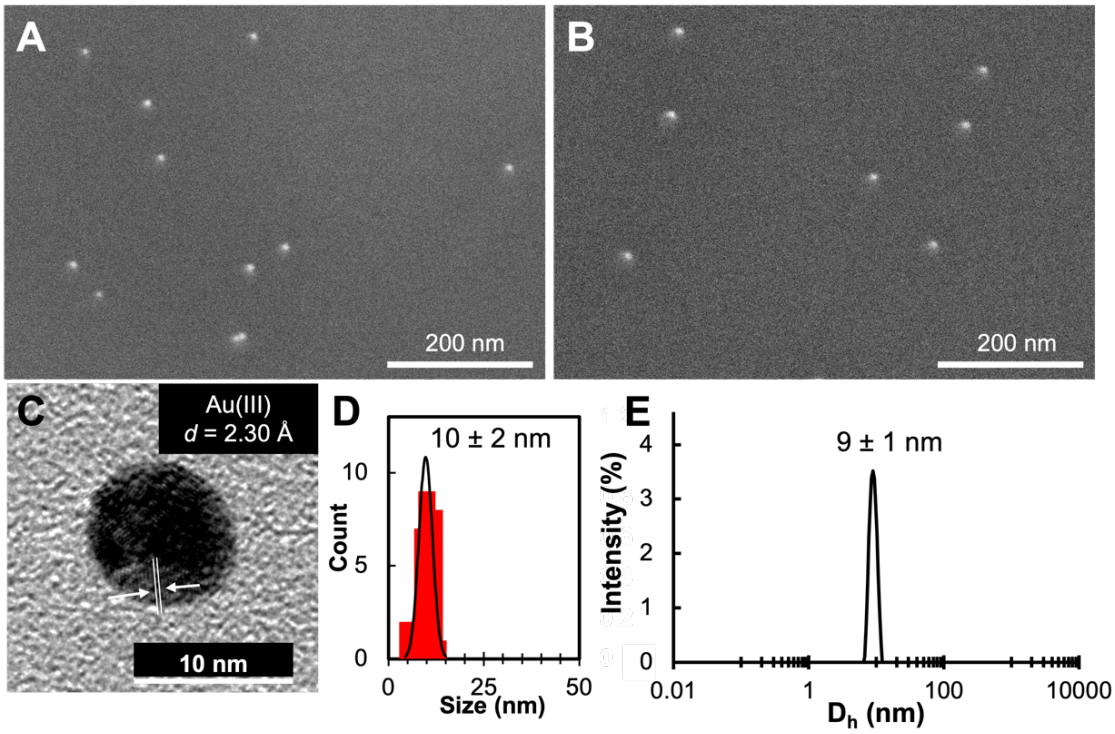

Figure 4.2 SEM (A, B) and TEM (C) images, corresponding particle size distribution (D), and DLS intensity profile (E) of AuNPs mineralized with 100 μM of V54-A3 at 25°C.

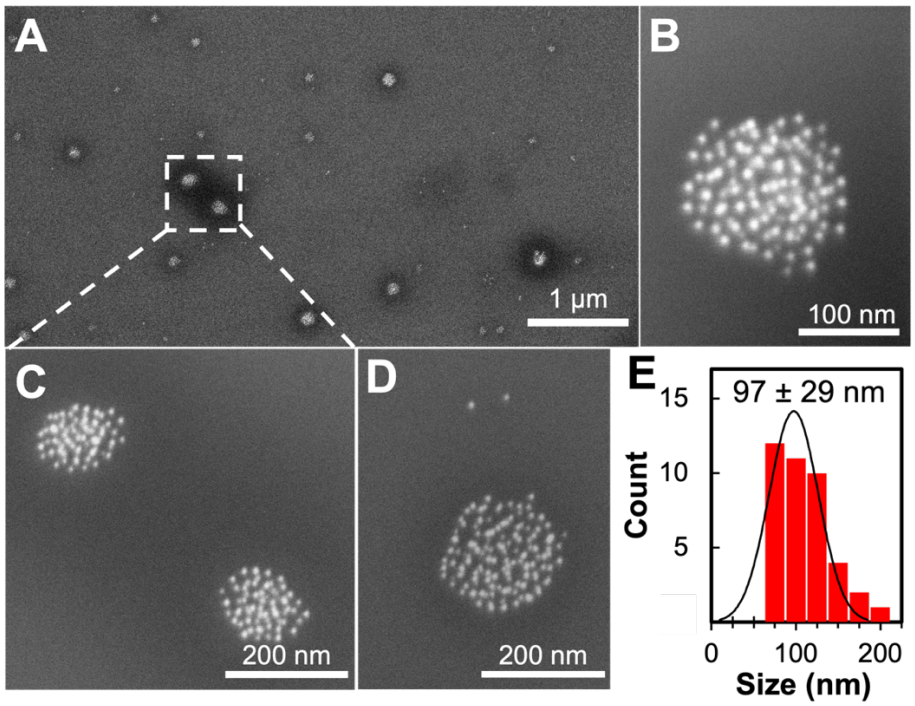

Figure 4.3 Field of view (A) and magnified (B-D) SEM images of AuNP clusters formed after incubation at 45°C for 5 min and the corresponding cluster size distribution (E).

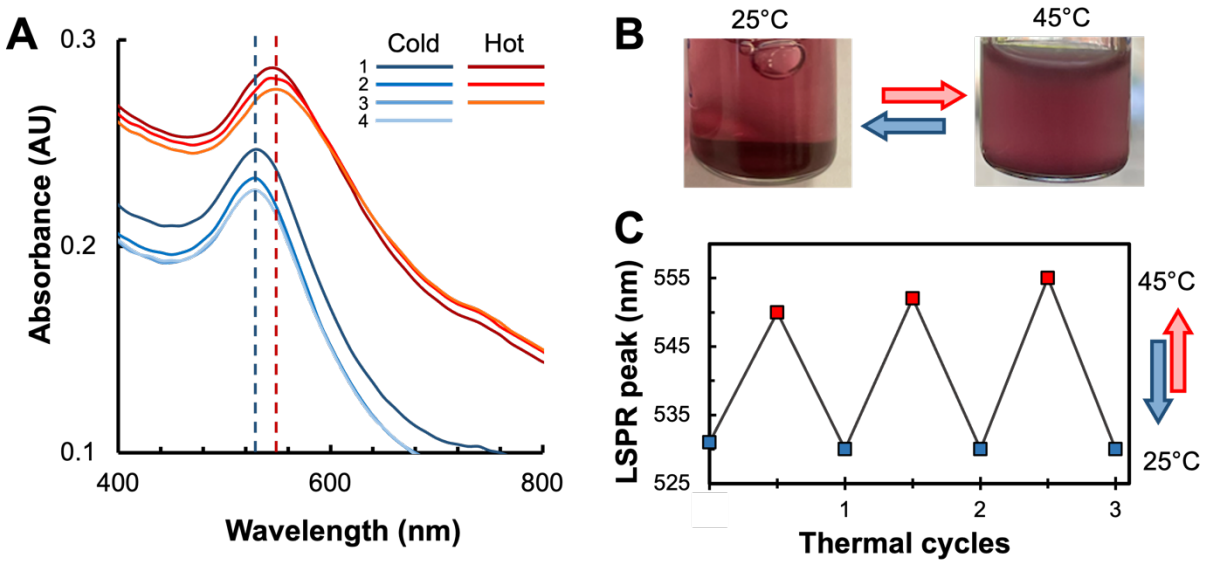

Figure 4.4 UV-Visible spectra (A), observed turbidity (B), and LSPR shift (C) associated with repeated cycles of heating AuNPs to 45°C and cooling to 25°C with 10 minutes equilibration steps at each temperature.

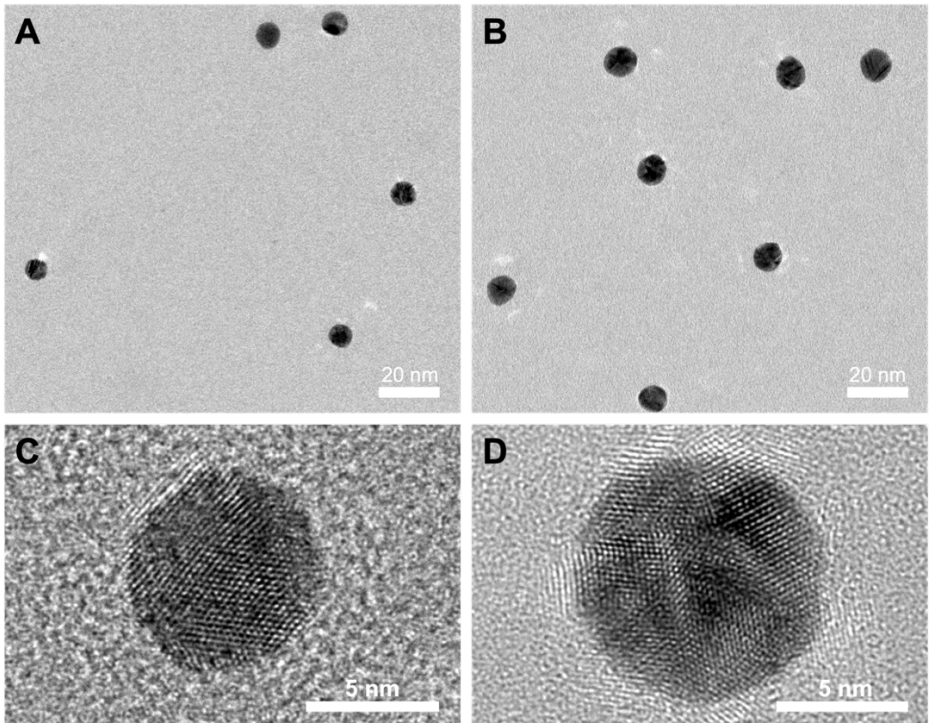

Figure 4.5 Field of view (A-B) and magnified (C-D) TEM images of AuNPs synthesized in solutions of V54-AuBP1 (A and C) or V54-AuBP2 (B and D).

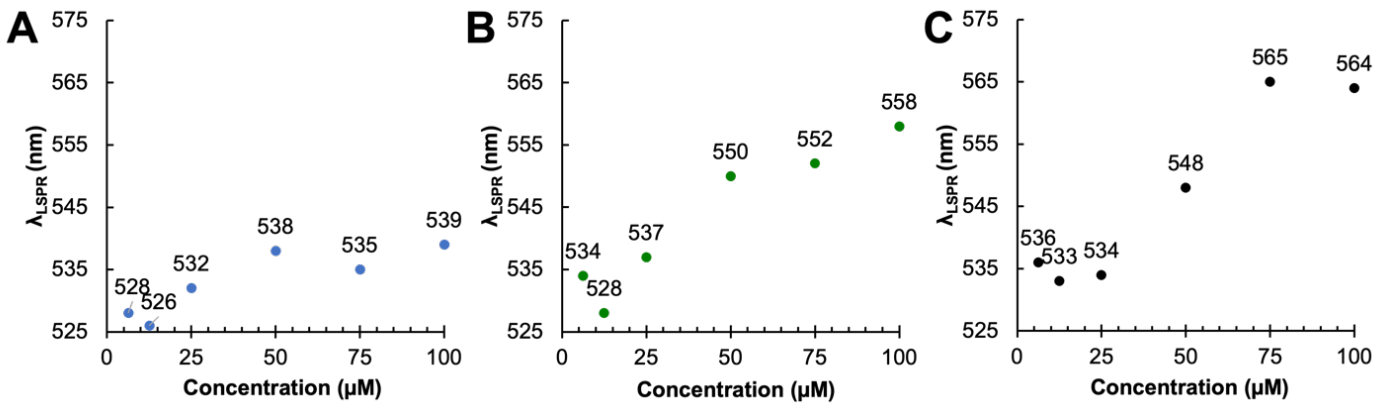

Figure 4.6 LSPR peaks of AuNPs synthesized in solutions of V54-AuBP1 (A), V54-AuBP2 (B), or V54-A3 (C) at varying concentrations as indicated.

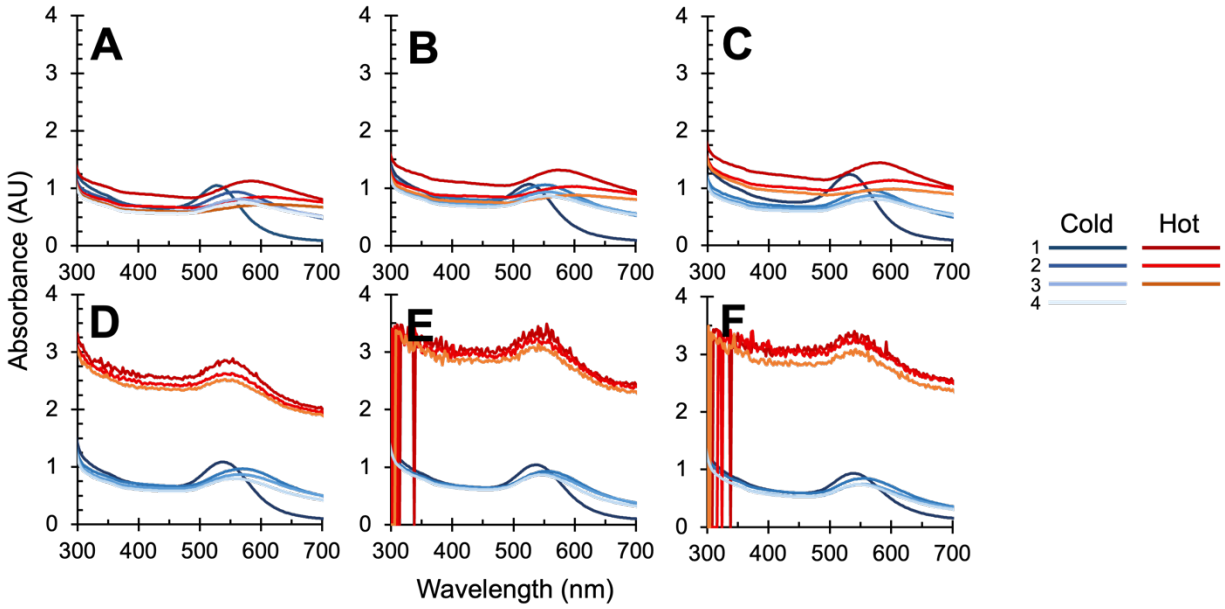

Figure 4.7 UV-visible spectra of the AuNPs synthesized in 6.25 (A), 12.5 (B), 25 (C), 50 (D), 75 (E), or 100 μM (F) solutions of V54-AuBP1 in HEPES buffer supplemented with $HAuCl_4$. Samples were thermocycled by incubating the 96-well plate at 45°C (hot) or 25°C (cold) for 10 min.

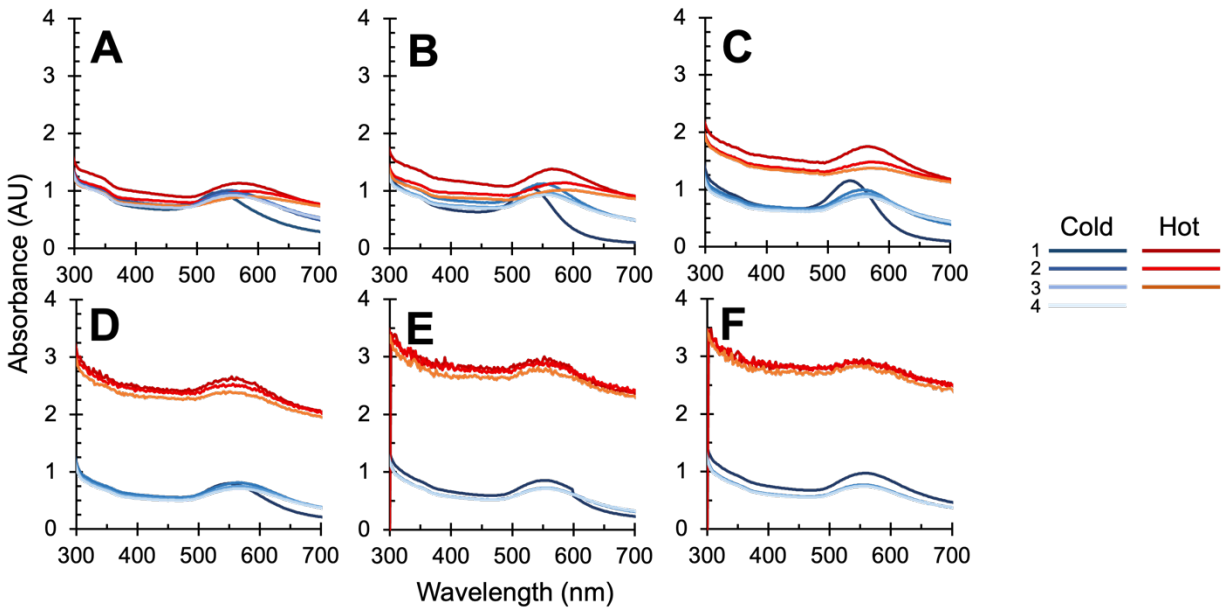

Figure 4.8 UV-visible spectra of the AuNPs synthesized in 6.25 (A), 12.5 (B), 25 (C), 50 (D), 75 (E), or 100 μM (F) V54-AuBP2 solutions of in HEPES buffer supplemented with $HAuCl_4$. Samples were thermocycled by incubating the 96-well plate at 45°C (hot) or 25°C (cold) for 10 min.

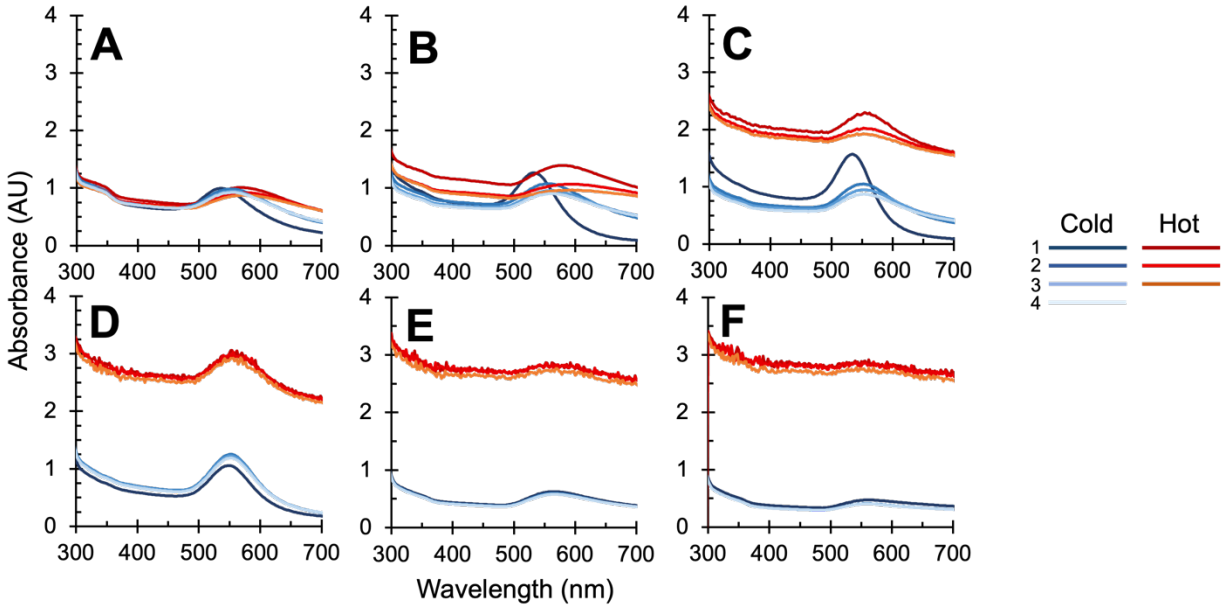

Figure 4.9 UV-visible spectra of the AuNPs synthesized in 6.25 (A), 12.5 (B), 25 (C), 50 (D), 75 (E), or 100 μM (F) solutions of V54-A3 in HEPES buffer supplemented with $HAuCl_4$. Samples were thermocycled by incubating the 96-well plate at 45°C (hot) or 25°C (cold) for 10 min.

Chapter 5 Bio-inspired silica mineralization using R5 peptoids

5.1 Introduction

As previously discussed, silica-based nanomaterials have been widely studied for their vast range of applications. Many biomimetic approaches towards tailored nanoscale silica synthesis use organic molecules (proteins, peptides, polypeptides, or synthetic polymers) to precipitate silica from a precursor solution and control mineralization outcomes. Peptides and proteins are especially desirable synthesis building blocks thanks to their chemical monodispersity, programmability, and structural complexity. As discussed in **Chapter 1**, a large number of studies have used silaffin-derived peptides - and most often the R5 peptide - to achieve control over the organization, size, and structure of mineralized silica nanoparticles. Peptoids are synthetic polymers consisting of building blocks that are analogous to natural amino acids except that side chains are attached to backbone nitrogen atoms instead of α-carbons (**Fig. 5.1A**).[170] This leads to increased resistance to proteolysis, higher thermostability, conformational flexibility, and ease of synthesis compared to peptides and proteins. Importantly, peptoids have been successfully programmed for self-assembly and used to gain control over the crystallization of inorganic materials.[59,171–174] In this chapter, we discuss a study that centers Molecular Dynamics (MD) simulations to investigate how sequence and backbone structure impact the outcomes of silicification using the R5 peptide or a peptoid mimic of this peptide.

5.2 Materials and Methods

5.2.1 Synthesis of R5 peptide and peptoid analogs

R5 forward (Acetyl-SSKKSGSYSGSKGSKRRIL-Amide) and R5 reverse (Acetyl-LIRRKSGKSGSYSGSKKSS-Amide) peptides were synthesized using GenScript's PepPower platform.

Peptoid analogs were synthesized by the Chen Lab (PNNL) as follows: rink amide resin (0.09 mmol) was used to generate C-terminal amide peptoid R5. First, the Fmoc groups on the resin were removed in 2 mL of 20% (v/v) 4-methylpiperidine/N,N-dimethylformamide (DMF) by agitating for 40 min, filtering, and washing with DMF five times. For each DMF wash, 1 mL of DMF was added and the solution was agitated for 1 min. An acylation reaction was next performed on the amino resin by adding 1.5 mL of bromoacetic acid in DMF (0.6 M), followed by addition of 0.30 mL of 50% (v/v) N,N-diisopropylcarbodiimide (DIC)/DMF. The mixture was agitated for 10 minutes at room temperature, filtered and washed 5 times with DMF. Nucleophilic displacement of the bromine with different primary amines was conducted by addition of 1.5 mL of primary amine monomer (0.6 M) in N-methyl-2-pyrrolidone (NMP), followed by agitation for 10 minutes at room temperature. The monomer solution was filtered from the resin and washed 5 times with DMF. Acylation and displacement steps were repeated until the entire R5 peptoid analog was synthesized. The final crude product was cleaved from the resin by addition of 2 mL of TFA/water (v/v = 95/5) and agitation for 30 minutes. The solution was collected by filtration, followed by washing the resin twice with 1 mL of 95% TFA. The solvent was next evaporated under a stream of N_2 gas, yielding an oily crude product that was dissolved in H_2O/CH_3CN (v/v = 1/1) for HPLC purification. The target

peptoids were purified by reverse-phase HPLC on a XBridge Prep C18 10 µm Optimum Bed Density (10 µm, 19 mm × 100 mm), using adaptable gradient of acetonitrile in H_2O with 0.1% TFA over 15 min. Purified peptoids were analyzed on a Waters ACQUITY reverse-phase UPLC using a gradient over 7 min at 40°C on a 1.7 µm, 2.1 mm × 50 mm ACQUITYBEH C18 column operated at 0.4 mL/min. The C18 column was connected toa Waters SQD2 mass spectrometry system. The purified R5 peptoids were lyophilized in a mixture of water and acetonitrile (v/v = 1/1). Peptoid powders were finally divided into small aliquots and stored at −80°C until further use.

5.2.2 Silica mineralization templated by R5 peptides and peptoid analogs

In the following protocol, “reagent” is used to refer to forward/reverse peptides/peptoids depending on the experiment. Solutions of orthosilicic acid were freshly prepared as previously described. Samples were prepared by resuspending the pre-weighed lyophilized reagent in phosphate-citrate buffer ([Na_2HPO_4] = 164.3 mM and [citric acid] = 7.1 mM at pH 7) to reach a final concentration ranging from 1 to 3 mM. To induce mineralization, orthosilicic acid was added to the reagent solution at a 1:10 volumetric ratio, and samples were vortexed for 10 s. The reaction was allowed to progress at room temperature for 5 minutes before vials were centrifuged for 10 minutes at 15,000*g*. The supernatant was carefully removed by aspiration, and pellets were washed three times with DI water and centrifugation for 10 minutes at 15,000 *g*. Pellets were finally taken into 100 µL of DI water. For SEM imaging, 3 µL of the solution was deposited on a silicon wafer and allowed to airdry overnight. Images were acquired on FEI Sirion XL30 SEM operated at 2 kV and a spot size of 1 using through-lens detection (TLD) and ultra-high resolution (UHR) mode.

5.2.3 Surface Plasmon Resonance (SPR)

SPR chips were fabricated in house using a glass substrate coated with a 2-nm titanium adhesion layer, a 48-nm evaporated gold film, and a 4-nm silicon film deposited by plasma-enhanced chemical vapor deposition.[30] Chips were cleaned with ethanol and DI water before use and mounted on the four-channel flow cell of a SPR sensor from the Institute of Photonics and Electronics (Prague, Czech Republic). Channels were equilibrated in phosphate-citrate buffer for 15 min as described previously.[30,31] Two of the channels were then used to run "forward" R5 peptide and "forward" R5 peptoid (called R5A) samples at 25 μM. The third was used to run pure phosphate-citrate buffer to establish a subtractable baseline. After 30 min, channels were washed with phosphate-citrate buffer until a plateau in the SPR shift was reached. All experiments were conducted at a flow rate of 40 μL-min^{-1} and at room temperature.

5.3 Results and Discussion

In this study, we postulated that a peptoid analog of the R5 peptide might offer significant improvements in silicification activity due to its alternative backbone structure and conformational flexibility. We collaborated with the Pfaendtner Lab to investigate how differences in molecular interactions, and the resultant binding energies to silica surfaces, would influence SiO_2 mineralization outcomes. Although it is possible to computationally study an exact R5 peptoid mimic, where identical side chains are attached to backbone nitrogen atoms, this design presented experimental challenges to collaborator Chen since some amino acid residues were not readily available as precursors for peptoid synthesis (including glycine which cannot typically be included in peptoid sequences). **Fig. 5.1B**

shows the peptoid analogs that were used to synthesize R5 peptoids compared to their canonical amino acid counterparts.

We used SPR to compare the binding affinity of peptide and peptoid constructs to a silica surface. To this end, equimolar concentrations of the R5 peptide and its R5 peptoid analog (**Fig. 5.2**) were flowed over a silica-coated chip until SPR shifts reached a plateau. This equilibrium shift, which is reached when the number of dissociation events equals the number of association events, approximates the macromolecular coverage on the chip surface and can be used as a proxy for binding affinity. **Fig 5.2A** shows that the SPR shift was approximately 4-fold larger for the peptoid relative to the peptide, denoting a substantially higher binding. This trend was in agreement with MD simulations (**Fig. 5.3**) predicting that the R5 peptoid analog had a substantially higher free energy of binding on silica compared to the R5 peptide or atheoretical R5 peptoid mimic possessing identical side chains. Calculations were used to study the two-dimensional free energy profiles and identify the preferred backbone structure(s) corresponding to each construct on the silica surface. Unlike R5 peptide, R5 peptoid analog was found to have only one clear mode of binding to the surface with a radius of gyration around 1.4 nm. Additionally, MD simulations identified residues Y8, K12, K15 and R16-17 as significant contributors to the higher binding energy by virtue of being significantly closer to the silica surface due to increased peptoid backbone flexibility.

We assessed the impact of these variations in binding energy on silica mineralization by mixing 1 mM or 3 mM of the R5 peptide or its peptoid analog with silicic acid. At 3 mM, both constructs yielded quasi-spherical SiO_2 particles in the 500-600 nm range (**Fig. 5.4**). However, at the lower concentration, there was a marked difference in synthesis

outcomes: while the R5 peptoid analog yielded similar 500 nm spherical particles, the peptide induced the formation of an extended structure consisting of interconnected, polycondensed nanostructures that lacked any morphological control. The peptoid's retained morphological control at lower concentrations demonstrates the stronger interactions with silica and backbone flexibility contributes to the superior silicification activity. These results support the MD calculations and SPR experimental results indicating strong silica binding affinity in the case of peptoid analogs.

5.4 Conclusion

In this collaborative work with the Pfaendtner and Chen labs, we conducted a computationally guided study to understand the structural differences between the R5 peptide and its peptoid analog and their impact on silicification products. We conducted SPR experiments to validate the differences in binding energy predicted by metadynamics calculations. MD simulations were also used to show that charged and polar residues lie in closer proximity to silica surfaces in the peptoid analog of the R5 peptide. Our results reveal that differences in binding energy could be useful in predicting biomimetic mineralization behavior in agreement with previous work.[175] In addition, we identify several key features that can aid in designing targeted mineralization templates in the future.

5.5 Figures

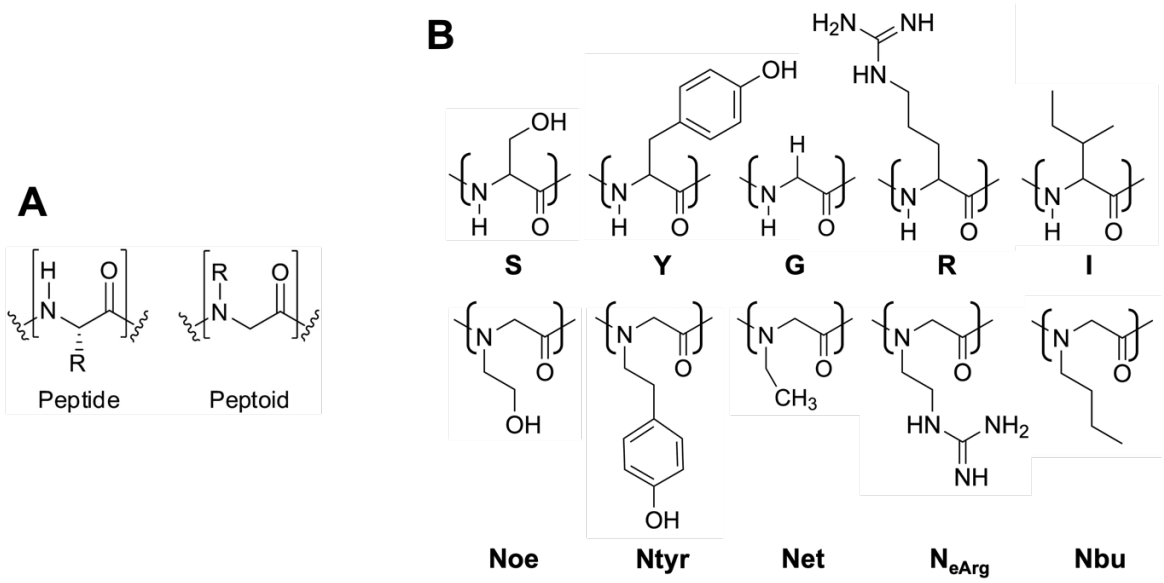

Figure 5.1 (A) Differences in backbone chemistry and side chain placement between peptides and peptoids, (B) canonical sidechain chemistry for serine, tyrosine, glycine, arginine, and isoleucine (top) compared to their synthetic peptoid analogs (bottom).

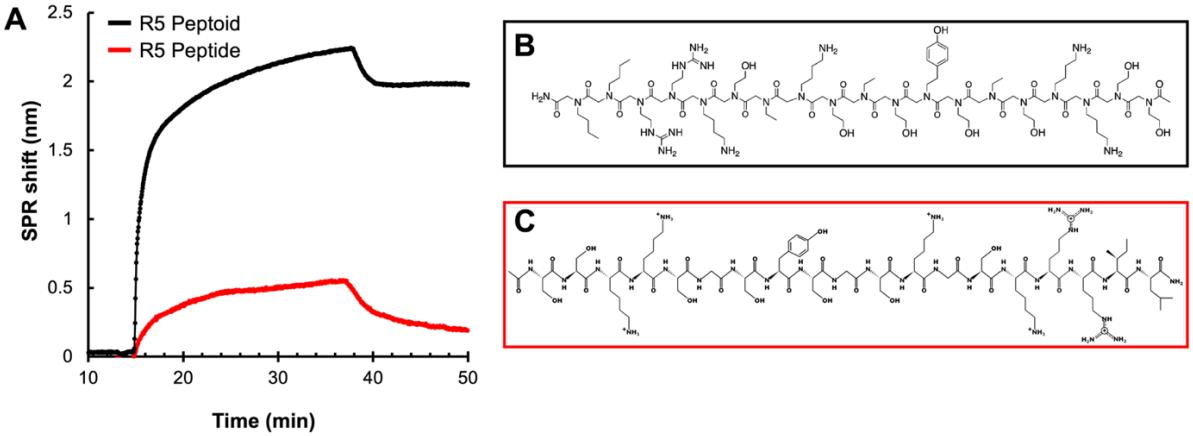

Figure 5.2 SPR sensorgrams obtained by flowing 25 μM solutions of R5 peptoid analog (black) and R5 peptide (red) on a multichannel SiO_2-coated SPR chip. Chemical structures of R5 peptoid (B) and R5 peptide (C).

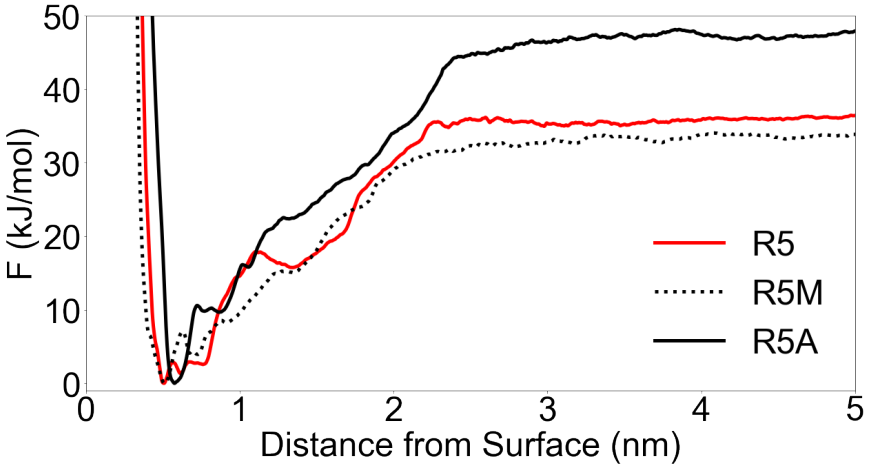

Figure 5.3 Binding free energy of the center of mass (COM) of the R5 peptide (solid red), R5 peptoid theoretical mimic (dotted black), and R5 peptoid analog (solid black) to an amorphous silica surface obtained through metadynamics calculations.

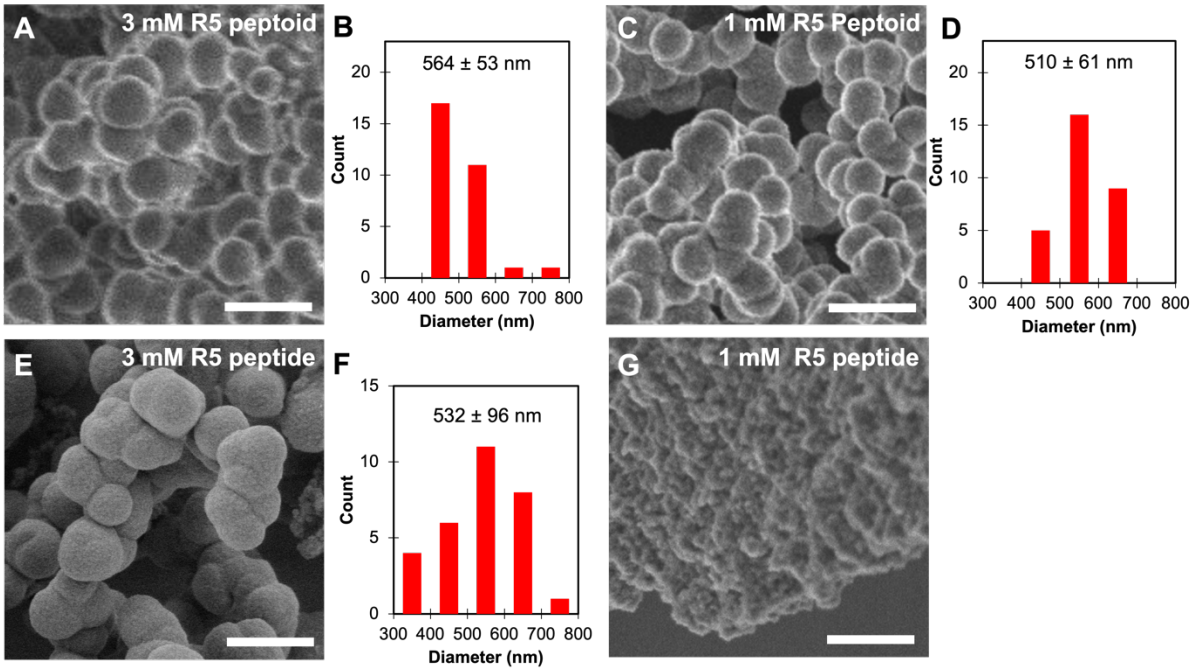

Figure 5.4 SEM images of SiO_2 mineralization products obtained in solutions of 3 mM (A) or 1 mM (C) of R5 peptoid or 3 mM (E) or 1 mM (G) of peptide R5. Histograms show the corresponding particle size distributions based on n = 30.

Chapter 6 Conclusions

In this dissertation, we present a series of detailed studies aimed at gaining a fundamental understanding of and achieving precise control over the biomimetic mineralization and dynamic reconfiguration of inorganic materials mediated by biomolecular building blocks. First, we construct silica-binding ELPs that exhibit unique self-assembly behavior above their T_t, producing uniform micelles that display a high density of the cationic silica-binding Car9 peptides on their coronae. We establish that, unlike the extended protein unimers, protein micelles template the self-limiting growth of 60-nm silica nanoparticles that exhibited a high degree monodispersity, colloidal stability and a positive surface charge. The silicification products were exploited for the electrostatically driven assembly of a variety of mono- and bi-material hierarchical superstructures that were stable over a span of months. Additionally, we demonstrated the dominant role of the amine-containing Tris buffer catalyzing silica precipitation into much larger particles with a negative surface charge regardless of the reaction temperature or the sequence of the protein template.

In a follow-up study, we demonstrate the ability to mineralize silica particles of various sizes by changing the sequence of the Car9 segment and the temperature at which protein solutions are incubated prior to the addition of silicic acid precursor. By studying the temperature dependent micellization kinetics and silica mineralization outcomes, we gain fundamental understanding of the interplay between electrostatic repulsion of protein micelles and the silicification reaction kinetics as a function of sequence and temperature. We extract important design rules for the self-assembly of protein unimers including the crucial role of arginine-4 and insignificance of lysine-8 and lysine-11 in this process.

Further, we use silica mineralization to capture intricate and subtle differences in the protein templates (for example destabilization, weakened repulsive forces, or core compaction) that were otherwise indistinguishable using DLS and turbidity characterization. This simple biomimetic approach to synthesize positively charged silica NPs and hierarchical and composite superstructures eliminates the need for multiple precursors or surface modifications and provides a simple route to controlling the silicification products with genetic engineering of the peptide sequence, solution conditions, and reaction temperature. It also enables the custom synthesis of silica nanoparticles of tunable sizes and surface charges by introducing simple modifications of the macromolecular template paired with reaction temperature. This can be useful in heterogenous catalysis systems or modular drug delivery cases that need precise control over the pore size and electrostatic repulsion between components.

Not only have biomacromolecules proven useful for mediating the biomimetic mineralization of target inorganic materials, but they have also expanded the hierarchical and configurational capabilities and achieved precise control over the size, morphology, and arrangement of the mineralization outcomes. To achieve such control, biomolecules are designed to contain multiple domains or motifs that serve different functionalities including nucleation, capping, functionalization, surface decoration, and others. We used gold-binding ELPs to synthesize gold nanoparticles that can be reversibly assembled into clusters with distinct plasmonic signatures in response to temperature change. For both systems, we study how protein sequence and concentration, solution conditions, and temperature affect mineralization outcomes and plasmonic responses.

Finally, we transfer learnings from solid-binding peptides to sequence defined peptoids by designing a polymeric analog of the bio-inspired R5 silicifying peptides. We use experimental work to validate the differences in binding energy predicted by metadynamics calculations. MD simulations were also used to show that charged and polar residues lie in closer proximity to silica surfaces in the peptoid analog of the R5 peptide. Our work reveals that differences in binding energy could be useful in predicting biomimetic mineralization and identifies several key features that can aid in designing targeted mineralization templates in the future.

The biomimetic approaches to the synthesis of size- and composition-controlled nanomaterials described herein are simple and environmentally friendly, and the extracted design rules should prove useful for the biological fabrication of a broad range of hierarchical systems with applications in biomedicine and energy-related fields.

Appendix A Inorganic mineralization templated by self-assembling *de novo* designed protein fibers

A.1 Introduction

High information content biomacromolecules possess robust self-assembling capabilities that can be harnessed and engineered for structural and functional applications in nanotechnology.[2,11–13,176–180] Self-assembled biological building blocks including peptides[8,48,181,182] and proteins[183–185] have been shown to template mineralization of inorganic materials in natural and engineered systems. For example, self-assembly of amelogenin proteins regulates enamel biomineralization and has been shown to affect signaling and structural properties in dental cells. [186] However, designing self-assembling proteins to mimic natural systems, unlike DNA and short peptides, presents a unique set of challenges due to the complexity of protein-protein interactions and specificity and symmetry limitations. In an attempt to combat these design challenges, Ma *et al* exploited the self-assembling capabilities of peptoids (N-substituted polyglycines) to build a well-defined two-dimensional structural foundation functionalized with solid binding proteins to template the mineralization of TiO_2/Au nanocomposites.[59,174] Despite the chemical programmability and proteolytic robustness of peptoids, they cannot be modularly programmed for both self-assembly and inorganic mineralization.

In this work, we explore the mineralization of TiO_2 nanoparticles on self-assembling *de novo* designed protein fibers genetically fused to SBPs to nucleate inorganic mineralization. Fascinating studies focused on *de novo* designing protein building blocks capable of self-assembling into pseudosymmetric 2D arrays (sheets, helical bundles, and filaments) via noncovalent interactions.[187–190] Given the variability in their sizes and

architectures and their adaptability to design modifications and fusions, we proposed using *de novo* designed helical filaments (DHFs) that enable modular fusion of SBPs to their C- or N- termini as a scaffold for TiO_2 mineralization. This nascent project is in collaboration with Dr. Hao Shen, a Postdoctoral Fellow at the Institute for Protein Design.

A.2 Materials and Methods

A.2.1 DNA manipulation and protein purification

Early experiments were conducted using *de novo* repeat proteins: DHF58, DHF91, and DHF119 from previous work by Shen *et al*.[190] Additionally, two unpublished designs with varying architectures and dimensions were used HZ41 and HA13. The designs were expressed in *E. coli* under the control of a T7 promoter and purified by immobilized metal affinity chromatography (IMAC) as described in **Ref 190.**

A.2.2 Titania mineralization

Prior to mineralization experiments, protein concentrations were quantified using A_{280} measurements. A diluted precursor solution was freshly prepared by mixing 95 µL of Titanium (IV) bis(ammonium lactato) dihydroxide (TiBALDH, Sigma-Aldrich) with 105 µL DI-water and vortexing until dissolved. Aliquots (5 µL) of the TiBALDH solution were added to 400 µL of fiber solutions to reach final concentrations of 10 µM proteins in 20 mM Tris-HCl at pH 6.0. Each solution was vortexed for 20 seconds and rotated at 30 rpm for 2 hours or 6 days at room temperature. Tubes were placed in a 4ºC fridge overnight to sediment mineralization products. The supernatant was gently removed by pipetting, and pellets were resuspended in 500 µL of DI water. Resuspended mineralization products were then centrifuged at 10,000 g for 2 min and the supernatant was removed

by pipetting. This wash step was repeated twice to remove salts and unreacted TiBALDH before TEM. Mineralization products were finally resuspended in 200 µL of DI water for TEM characterization.

A.3 Results and Discussion

A.3.1 Self-assembly newly constructed Car9-tagged DHF monomers

We designed DHF monomers that each contain a Car9 fusion that will be displayed on the outer surface of the resulting self-assembled helical fibers. Since most of the existing monomers contain sfGFP,[190] we used fluorescence microscopy and TEM to verify whether the new SBP fusions hindered filament formation. Three fiber designs shown in **Fig. A.2** retained their self-assembling properties after genetically fusing Car9 to their termini: Car9-sfGFP-**DHF91**-His, His-**DHF119**-sfGFP-Car9, and His-**HA13**-sfGFP-Car9 (except for His-**DHF58**-sfGFP-Car9 that failed to assemble into fibers after expression and IMAC purification). Prior to mineralization experiments, we also tested out the influence of reaction buffer conditions on the resulting fibers and verified that they remain stable for 7 days at pH 6.0.

A.3.2 Titania mineralization on de novo self-assembling fibers

Proof of concept experiments revealed that solutions of Car9-sfGFP-DHF91-His, His-DHF119-sfGFP-Car9, and His-HA13-sfGFP-Car9 self-assembled fibers can template the precipitation of 5-nm TiO_2 nanoparticles. It was observed that the mineralized fibers tend to bundle as the reaction is allowed to progress longer (2 hours compared to 6 days). HR-TEM analysis confirmed discrete nanoparticles with a lattice spacing consistent with that of anatase TiO_2 (**Fig. A.5 B** courtesy of Dr. Biao Jin at PNNL). Control mineralization

experiments in fiber solutions lacking the Car9 fusions revealed the retained ability to precipitate anatase TiO_2 NPs over similar time frames. This was attributed to the positively charged His_6 tag used for purification.

To test out the influence of His_6 tag on non-specific mineralization, a new construct was designed with an engineered TEV protease cleavage site at the N-terminus of the monomer (called His-TEV-HA13-sfGFP-Car9). After the His tag was used for protein purification, it easily cleaved before TiO_2 precursor was added to the fiber solution. **Fig. A.6** shows resulting TiO_2 NPs were homogeneously distributed over the fibers and reported an average diameter of 5 ± 1 nm. Eliminating both His_6 and Car9 leads to aggregated, non-specific precipitating of Ti-containing materials that lacks structural or morphological control.

A.4 Conclusion

These results laid out important design considerations for building mineralization templates on *de novo* designed self-assembling fibers. We observed the influence of reaction time on producing large bundles of mineralized fibers and fully encapsulated mineralized structures. We observed non-specific mineralization on fibers that lacked Car9 fusion due to the His_6 purification tag that likely promoted the nucleation of TiO_2 similarly to Car9. Cleaving His_6 prior to the addition of precursor eliminates non-specific NPs where Car9 is capable of promoting the mineralization of homogeneously distributed anatase NPs in the 5-nm range. Next, we aim to control the NP distribution on the outer surface of the assembled fibers which can result in varying functionalities and catalytic properties. We will explore different-sized fiber monomers to control the distribution of functional Car9 fusions that are accessible to precursor molecules. Combining our

designs with pH-responsive fibers or peptide-dependent self-assembly can lead to intricate hierarchical and responsive systems.

Confined mineralization space and limited access to precursor molecules can drastically affect the resulting nanomaterials in terms of dimensions, shape, crystalline phase, and others. A few unsuccessful attempts were made to direct TiO_2 mineralization at the inner pores of *de novo* self-assembling fibers (HA13 and HZ41) that have larger inners pores compared to DHF constructs discussed in Chapter 4. We continue to try different SBP fusion designs that minimize steric hinderance between the charged moieties and enable self-assembly with the goal of directing mineralization to the inner pores. Other approaches can be explored to control the NP distribution on the outer surface of the assembled fibers including using different-sized fiber monomers to control the distribution of functional Car9 fusions that are accessible to precursor molecules. We can combine our designs with pH-responsive fibers or peptide-dependent self-assembly in the future to create more intricate hierarchical and responsive systems

In natural biomineralization systems, formation of enamel containing highly ordered bundles of apatite is thought to begin with the precipitation of calcium phosphate (CaP) mediated by amelogenin in the extracellular protein matrix.[191] *De novo* designed fibers offer a robust hierarchical system than can mimic this natural process with the goal of controlled CaP mineralization. The insights we gained from DHF designs and TiO_2 mineralization experiments can be translated into this complex system taking inspiration from recent work where self-assembled nanoribbons could template CaP nucleation.[191–193]

A.5 Figures

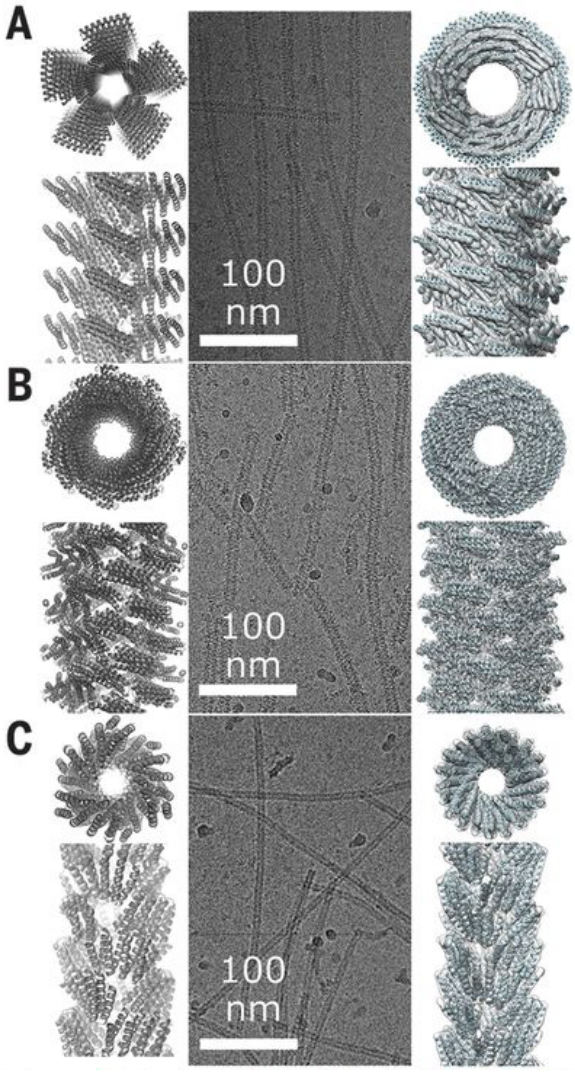

Figure A.1 Computational model (left), representative cryo-TEM images (middle), and cryo-EM structure (right) corresponding to DHF58 (A), DHF119 (B), and DHF91 (C) from **Ref** [190]**.**

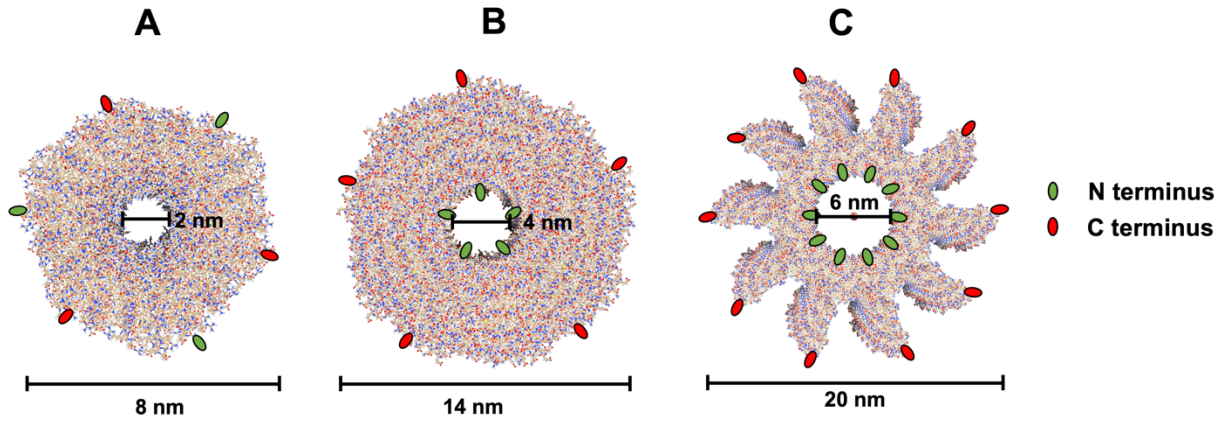

Figure A.2 Schematic showing the structure and dimensions of Car9-sfGFP-DHF91-His (A – PDB 6E9X), His-DHF119-sfGFP-Car9 (B – PDB 6E9Z), and His-HA13-sfGFP-Car9 (C) based on cryo-EM analysis.

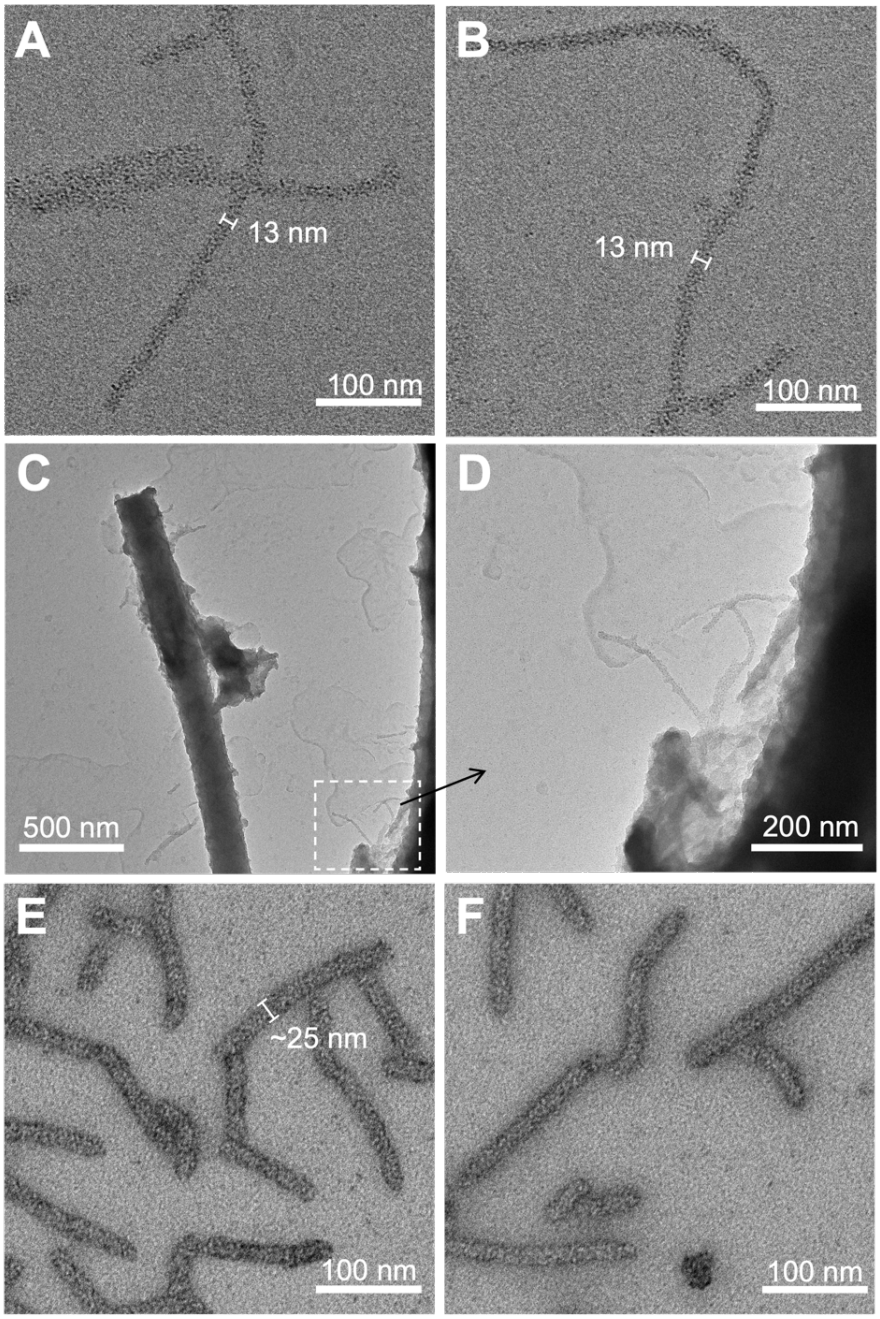

Figure A.3 TEM micrographs of unstained TiO_2 mineralization products from 10 μM solutions of Car9-sfGFP-DHF91-His after 2 hours (A-B) or 6 days (C-D). Control experiment used sfGFP-DHF91-His lacking the Car9 N-terminal fusion (E-F).

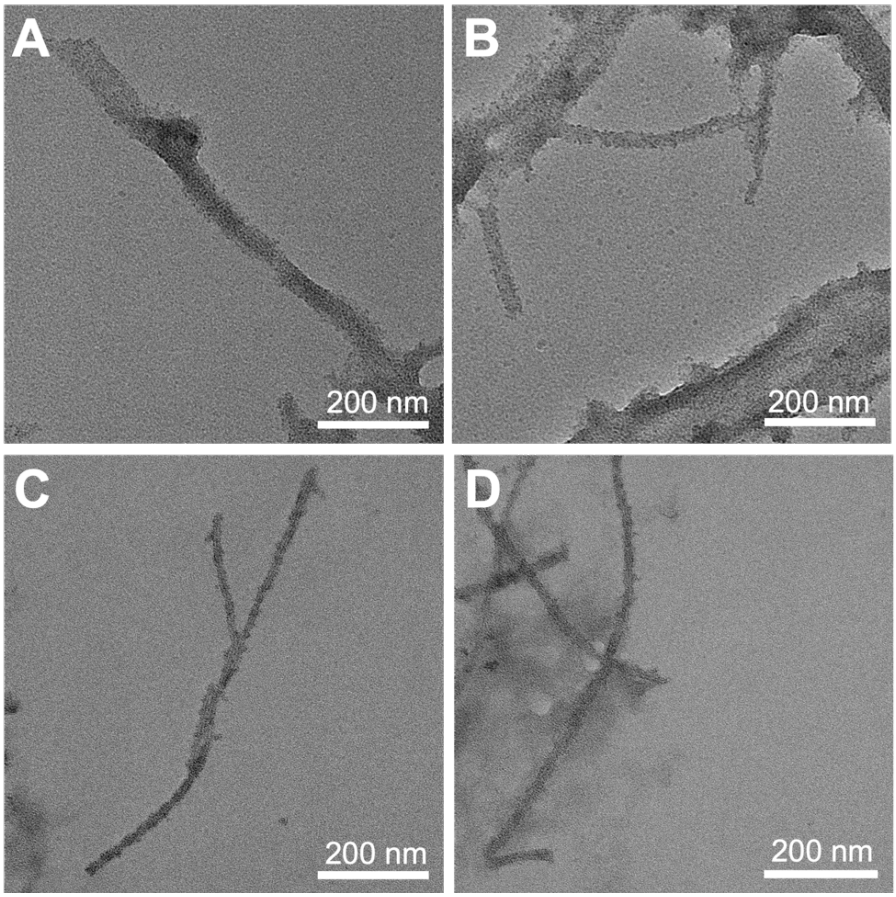

Figure A.4 TEM micrographs of unstained TiO_2 mineralization products after 2 hours in from 10 μM solutions of His-DHF119-sfGFP-Car9 (A-B) or His-DHF119-sfGFP lacking the Car9 C-terminal fusion (C-D).

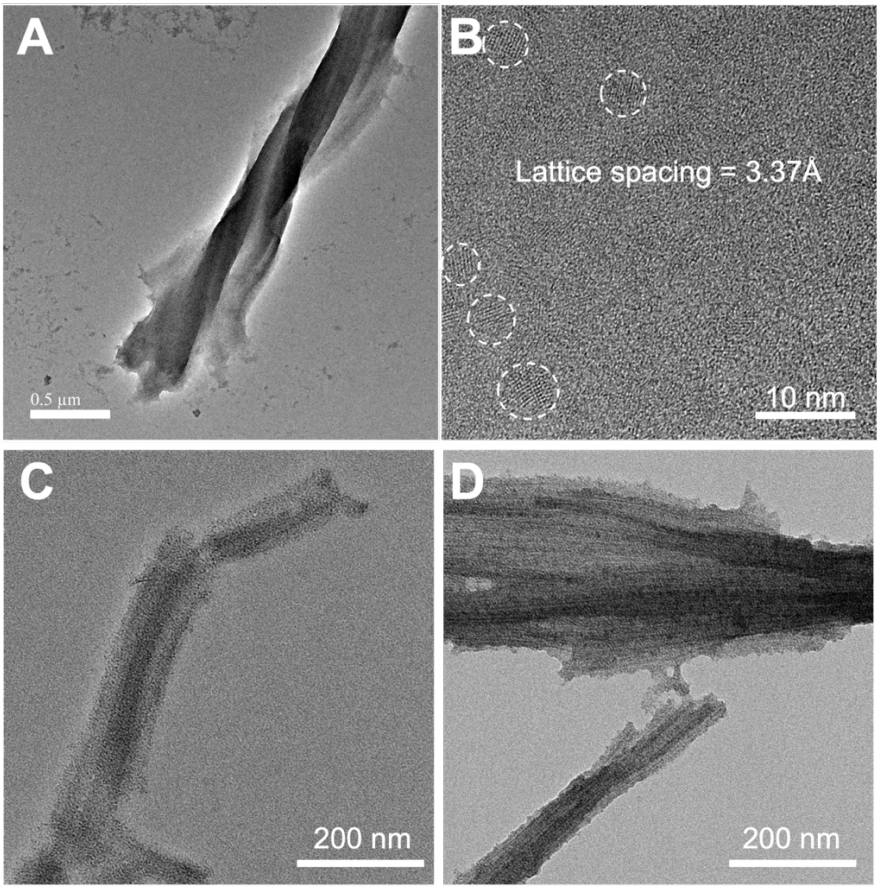

Figure A.5 TEM micrographs of unstained TiO_2 mineralization products after 6 days in from 10 µM solutions of His-HA13-sfGFP-Car9 (A-B) or His-HA13-sfGFP lacking the Car9 C-terminal fusion (C-D).

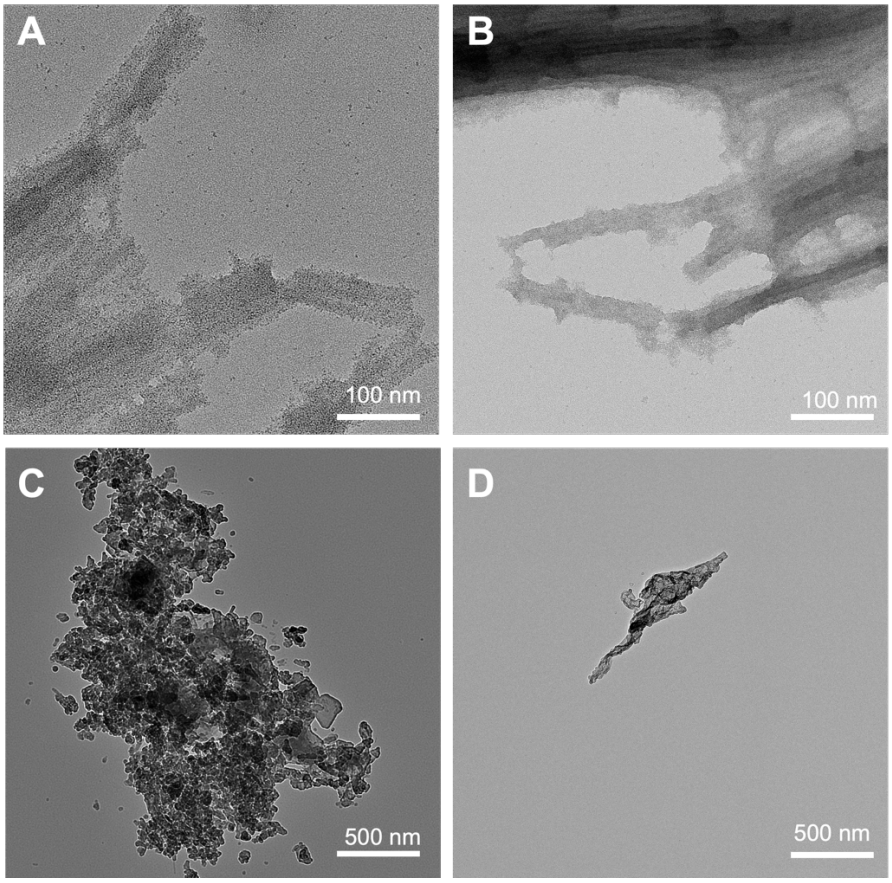

Figure A.6 TEM micrographs of unstained TiO_2 mineralization products after 2 hours in from 10 μM solutions of HA13-sfGFP-Car9 (A-B) or HA13-sfGFP lacking the Car9 C-terminal fusion (C-D). His_6 tag was cleaved from both constructs prior to the mineralization reaction.

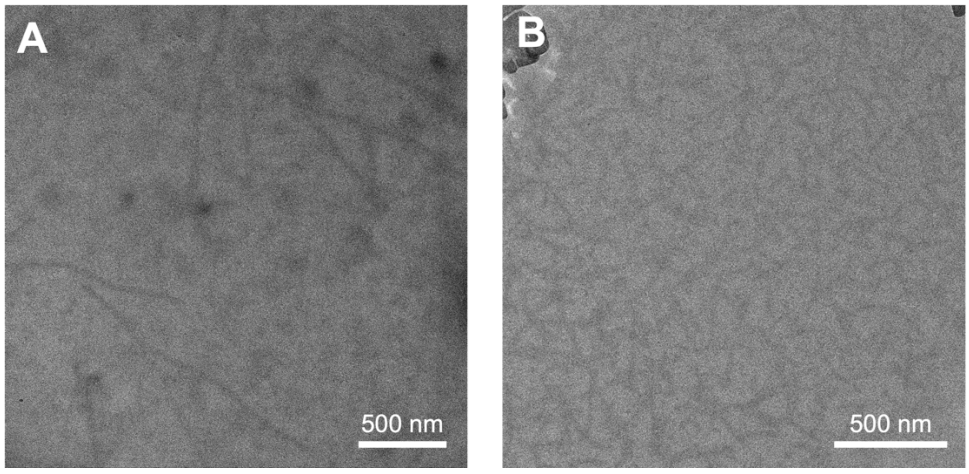

Figure A.7 TEM images of unstained fibers comprised of His-DHF119-sfGFP (A) and sfGFP-DHF91-His (B) monomers without the addition of TiBALDH precursor.

Funding Information

This material is based upon work supported by the US Department of Energy, Office of Science, Office of Basic Energy Sciences, as part of the Energy Frontier Research Centers program: CSSAS, The Center for the Science of Synthesis Across Scales under Award Number DE-SC0019288. SEM, TEM, and AFM imaging was performed at the Molecular Analysis Facility, a National Nanotechnology Coordinated Infrastructure site at the University of Washington supported in part by the National Science Foundation (awards NNCI-2025489, NNCI-1542101), the University of Washington, the Molecular Engineering & Sciences Institute, and the Clean Energy Institute. I would like to thank the Clean Energy Institute for support. The computational work was completed through the advanced computational, storage, and networking infrastructure provided by the Hyak supercomputer system and funded by the STF at the University of Washington. Peptoid synthesis and purification were performed at the Pacific Northwest National Laboratory (PNNL). PNNL is multi-program national laboratory operated for Department of Energy by Battelle under Contracts No. DE-AC05-76RL01830.

References

1. Seeman, N. C. & Belcher, A. M. *Emulating Biology: Building Nanostructures from the Bottom Up*. *PNAS* **99**, 6451–6455 (2002).
2. Brodin, J. D. *et al.* Metal-directed, chemically tunable assembly of one-, two- and three-dimensional crystalline protein arrays. *Nat Chem* **4**, 375–382 (2012).
3. Chworos, A. *et al.* Building Programmable Jigsaw Puzzles with RNA. *Science* **306**, 2068–2072 (2004).
4. Delebecque, C. J., Lindner, A. B., Silver, P. A. & Aldaye, F. A. Organization of Intracellular Reactions with Rationally Designed RNA Assemblies. *Science* **333**, 470–474 (2011).
5. Nykypanchuk, D., Maye, M. M., Van Der Lelie, D. & Gang, O. DNA-guided crystallization of colloidal nanoparticles. *Nature* **451**, 549–552 (2008).
6. Rothemund, P. W. K. Folding DNA to create nanoscale shapes and patterns. *Nature* **440**, 297–302 (2006).
7. Winegar, P. H. *et al.* DNA-Directed Protein Packing within Single Crystals. *Chem* **6**, 1007–1017 (2020).
8. Levin, A. *et al.* Biomimetic peptide self-assembly for functional materials. *Nature Reviews Chemistry* **4**, 615–634 (2020).
9. Zhang, J. *et al.* Microfabrication of peptide self-assemblies: inspired by nature towards applications. *Chemical Society Reviews* **51**, 6936–6947 (2022).
10. Cai, C., Lin, J., Lu, Y., Zhang, Q. & Wang, L. Polypeptide self-assemblies: Nanostructures and bioapplications. *Chemical Society Reviews* **45**, 5985–6012 (2016).
11. Zhu, J. *et al.* Protein Assembly by Design. *Chemical Reviews* **121**, 13701–13796 (2021).
12. Yang, G. *et al.* Highly Ordered Self-Assembly of Native Proteins into 1D, 2D, and 3D Structures Modulated by the Tether Length of Assembly-Inducing Ligands. *Angewandte Chemie* **129**, 10831–10835 (2017).
13. Whitesides, G. & Grzybowski, B. Self-Assembly at All Scales. *Science (1979)* **295**, 2418–2421 (2002).
14. Noy, A. Bionanoelectronics. *Advanced Materials* **23**, 807–820 (2011).
15. Hemmatian, Z. *et al.* Electronic control of H+ current in a bioprotonic device with Gramicidin A and Alamethicin. *Nat Commun* **7**, (2016).

16. Soto-Rodríguez, J., Hemmatian, Z., Josberger, E. E., Rolandi, M. & Baneyx, F. A Palladium-Binding Deltarhodopsin for Light-Activated Conversion of Protonic to Electronic Currents. *Advanced Materials* **28**, 6581–6585 (2016).

17. Soto-Rodríguez, J., Hemmatian, Z., Black, J., Rolandi, M. & Baneyx, F. Two-Channel Bioprotonic Photodetector. *ACS Appl Bio Mater* **2**, 930–935 (2019).

18. Kröger, N., Deutzmann, R. & Sumper, M. Polycationic peptides from diatom biosilica that direct silica nanosphere formation. *Science (1979)* **286**, 1129–1132 (1999).

19. Knecht, M. R. & Wright, D. W. Functional analysis of the biomimetic silica precipitating activity of the R5 peptide from Cylindrotheca fusiformis. *Chemical Communications* **3**, 3038–3039 (2003).

20. Belton, D. J., Deschaume, O. & Perry, C. C. An overview of the fundamentals of the chemistry of silica with relevance to biosilicification and technological advances. *FEBS Journal* **279**, 1710–1720 (2012).

21. Lechner, C. C. & Becker, C. F. W. A sequence-function analysis of the silica precipitating silaffin R5 peptide. *Journal of Peptide Science* **20**, 152–158 (2014).

22. Brown, S. Metal-recognition by repeating polypeptides. *Nat Biotechnol* **15**, 269–272 (1997).

23. Pushpavanam, K., Ma, J., Cai, Y., Naser, N. Y. & Baneyx, F. Solid-Binding Proteins: Bridging Synthesis, Assembly, and Function in Hybrid and Hierarchical Materials Fabrication. *Annu Rev Chem Biomol Eng* **12**, 333–357 (2021).

24. Thai, C. K. *et al.* Identification and characterization of Cu2O- and ZnO-binding polypeptides by escherichia coli cell surface display: Toward an understanding of metal oxide binding. *Biotechnol Bioeng* **87**, 129–137 (2004).

25. Date, T., Sekine, J., Matsuno, H. & Serizawa, T. Polymer-binding peptides for the noncovalent modification of polymer surfaces: Effects of peptide density on the subsequent immobilization of functional proteins. *ACS Appl Mater Interfaces* **3**, 351–359 (2011).

26. Brandon L. Coyle, Marco Rolandi, and F. B. Carbon-Binding Designer Proteins that Discriminate between sp2 - and sp3 -Hybridized Carbon Surfaces. *Bone* **23**, 1–7 (2014).

27. Qi, X. *et al.* Predictive Theoretical Framework for Dynamic Control of Bioinspired Hybrid Nanoparticle Self-Assembly. *ACS Nano* **16**, 1919–1928 (2022).

28. Coyle, B. L. & Baneyx, F. A cleavable silica-binding affinity tag for rapid and inexpensive protein purification. *Biotechnol Bioeng* **111**, 2019–2026 (2014).

29. Yang, W., Hellner, B. & Baneyx, F. Self-Immobilization of Car9 Fusion Proteins within High Surface Area Silica Sol-Gels and Dynamic Control of Protein Release. *Bioconjug Chem* **27**, 2450–2459 (2016).

30. Hellner, B., Lee, S. B., Subramaniam, A., Subramanian, V. R. & Baneyx, F. Modeling the Cooperative Adsorption of Solid-Binding Proteins on Silica: Molecular Insights from Surface Plasmon Resonance Measurements. *Langmuir* **35**, 5013–5020 (2019).

31. Hellner, B. *et al.* Sequence-Structure-Binding Relationships Reveal Adhesion Behavior of the Car9 Solid-Binding Peptide: An Integrated Experimental and Simulation Study. *J Am Chem Soc* **142**, 2355–2363 (2020).

32. Dunakey, S. J. G. *et al.* Selective Labeling and Decoration of the Ends and Sidewalls of Single-Walled Carbon Nanotubes Using Mono- and Bispecific Solid-Binding Fluorescent Proteins. *Bioconjug Chem* (2019) doi:10.1021/acs.bioconjchem.9b00097.

33. Ma, J. *et al.* Nanoparticle-mediated assembly of peptoid nanosheets functionalized with solid-binding proteins: Designing heterostructures for hierarchy. *Nano Lett* **21**, 1636–1642 (2021).

34. Peelle, B. R., Krauland, E. M., Dane Wittrup, K. & Belcher, A. M. Design criteria for engineering inorganic material-specific peptides. *Langmuir* **21**, 6929–6933 (2005).

35. Puddu, V., Slocik, J. M., Naik, R. R. & Perry, C. C. Titania binding peptides as templates in the biomimetic synthesis of stable titania nanosols: Insight into the role of buffers in peptide-mediated mineralization. *Langmuir* **29**, 9464–9472 (2013).

36. Hellner, B., Stegmann, A. E., Pushpavanam, K., Bailey, M. J. & Baneyx, F. Phase Control of Nanocrystalline Inclusions in Bioprecipitated Titania with a Panel of Mutant Silica-Binding Proteins. *Langmuir* **36**, 8503–8510 (2020).

37. Pushpavanam, K., Hellner, B. & Baneyx, F. Interrogating biomineralization one amino acid at a time: amplification of mutational effects in protein-aided titania morphogenesis through reaction-diffusion control. *Chemical Communications* **57**, 4803–4806 (2021).

38. Papike, J. J. & Cameron, M. Crystal chemistry of silicate minerals of geophysical interest. *Reviews of Geophysics* **14**, 37–80 (1976).

39. Lechner, C. C. & Becker, C. F. W. Silaffins in silica biomineralization and biomimetic silica precipitation. *Mar Drugs* **13**, 5297–5333 (2015).

40. Estroff, L. A. Introduction: Biomineralization. *Chemical Reviews* **108**, 4329–4331 (2008).

41. Dorval Courchesne, N. M., Steiner, S. A., Cantú, V. J., Hammond, P. T. & Belcher, A. M. Biotemplated Silica and Silicon Materials as Building Blocks for Micro- to Nanostructures. *Chemistry of Materials* **27**, 5361–5370 (2015).

42. Ciriminna, R. *et al.* The Sol–Gel Route to Advanced Silica-Based Materials and Recent Applications. *Chem Rev* **113**, 6592–6620 (2013).

43. Hyde, E. D. E. R., Seyfaee, A., Neville, F. & Moreno-Atanasio, R. Colloidal Silica Particle Synthesis and Future Industrial Manufacturing Pathways: A Review. *Industrial and Engineering Chemistry Research* **55**, 8891–8913 (2016).

44. Abdelhamid, M. A. A. & Pack, S. P. Biomimetic and bioinspired silicifications: Recent advances for biomaterial design and applications. *Acta Biomaterialia* **120**, 38–56 (2021).

45. Hildebrand, M. Diatoms, biomineralization processes, and genomics. *Chem Rev* **108**, 4855–4874 (2008).

46. Heintze, C. *et al.* An intimate view into the silica deposition vesicles of diatoms. *BMC Mater* **2**, 1–15 (2020).

47. Buckle, E. L. *et al.* Trimethylation of the R5 Silica-Precipitating Peptide Increases Silica Particle Size by Redirecting Orthosilicate Binding. *ChemBioChem* **21**, 3208–3211 (2020).

48. Kröger, N., Lorenz, S., Brunner, E. & Sumper, M. Self-assembly of highly phosphorylated silaffins and their function in biosilica morphogenesis. *Science (1979)* **298**, 584–586 (2002).

49. Lechner, C. C. & Becker, C. F. W. Exploring the effect of native and artificial peptide modifications on silaffin induced silica precipitation. *Chem Sci* **3**, 3500–3504 (2012).

50. Kröger, N., Deutzmann, R., Bergsdorf, C. & Sumper, M. Species-specific polyamines from diatoms control silica morphology. *PNAS* **97**, 14133–14138 (2000).

51. Sumper, M., Lorenz, S. & Brunner, E. Biomimetic Control of Size in the Polyamine-Directed Formation of Silica Nanospheres. *Angewandte Chemie - International Edition* **42**, 5192–5195 (2003).

52. Senior, L. *et al.* Structure and function of the silicifying peptide R5. *J Mater Chem B* **3**, 2607–2614 (2015).

53. Lopez, P. J., Gautier, C., Livage, J. & Coradin, T. *Mimicking Biogenic Silica Nanostructures Formation*. *Current Nanoscience* vol. 1 (2005).

54. Coradin, T., Durupthy, O. & Livage, J. Interactions of amino-containing peptides with sodium silicate and colloidal silica: A biomimetic approach of silicification. *Langmuir* **18**, 2331–2336 (2002).

55. Dickerson, M. B., Sandhage, K. H. & Naik, R. R. Protein- and peptide-directed syntheses of inorganic materials. *Chem Rev* **108**, 4935–4978 (2008).

56. Limo, M. J. *et al.* Interactions between Metal Oxides and Biomolecules: from Fundamental Understanding to Applications. *Chem Rev* **118**, 11118–11193 (2018).

57. Chen, C. L. & Rosi, N. L. Peptide-based methods for the preparation of nanostructured inorganic materials. *Angewandte Chemie - International Edition* **49**, 1924–1942 (2010).

58. Coyle, B. L. & Baneyx, F. Direct and reversible immobilization and microcontact printing of functional proteins on glass using a genetically appended silica-binding tag. *Chemical Communications* **52**, 7001–7004 (2016).

59. Ma, J. *et al.* Controlling Mineralization with Protein-Functionalized Peptoid Nanotubes. *Advanced Materials* **35**, (2023).

60. Cai, Y. *et al.* Towards predictive control of reversible nanoparticle assembly with solid-binding proteins. *Soft Matter* **20**, 1935–1942 (2024).

61. Hernández-Gordillo, A., Hernández-Arana, A., Campero-Celis, A. & Vera-Robles, L. I. TiBALDH as a precursor for biomimetic TiO2 synthesis: Stability aspects in aqueous media. *RSC Adv* **9**, 34559–34566 (2019).

62. Gunnar, S. *et al.* Evolution of the Polymorph Selectivity of Titania Formation under Acidic and Low-Temperature Conditions. (2019) doi:10.1021/acsomega.8b03440.

63. Kharlampieva, E. *et al.* Bioenabled surface-mediated growth of titania nanoparticles. *Advanced Materials* **20**, 3274–3279 (2008).

64. Sewell, S. L. & Wright, D. W. Biomimetic synthesis of titanium dioxide utilizing the R5 peptide derived From Cylindrotheca fusiformis. *Chemistry of Materials* **18**, 3108–3113 (2006).

65. Kröger, N. *et al.* Bioenabled synthesis of rutile (TiO2) at ambient temperature and neutral pH. *Angewandte Chemie - International Edition* **45**, 7239–7243 (2006).

66. Link, S. & El-Sayed, M. A. Size and temperature dependence of the plasmon absorption of colloidal gold nanoparticles. *Journal of Physical Chemistry B* **103**, 4212–4217 (1999).

67. Naik, R. R., Stringer, S. J., Agarwal, G., Jones, S. E. & Stone, M. O. Biomimetic synthesis and patterning of silver nanoparticles. *Nat Mater* **1**, 169–172 (2002).

68. Slocik, J. M., Stone, M. O. & Naik, R. R. Synthesis of gold nanoparticles using multifunctional peptides. *Small* **1**, 1048–1052 (2005).

69. Slocik, J. M. & Naik, R. R. Biologically programmed synthesis of bimetallic nanostructures. *Advanced Materials* **18**, 1988–1992 (2006).

70. Li, Y., Tang, Z., Prasad, P. N., Knecht, M. R. & Swihart, M. T. Peptide-mediated synthesis of gold nanoparticles: Effects of peptide sequence and nature of binding on physicochemical properties. *Nanoscale* **6**, 3165–3172 (2014).

71. Song, C., Zhao, G., Zhang, P. & Rosi, N. L. Expeditious synthesis and assembly of sub-100 nm hollow spherical gold nanoparticle superstructures. *J Am Chem Soc* **132**, 14033–14035 (2010).

72. Lachowski, K. J., Vaddi, K., Naser, N. Y., Baneyx, F. & Pozzo, L. D. Multivariate analysis of peptide-driven nucleation and growth of Au nanoparticles. *Digital Discovery* (2022) doi:10.1039/d2dd00017b.

73. Chen, C. L., Zhang, P. & Rosi, N. L. A new peptide-based method for the design and synthesis of nanoparticle superstructures: Construction of highly ordered gold nanoparticle double helices. *J Am Chem Soc* **130**, 13555–13557 (2008).

74. Zhou, W., Gao, X., Liu, D. & Chen, X. Gold Nanoparticles for in Vitro Diagnostics. *Chemical Reviews* **115**, 10575–10636 (2015).

75. Saha, K., Agasti, S. S., Kim, C., Li, X. & Rotello, V. M. Gold nanoparticles in chemical and biological sensing. *Chemical Reviews* **112**, 2739–2779 (2012).

76. Chen, M. & Goodman, D. W. Catalytically active gold: From nanoparticles to ultrathin films. *Acc Chem Res* **39**, 739–746 (2006).

77. Grabow, L. C. & Mavrikakis, M. Nanocatalysis beyond the gold-rush era. *Angewandte Chemie - International Edition* **47**, 7390–7392 (2008).

78. Liu, Y. & Yang, Y. Recent progress of TiObased anodes for Li ion batteries. *J Nanomater* **2016**, (2016).

79. Lan, Y., Lu, Y. & Ren, Z. Mini review on photocatalysis of titanium dioxide nanoparticles and their solar applications. *Nano Energy* **2**, 1031–1045 (2013).

80. Ding, T. & Baumberg, J. J. Thermo-responsive plasmonic systems: Old materials with new applications. *Nanoscale Advances* **2**, 1410–1416 (2020).

81. Thaggard, G. C., Haimerl, J., Fischer, R. A., Park, K. C. & Shustova, N. B. Traffic Lights for Catalysis: Stimuli-Responsive Molecular and Extended Catalytic Systems. *Angewandte Chemie - International Edition* **62**, e202302859 (2023).

82. Zhu, M. Q., Wang, L. Q., Exarhos, G. J. & Li, A. D. Q. Thermosensitive Gold Nanoparticles. *J Am Chem Soc* **126**, 2656–2657 (2004).

83. Yang, Y. J., Holmberg, A. L. & Olsen, B. D. Artificially Engineered Protein Polymers. *Annu. Rev. Chem. Biomol. Eng.* **8**, 549–75 (2017)

84. Shah, R. A., Frazar, E. M. & Hilt, J. Z. Recent developments in stimuli responsive nanomaterials and their bionanotechnology applications. *Current Opinion in Chemical Engineering* **30**, 103–111 (2020).

85. Blum, A. P. *et al.* Stimuli-responsive nanomaterials for biomedical applications. *Journal of the American Chemical Society* **137**, 2140–2154 (2015).

86. Pham, S. H., Choi, Y. & Choi, J. Stimuli-responsive nanomaterials for application in antitumor therapy and drug delivery. *Pharmaceutics* **12**, 1–19 (2020).

87. Cai, C. *et al.* Simulation-assisted self-assembly of multicomponent polymers into hierarchical assemblies with varied morphologies. *Angewandte Chemie - International Edition* **52**, 7732–7736 (2013).

88. Li, Z. & Yin, Y. Stimuli-Responsive Optical Nanomaterials. *Advanced Materials* **31**, 1807061 (2019).

89. Halperin, A., Kröger, M. & Winnik, F. M. Poly(N-isopropylacrylamide) Phase Diagrams: Fifty Years of Research. *Angewandte Chemie* **127**, 15558–15586 (2015).

90. Haq, M. A., Su, Y. & Wang, D. Mechanical properties of PNIPAM based hydrogels: A review. *Materials Science and Engineering C* **70**, 842–855 (2017).

91. Schild, H. G. Poly(N-isopropylacrylamide): experiment, theory and application. *Prog Polym Sci* **17**, 163–249 (1992).

92. Qian, J. & Wu, F. Thermosensitive PNIPAM semi-hollow spheres for controlled drug release. *J Mater Chem B* **1**, 3464–3469 (2013).

93. Pippa, N., Meristoudi, A., Pispas, S. & Demetzos, C. Temperature-dependent drug release from DPPC:C12H25-PNIPAM-COOH liposomes: Control of the drug loading/release by modulation of the nanocarriers' components. *Int J Pharm* **485**, 374–382 (2015).

94. Vikulina, A. S., Feoktistova, N. A., Balabushevich, N. G., Von Klitzing, R. & Volodkin, D. Cooling-Triggered Release from Mesoporous Poly(N-isopropylacrylamide) Microgels at Physiological Conditions. *ACS Appl Mater Interfaces* **12**, 57401–57409 (2020).

95. Raissi, H. & Pasban, S. PNIPAM/Hexakis as a thermosensitive drug delivery system for biomedical and pharmaceutical applications. *Sci Rep* **12**, (2022).

96. Qian, Z., Guye, K. N., Masiello, D. J. & Ginger, D. S. Dynamic Optical Switching of Polymer/Plasmonic Nanoparticle Hybrids with Sparse Loading. *Journal of Physical Chemistry B* **121**, 1092–1099 (2017).

97. Choe, A. *et al.* Stretchable and wearable colorimetric patches based on thermoresponsive plasmonic microgels embedded in a hydrogel film. *NPG Asia Mater* **10**, 912–922 (2018).

98. Meyer, D. E. & Chilkoti, A. Quantification of the effects of chain length and concentration on the thermal behavior of elastin-like polypeptides. *Biomacromolecules* **5**, 846–851 (2004).

99. Cho, Y. *et al.* Effects of hofmeister anions on the phase transition temperature of elastin-like polypeptides. *Journal of Physical Chemistry B* **112**, 13765–13771 (2008).

100. Quiroz, F. G. & Chilkoti, A. Sequence heuristics to encode phase behaviour in intrinsically disordered protein polymers. *Nat Mater* **14**, 1164–1171 (2015).

101. Mills, C. E., Ding, E. & Olsen, B. D. Cononsolvency of Elastin-like Polypeptides in Water/Alcohol Solutions. *Biomacromolecules* **20**, 2167–2173 (2019).

102. Trabbic-Carlson, K. *et al.* Effect of protein fusion on the transition temperature of an environmentally responsive elastin-like polypeptide: A role for surface hydrophobicity? *Protein Engineering, Design and Selection* **17**, 57–66 (2004).

103. Meyer, D. E. & Chilkoti, A. *Purification of Recombinant Proteins by Fusion with Thermally-Responsive Polypeptides*. *NATURE BIOTECHNOLOGY* vol. 17 http://biotech.nature.com (1999).

104. Lee, T. A. T., Cooper, A., Apkarian, R. P. & Conticello, V. P. Thermo-reversible self-assembly of nanoparticles derived from elastin-mimetic polypeptides. *Advanced Materials* **12**, 1105–1110 (2000).

105. Han, W., Chilkoti, A. & López, G. P. Self-assembled hybrid elastin-like polypeptide/silica nanoparticles enable triggered drug release. *Nanoscale* **9**, 6178–6186 (2017).

106. Saha, S., Banskota, S., Roberts, S., Kirmani, N. & Chilkoti, A. Engineering the Architecture of Elastin-Like Polypeptides: From Unimers to Hierarchical Self-Assembly. *Adv Ther (Weinh)* **3**, 1900164 (2020).

107. Jenkins, I. C., Milligan, J. J. & Chilkoti, A. Genetically Encoded Elastin-Like Polypeptides for Drug Delivery. *Advanced Healthcare Materials* **10**, 2100209 (2021).

108. Milligan, J. J., Saha, S., Jenkins, I. C. & Chilkoti, A. Genetically encoded elastin-like polypeptide nanoparticles for drug delivery. *Curr Opin Biotechnol* **74**, 146–153 (2022).

109. Le, D. H. T. & Sugawara-Narutaki, A. Elastin-like polypeptides as building motifs toward designing functional nanobiomaterials. *Molecular Systems Design and Engineering* **4**, 545–565 (2019).

110. Sun, M. *et al.* Thermally Triggered in Situ Assembly of Gold Nanoparticles for Cancer Multimodal Imaging and Photothermal Therapy. *ACS Appl Mater Interfaces* **9**, 10453–10460 (2017).

111. Simon, J. R., Carroll, N. J., Rubinstein, M., Chilkoti, A. & López, G. P. Programming molecular self-assembly of intrinsically disordered proteins containing sequences of low complexity. *Nat Chem* **9**, 509–515 (2017).

112. Li, L. *et al.* Functional Modification of Silica through Enhanced Adsorption of Elastin-Like Polypeptide Block Copolymers. *Biomacromolecules* **19**, 298–306 (2018).

113. Alvisi, N. *et al.* Self-assembly of elastin-like polypeptide brushes on silica surfaces and nanoparticles. *Biomacromolecules* **22**, 1966–1979 (2021).

114. Han, W., MacEwan, S. R., Chilkoti, A. & López, G. P. Bio-inspired synthesis of hybrid silica nanoparticles templated from elastin-like polypeptide micelles. *Nanoscale* **7**, 12038–12044 (2015).

115. Qiu, Y., Lin, Y. & Zhang, G. Unique silica biomimetic mineralization of acidic elastin-like polypeptides without hydroxyl and charged residues. *Int J Biol Macromol* **153**, 224–231 (2020).

116. Patwardhan, S. V. *et al.* Chemistry of aqueous silica nanoparticle surfaces and the mechanism of selective peptide adsorption. *J Am Chem Soc* **134**, 6244–6256 (2012).

117. Ciriminna, R. *et al.* The sol-gel route to advanced silica-based materials and recent applications. *Chemical Reviews* **113**, 6592–6620 (2013).

118. Kang, H., Long, D. J. & Haynes, C. L. Preparation of Colloidally Stable Positively Charged Hollow Silica Nanoparticles: Effect of Minimizing Hydrolysis on ζ Potentials. *Langmuir* **35**, 7985–7994 (2019).

119. Liu, Z., Bode, V., Hadayati, P., Onay, H. & Sudhölter, E. J. R. Understanding the stability mechanism of silica nanoparticles: The effect of cations and EOR chemicals. *Fuel* **280**, (2020).

120. Naik, R. R., Brott, L. L., Clarson, S. J. & Stone, M. O. Silica-Precipitating Peptides Isolated from a Combinatorial Phage Display Peptide Library. *J Nanosci Nanotechnol* **2**, 95–100 (2002).

121. Zhao, B., Li, N. K., Yingling, Y. G. & Hall, C. K. LCST Behavior is Manifested in a Single Molecule: Elastin-Like polypeptide (VPGVG)n. *Biomacromolecules* **17**, 111–118 (2016).

122. MacEwan, S. R. & Chilkoti, A. Elastin-like polypeptides: biomedical applications of tunable biopolymers. *Biopolymers* **94**, 60–77 (2010).

123. Rodríguez-Cabello, J. C., Arias, F. J., Rodrigo, M. A. & Girotti, A. Elastin-like polypeptides in drug delivery. *Advanced Drug Delivery Reviews* **97**, 85–100 (2016).

124. Varanko, A. K., Su, J. C. & Chilkoti, A. Elastin-Like Polypeptides for Biomedical Applications. *Annu Rev Biomed Eng* **22**, 343–369 (2020).

125. Shah, M. *et al.* Biodegradation of elastin-like polypeptide nanoparticles. *Protein Science* **21**, 743–750 (2012).

126. Anthis, N. J. & Clore, G. M. Sequence-specific determination of protein and peptide concentrations by absorbance at 205 nm. *Protein Science* **22**, 851–858 (2013).

127. Nečas, D. & Klapetek, P. Gwyddion: An open-source software for SPM data analysis. *Central European Journal of Physics* **10**, 181–188 (2012).

128. Rao, J., Luo, Z., Ge, Z., Liu, H. & Liu, S. 'Schizophrenic' micellization associated with coil-to-helix transitions based on polypeptide hybrid double hydrophilic rod-coil diblock copolymer. *Biomacromolecules* **8**, 3871–3878 (2007).

129. Cai, C., Lin, J., Chen, T., Wang, X. S. & Lin, S. Super-helices self-assembled from a binary system of amphiphilic polypeptide block copolymers and polypeptide homopolymers. *Chemical Communications* 2709–2711 (2009) doi:10.1039/b823367e.

130. Cai, C., Zhu, W., Chen, T., Lin, J. & Tian, X. Synthesis and Self-assembly behavior of amphiphilic polypeptide-based brush-coil block copolymers. *J Polym Sci A Polym Chem* **47**, 5967–5978 (2009).

131. Karg, M., Hellweg, T. & Mulvaney, P. Self-assembly of tunable nanocrystal superlattices using poly-(NIPAM) spacers. *Adv Funct Mater* **21**, 4668–4676 (2011).

132. Zhu, W., Lin, J. & Cai, C. The effect of a thermo-responsive polypeptide-based copolymer on the mineralization of calcium carbonate. *J Mater Chem* **22**, 3939–3947 (2012).

133. Garanger, E. *et al.* Structural Evolution of a Stimulus-Responsive Diblock Polypeptide Micelle by Temperature Tunable Compaction of its Core. *Macromolecules* **48**, 6617–6627 (2015).

134. Widder, K. *et al.* Characterisation of hydration and nanophase separation during the temperature response in hydrophobic/hydrophilic elastin-like polypeptide (ELP) diblock copolymers. *Soft Matter* **13**, 1816–1822 (2017).

135. MacEwan, S. R. *et al.* Phase Behavior and Self-Assembly of Perfectly Sequence-Defined and Monodisperse Multiblock Copolypeptides. *Biomacromolecules* **18**, 599–609 (2017).

136. Hassouneh, W., Zhulina, E. B., Chilkoti, A. & Rubinstein, M. Elastin-like Polypeptide Diblock Copolymers Self-Assemble into Weak Micelles. *Macromolecules* **48**, 4183–4195 (2015).

137. Choi, J. W., Choi, S. H. & Won, J. I. Self-Assembly Behavior of Elastin-like Polypeptide Diblock Copolymers Containing a Charged Moiety. *Biomacromolecules* **22**, 2604–2613 (2021).

138. Dreher, M. R. *et al.* Temperature triggered self-assembly of polypeptides into multivalent spherical micelles. *J Am Chem Soc* **130**, 687–694 (2008).

139. Sharma, B., Ma, Y., Ferguson, A. L. & Liu, A. P. In search of a novel chassis material for synthetic cells: emergence of synthetic peptide compartment. *Soft Matter* **16**, 10769–10780 (2020).

140. Roberts, S., Dzuricky, M. & Chilkoti, A. Elastin-like polypeptides as models of intrinsically disordered proteins. *FEBS Lett* **589**, 2477–2486 (2015).

141. Kuno, T., Nonoyama, T., Hirao, K. & Kato, K. Influence of the charge relay effect on the silanol condensation reaction as a model for silica biomineralization. *Langmuir* **27**, 13154–13158 (2011).

142. Larson-Smith, K., Jackson, A. & Pozzo, D. C. Small angle scattering model for Pickering emulsions and raspberry particles. *J Colloid Interface Sci* **343**, 36–41 (2010).

143. Roth, K. M., Zhou, Y., Yang, W. & Morse, D. E. Bifunctional small molecules are biomimetic catalysts for silica synthesis at neutral pH. *J Am Chem Soc* **127**, 325–330 (2005).

144. Berg, J. C. *An Introduction to Interfaces & Colloids: The Bridge to Nanoscience*. (World Scientific, 2010).

145. Cai, Y., Naser, N. Y., Ma, J. & Baneyx, F. Precision Loading and Delivery of Molecular Cargo by Size-Controlled Coacervation of Gold Nanoparticles Functionalized with Elastin-like Peptides. *Biomacromolecules* **25**, 2390–2398 (2024).

146. Shusharina, N. P., Nyrkova, I. A. & Khokhlov, A. R. Diblock Copolymers with a Charged Block in a Selective Solvent: Micellar Structure. *Macromolecules* **29**, 3167–3174 (1996).

147. Marko, J. F. & Rabin, Y. Microphase separation of charged diblock copolymers: melts and solutions. *Macromolecules* **25**, 1503–1509 (1992).

148. Xi, S., Wang, L., Liu, J. & Chapman, W. Thermodynamics, Microstructures, and Solubilization of Block Copolymer Micelles by Density Functional Theory. *Langmuir* **35**, 5081–5092 (2019).

149. Hervé, P. *et al.* Novel core-shell structure for colloids made of neutral/polyelectrolyte diblock copolymers and oppositely charged surfactants. *Europhysics Letters (EPL)* **58**, 912–918 (2002).

150. Lu, Y., Lin, J., Wang, L., Zhang, L. & Cai, C. Self-Assembly of Copolymer Micelles: Higher-Level Assembly for Constructing Hierarchical Structure. *Chemical Reviews* **120**, 4111–4140 (2020).

151. Jain, S. & Bates, F. S. On the Origins of Morphological Complexity in Block Copolymer Surfactants. *Science (1979)* **300**, 460–464 (2003).

152. Van Eldijk, M. B. *et al.* Synthesis and self-assembly of well-defined elastin-like polypeptide-poly(ethylene glycol) conjugates. *Biomacromolecules* **15**, 2751–2759 (2014).

153. Weitzhandler, I. *et al.* Micellar Self-Assembly of Recombinant Resilin-/Elastin-Like Block Copolypeptides. *Biomacromolecules* **18**, 2419–2426 (2017).

154. Coradin, T. & Livage, J. Effect of some amino acids and peptides on silicic acid polymerization. *Colloids Surf B Biointerfaces* **21**, 329–336 (2001).

155. Coradin, T. & Lopez, P. J. Biogenic silica patterning: Simple chemistry or subtle biology? *ChemBioChem* **4**, 251–259 (2003).

156. Roeters, S. J. *et al.* Backbone Structure of Diatom Silaffin Peptide R5 in Biosilica Determined by Combining Solid-State NMR with Theoretical Sum-Frequency Generation Spectra. *Journal of Physical Chemistry Letters* **12**, 9657–9661 (2021).

157. Pagliaro, M. & Hutchings, G. J. Heterogeneous catalysis for fine chemicals. *Catal Sci Technol* **1**, 1543 (2011).

158. Shi, J. On the Synergetic Catalytic Effect in Heterogeneous Nanocomposite Catalysts. *Chem Rev* **113**, 2139–2181 (2013).

159. Lee, C. H., Lo, L. W., Mou, C. Y. & Yang, C. S. Synthesis and characterization of positive-charge functionalized mesoporous silica nanoparticles for oral drug delivery of an anti-inflammatory drug. *Adv Funct Mater* **18**, 3283–3292 (2008).

160. Kim, M. H. *et al.* Facile synthesis of monodispersed mesoporous silica nanoparticles with ultralarge pores and their application in gene delivery. *ACS Nano* **5**, 3568–3576 (2011).

161. Vallet-Regí, M., Ruiz-González, L., Izquierdo-Barba, I. & González-Calbet, J. M. Revisiting silica based ordered mesoporous materials: medical applications. *J Mater Chem* **16**, 26–31 (2006).

162. Lee, J., Hong, C. K., Choe, S. & Shim, S. E. Synthesis of polystyrene/silica composite particles by soap-free emulsion polymerization using positively charged colloidal silica. *J Colloid Interface Sci* **310**, 112–120 (2007).

163. Clavero, C. Plasmon-induced hot-electron generation at nanoparticle/metal-oxide interfaces for photovoltaic and photocatalytic devices. *Nat Photonics* **8**, 95–103 (2014).

164. Veisi, H., Abassi, P., Mohammadi, P., Tamoradi, T. & Karmakar, B. Gold nanoparticles decorated biguanidine modified mesoporous silica KIT-5 as recoverable heterogeneous catalyst for the reductive degradation of environmental contaminants. *Sci Rep* **11**, (2021).

165. Ramanathan, R., Campbell, J. L., Soni, S. K., Bhargava, S. K. & Bansal, V. Cationic Amino Acids Specific Biomimetic Silicification in Ionic Liquid: A Quest to Understand the Formation of 3-D Structures in Diatoms. *PLoS One* **6**, e17707-(2011).

166. Belton, D., Paine, G., Patwardhan, S. V. & Perry, C. C. Towards an understanding of (bio)silicification: The role of amino acids and lysine oligomers in silicification. *J Mater Chem* **14**, 2231–2241 (2004).

167. Naser, N. Y. *et al.* Biomimetic mineralization of positively charged silica nanoparticles templated by thermoresponsive protein micelles: applications to electrostatic assembly of hierarchical and composite superstructures. *Soft Matter* (2024) doi:10.1039/D4SM00907J.

168. Baffou, G., Quidant, R. & Girard, C. Heat generation in plasmonic nanostructures: Influence of morphology. *Appl Phys Lett* **94**, 153109 (2009).

169. Baffou, G., Quidant, R. & García De Abajo, F. J. Nanoscale control of optical heating in complex plasmonic systems. in *ACS Nano* vol. 4 709–716 (2010).

170. Sun, J. & Zuckermann, R. N. Peptoid polymers: A highly designable bioinspired material. *ACS Nano* **7**, 4715–4732 (2013).

171. Li, Z., Cai, B., Yang, W. & Chen, C. L. Hierarchical Nanomaterials Assembled from Peptoids and Other Sequence-Defined Synthetic Polymers. *Chemical Reviews* **121**, 14031–14087 (2021).

172. Jun, J. M. V., Altoe, M. V. P., Aloni, S. & Zuckermann, R. N. Peptoid nanosheets as soluble, two-dimensional templates for calcium carbonate mineralization. *Chemical Communications* **51**, 10218–10221 (2015).

173. Yang, W., Yin, Q. & Chen, C. L. Designing Sequence-Defined Peptoids for Biomimetic Control over Inorganic Crystallization. *Chemistry of Materials* **33**, 3047–3065 (2021).

174. Yang, W. *et al.* Designing sequence-defined peptoids for fibrillar self-assembly and silicification. *J Colloid Interface Sci* **634**, 450–459 (2023).

175. Henzler, K. *et al. Supersaturated Calcium Carbonate Solutions Are Classical*. https://www.science.org (2018).

176. Stephanopoulos, N. Hybrid Nanostructures from the Self-Assembly of Proteins and DNA. *Chem* **6**, 364–405 (2020).

177. Kim, N. H. *et al.* Supramolecular assembly of protein building blocks: from folding to function. *Nano Convergence* **9**, 4 (2022).

178. Suzuki, Y. *et al.* Self-assembly of coherently dynamic, auxetic, two-dimensional protein crystals. *Nature* **533**, 369–373 (2016).

179. Rothemund, P. W. K. Folding DNA to create nanoscale shapes and patterns. *Nature* vol. **440**, 297–302 (2006).

180. Seeman, N. C. Nanomaterials based on DNA. *Annual Review of Biochemistry* **79**, 65–87 (2010).

181. Li, Q., Wang, Y., Zhang, G., Su, R. & Qi, W. Biomimetic mineralization based on self-assembling peptides. *Chemical Society Reviews* **52**, 1549–1590 (2023).

182. Wang, S. *et al.* Mechanistic process understanding of the self-assembling behaviour of asymmetric bolaamphiphilic short-peptides and their templating for silica and titania nanomaterials. *Nanoscale* **13**, 13318–13327 (2021).

183. Abdali, Z. *et al.* Curli-Mediated Self-Assembly of a Fibrous Protein Scaffold for Hydroxyapatite Mineralization. *ACS Synth Biol* **9**, 3334–3343 (2020).

184. Cui, F. Z., Li, Y. & Ge, J. Self-assembly of mineralized collagen composites. *Materials Science and Engineering R: Reports* **57**, 1–27 (2007).

185. Moradian-Oldak, J. Protein-mediated enamel mineralization. *Frontiers in Bioscience* **17**, 1996–2023 (2012).

186. Le Norcy, E. *et al.* Phosphorylated and non-phosphorylated Leucine Rich Amelogenin Peptide differentially affect ameloblast mineralization. *Front Physiol* **9**, (2018).

187. Huang, P. S., Boyken, S. E. & Baker, D. The coming of age of de novo protein design. *Nature* **537**, 320–327 (2016).

188. Gonen, S., DiMaio, F., Gonen, T. & Baker, D. Design of ordered two-dimensional arrays mediated by noncovalent protein-protein interfaces. *Science (1979)* **348**, 1365–1368 (2015).

189. Chen, Z. *et al.* Self-Assembling 2D Arrays with de Novo Protein Building Blocks. *J Am Chem Soc* **141**, 8891–8895 (2019).

190. Shen, H. *et al. De Novo Design of Self-Assembling Helical Protein Filaments*. https://www.science.org (2018).

191. Akkineni, S. *et al.* Amyloid-like amelogenin nanoribbons template mineralization via a low-energy interface of ion binding sites. *Proceedings of the National Academy of Sciences* **119**, e2106965119 (2022).

192. Tao, J. *et al.* Control of Calcium Phosphate Nucleation and Transformation through Interactions of Enamelin and Amelogenin Exhibits the ‘goldilocks Effect’. *Cryst Growth Des* **18**, 7391–7400 (2018).

193. Akkineni, S. *et al.* Biomimetic Mineral Synthesis by Nanopatterned Supramolecular-Block Copolymer Templates. *Nano Lett* **23**, 4290–4297 (2023).